UNICA

UNIVERSITÀ
DEGLI STUDI
DI CAGLIARI

Ph.D. DEGREE IN
Physics

Cycle XXXVIII

TITLE OF THE Ph.D. THESIS

Heat Transport in Thermoelectric Materials:

from Layered Systems to Organic Crystals

Scientific Disciplinary Sector(s)

FIS/03

Ph.D. Student:	Siddi Francesco
Supervisor	Melis Claudio
Co-Supervisor	Colombo Luciano

Final exam. Academic Year 2024/2025
Thesis defence session: February 2026

Contents

Abstract

Thermoelectricity (TE) is a promising and sustainable source of energy that manage to convert wasted heat into electricity using the Seebeck effect. A good material for TE application should have with low thermal conductivity (k) and high Seebeck coefficient and electrical conductivity, because TE generators efficiency is inversely proportional to the first property and directly proportional to the other two properties. Unfortunately, materials with such characteristics are not present in nature, so as of now TE is not yet a viable form of energy due to its low efficiency. In order to increase it, we can modify some pristine materials to decrease its k and increase its electrical properties. In this thesis is presented a computational study of the thermal transport property of three materials, two belonging to the class of TMD (TaS2 and MoS2) and organic molecular crystals (BTBT, DNTT), using both ab-initio techniques and MD simulations. TMDs have high electrical properties, making them ideal for TE applications, but showed large k that decreases their possible use as TEG. Thus, after a detailed study of their thermal properties, it is shown that their inplane k greatly varies from their 2D and bulk phases, due to some inter-layer vibrational modes that are suppressed by the distancing of the layers. Furthermore, it is shown how the correct functionalization further decreases the k, making the functionalized and distanced system a good material for thermoelectric applications. While another decrease in k is found in a system with vacancies, it is observed that under the correct conditions the system showed

a super periodicity that restores the original k value. BTBT and DNTT have low k, but it is shown deviations from the expected k(T) trend because of its high anharmonic properties. While a BTE-level theory fails to predict it, both Wigner theory and MD simulations reproduces this deviation correctly, giving credit to AEMD simulations in highly anharmonic crystals

Chapter 1

Introduction

In the present landscape, energy sustainability and the reduction of energy waste are among the main concerns of current scientific research. Although powerful and sustainable energy sources have already been adopted in many circumstances with good conversion efficiency, they have many shortcomings that require further studies to overcome.

One of those is the waste of energy in the form of heat, that is a major concern on both new and old sources of energy. Thermoelectricity is a sustainable way to convert this wasted heat back into electricity, making thermoelectric generators prime candidates for auxiliary generators on the side of larger power sources [1].

Thermoelectric generators have really interesting characteristics. They offer extremely good scalability, noise-free energy generation, absence of moving and mechanical parts and great reliability, making thermoelectric energy suitable for a great variety of applications other than the aforementioned wasted energy recovery, e.g. energy generation in deep space missions and batteries for cardiac pacemakers.

Despite its really good advantages, thermoelectricity is still in dire need of further

scientific studies in order to become a major candidate for solving the aforementioned problems because of its terrible conversion efficiency.
The scope of this thesis is to offer an insight on the current thermoelectric landscape and to propose ways to improve the efficiency of such generators.

1.1 A brief history of thermoelectricity

Thermoelectricity first observations can be traced back to XVIII century, thanks to an experiment performed by the physicist and chemist Alessandro Giuseppe Antonio Anastasio Volta [2]. While studying the response of muscles when exposed to external electricity, Volta observed that if a dead frog's legs were put in a glass of water and is upper body was put in a different one the frog's muscles had some violent contractions [3]. He proposed a theory that related such contraction on the difference in temperature between the two glasses, and since previous experiment proved a correlation between muscles contraction and electricity, he was able to relate for the first time a difference in temperature with an electric current [4].
No further discoveries were made in this field for another twenty years, until the German physicist Johann Seebeck proposed a new explanation of the phenomenon with the theory of thermomagnetism. While the thermomagnetism theory was proved false by later studies[5], Seebeck's interpretation gives us the first parametrization of the relation between heat and electric current and the Seebeck's coefficient that he proposed is still today used in thermoelectric materials description. Because of this, today the phenomenon of electromotive force induced by a heat gradient take the name of Seebeck's effect and it is controlled by the Seebeck's coefficient:

$$S = -\frac{dV}{dT} \tag{1.1}$$

where V is the potential difference e T is the temperature [6].

Seebeck's studies, in conjunction with the progress on electromagnetism [7–9], opened a new field of research that aimed to find a relation between heat and electrical currents.

Of particular interest is the studies performed by Peltier in 1834. The French watchmaker discovered by generating a electrical current in a conductor composed by two different metal he was able to heat up or to cool down the system depending on the direction of the current. He explained the phenomenon by means of the Joule effect, but we know now that the two phenomena are in fact distinct and we call the one discovered by Peltier the *Peltier effect*. Today, we know that when a current is forced to pass between two different conductors, heat is released or absorbed by the junction between them [10]. The *Peltier coefficient* is often used to quantify this phenomenon:

$$\pi = \frac{\dot{Q}}{i} \tag{1.2}$$

where $\dot{Q}$ is the heat absorbed or released per unit time in the junction and i is the electric current flowing in the system.

In 1854, the British physicist Thomson finally gave an explanation of both Seebeck and Peltier effects in thermodynamic therms. While working on the first two thermodynamic laws, he discovered a new thermoelectric effects and was able to correlate the other two [11]:

$$\tau = \frac{\dot{q}}{\mathbf{j} \cdot \nabla T} \tag{1.3a}$$

$$\pi = S \cdot T \tag{1.3b}$$

$$\tau = T \cdot \frac{dS}{dT} \tag{1.3c}$$

Equation 1.3a is known as *Thomson effect* and is able to correlate the heat absorbed or released per unit of time and volume ($\dot{q}$) with the current density (j).

These three equations summarize the three fundamental thermoelectric effects and

with them came the idea of using a thermal gradient to induce an electrical current.

For the first time, in 1885 Rayleigh proposed the Seebeck effect as an active method to create electrical power [12]. While still far from the thermoelectric generation that we know today, this is the beginning of the research in this field, and in the following years many studies were made in this regard. As result of these researches, the firsts thermoelectric generators (TEG) were made [13].

While TEG using the Seebeck attracted a lot of attention and obtained mixed results, we have to wait until the discovery of semiconductors for the firsts devices that actively use the Peltier effect, i.e. use electric current to cool the environment, because of the extremely low conversion efficiency. Those devices are called *Peltier cells*.

In 1909, the German physicist Altenkirch discovered the theoretical maximum efficiency of a thermoelectric device. He proposed a model that is very similar to the modern understanding of the phenomenon, correctly suggesting that the thermoelectric efficiency is proportional to the one of the Carnot cycle (that is it's upper limit), and that the efficiency depends on the material thermoelectric properties: the Seebeck coefficient and the electrical and thermal conductivities [14].

After this, research in the thermoelectric scene stopped making progress, and we have to wait until the 1950s to obtain new developments. Thanks to the development on quantum mechanics and statistical dynamics, the American physicist and chemist Onsager obtained a generalized version of Equation 1.3c, and using those the Russian physicist Ioffe proposed the *dimensionless thermocouple figure of merit*:

$$Z\bar{T} = \frac{S_{pn}^2}{KR}\bar{T} \tag{1.4}$$

where S_{pn}^2 is the thermopower of the system, i.e. the squared difference between the Seebeck coefficient of the of the p and n components of the thermocouple, K

is the thermal parallel conductance, R is the series electrical resistance and $\bar{T}$ is the average temperature at which the system operates [15].

Ioffe stated that by maximizing $Z\bar{T}$ one can maximize the efficiency of the thermocouple. Having that in mind, we can write the efficiency of a TEG as:

$$\eta = \frac{\Delta T}{T_h} \times \frac{\sqrt{1 + Z\bar{T}} - 1}{\sqrt{1 + Z\bar{T}} + \frac{T_c}{T_h}} \tag{1.5}$$

where T_h and T_c are the temperatures of the hot and cold part of the system and ΔT is their difference [15].

Both Equation 1.4 and Equation 1.5 can be generalized to describe the property that in the years to come will be referred as the *fundamental parameter* for a thermoelectric material, the *material dimensionless figure of merit*:

$$zT = \frac{\sigma S^2}{\kappa} \tag{1.6}$$

This formulation of the figure of merit depends only on the properties of a single material that compose the TEG, therefore we can use this zT to compare the thermoelectric performances of different materials in a easy and ordered way. More specifically, zT depends linearly on the electrical conductivity σ, quadratically on the Seebeck's coefficient of the material S and inversely on the thermal conductivity κ. The grater the zT value is, the more useful a material is for thermoelectric applications. Alternately, we can say that a "good" thermoelectric material has high electrical conductivity, high Seebeck coefficient and low thermal conductivity. Moreover, this Equation can be further generalized by considering the dependence on the temperature of its parameters, in fact σ, S and κ change with temperature, so we can have a good thermoelectric material that operates at low temperatures that does not work as well at high temperatures and the reverse can also be true. The problem that emerges in this formulation is that there are no materials in nature that meet all the requirements cited above properly.

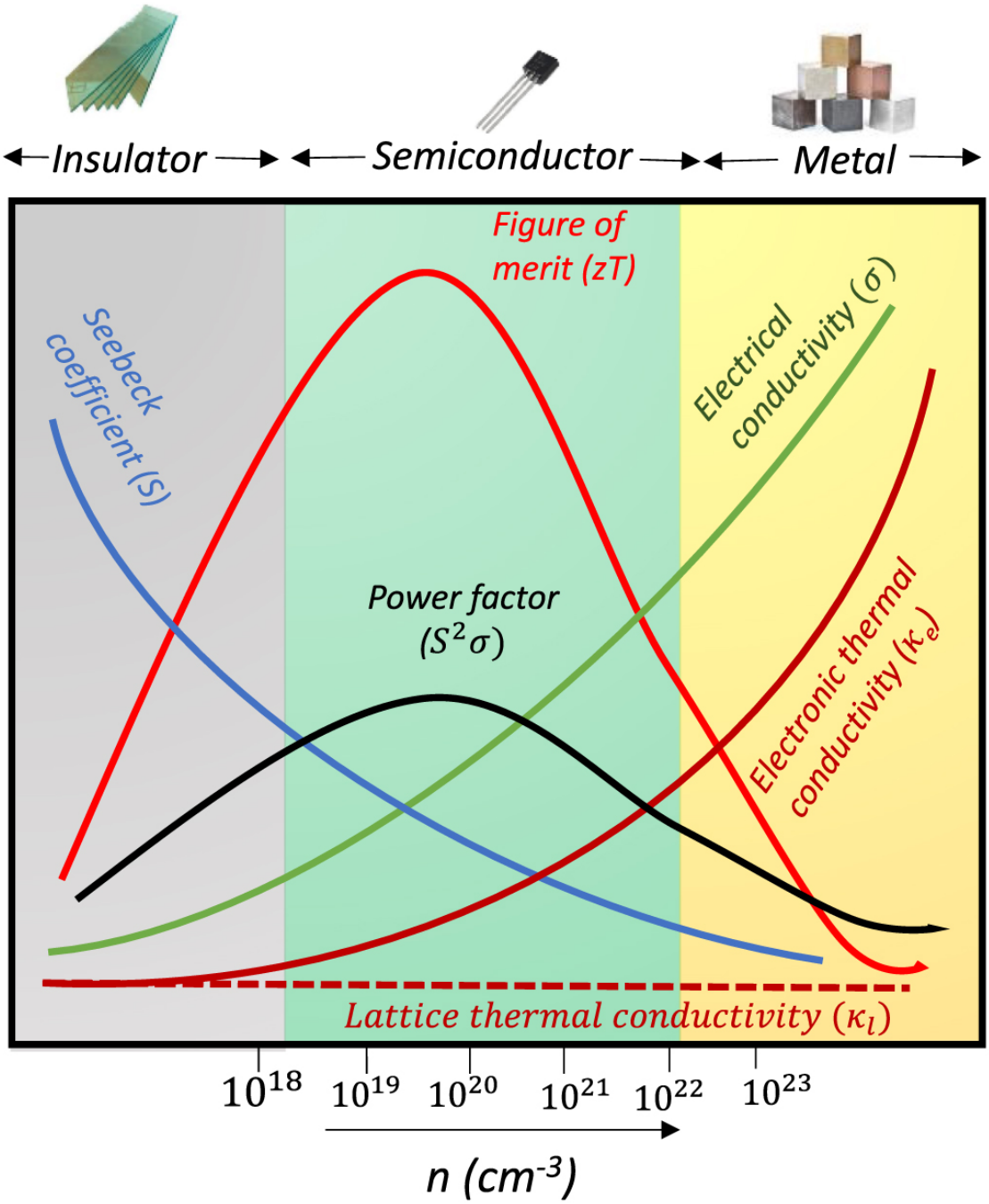

Figure 1.1: *Value of the figure of merit zT, Seebeck coefficient, electrical and thermal conductivity in function of the free carrier concentration [16].*

As we can see in Figure 1.1, all three properties depends on the free carrier concentration of the material and while the electrical and total thermal conductivities both increase with the number of free carrier, the Seebeck's coefficient decreases. This means that in nature there is a fixed limit at which the zT are limited because of the carrier concentration and this value is extremely low.

This is the main reason why since the earlier years of the studies on thermoelectricity, Ioffe himself did not proposed his findings using pure materials but he employed heavily doped semiconductors, in particular the telluride, of bismuth, of antimony and of lead.

Even if the greater efficiency obtained was of a meager 5% [17], some early applications for TEG generators were used in various fields, e.g. some early cooling device in the United Kingdom or some devices in the rural part of Russia that were able to generate electricity even where the main electrical grid didn't extend [18, 19].

Unfortunately, due to its very low efficiency (below 5%), thermoelectricity became a niche field of research and was deemed not capable of extensive power generations. However, TEG offered some really interesting advantages that allow to keep some degree of interest in this area of research. In particular, the fact that they are solid state generators allow the construction on very reliable devices, with no moving parts and durable for a long time without the need of maintenance.

Two noticeable application are on deep space mission as main generators for the electronics of satellites or probes and the use of nuclear thermoelectric batteries as pacemaker with a long lifetime (recently replace because of concern about nuclear waste) [20].

Other than this very niche applications, no further development of thermoelectricity was made until the end of the 1990s, were, thanks to the development of nanotechnology brought in the horizon a new prospective for the thermoelectric

scene [21]. In fact, nanostructured materials can show different behaviors for different carriers and opened the possibility for materials in which phonons behave like they were in a glass and the electron have a mobility similar to the one in a crystalline semiconductor (Slack's *phonon-glass electron-crystal* concept [22]).
This behavior leaded to another surge of interest in thermoelectricity as a widely used source of energy and so its field of research attracted once again a lot of attention.
Even with this newer development, the average zTs values do not exceed $zT \sim 1$ and, as we can see in Figure 1.2, this value is pretty low compared to zTs of other types of generators [23, 24].

But the new millennium brought new problems [25], in particular regarding en-

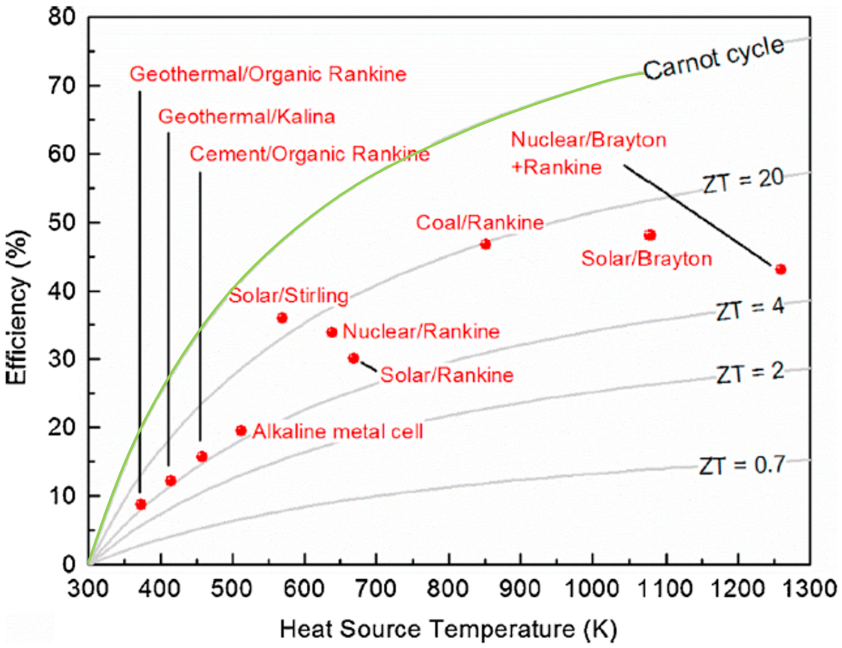

Figure 1.2: *Figure of merit for various energy generator types compared with the Carnot cycle (green line) [1].*

ergy issues, and thermoelectricity found a new way to shine in the field of auxiliary

generators. Many modern generators lose some energy in form of heat and the current idea in the thermoelectric scenario is to use that heat to fuel a TEG, in order to maximize energy production. Some examples are the wasted heat from vehicle engines, from factories or other type of power plants.

Another problem that thermoelectricity is suitable to address is the generation of energy in modern electronic devices. Since TEG are scalable they could be used in some micro-devices that still need electrical energy to function, giving rise to the field of research about *micro*-thermoelectric generators (μTEG). Those systems are currently developed and used both as primary generators as auxiliary ones that help some micro-photovoltaic cells to supply energy [26, 27].

Considering all this, today the research on thermoelectric materials is more active

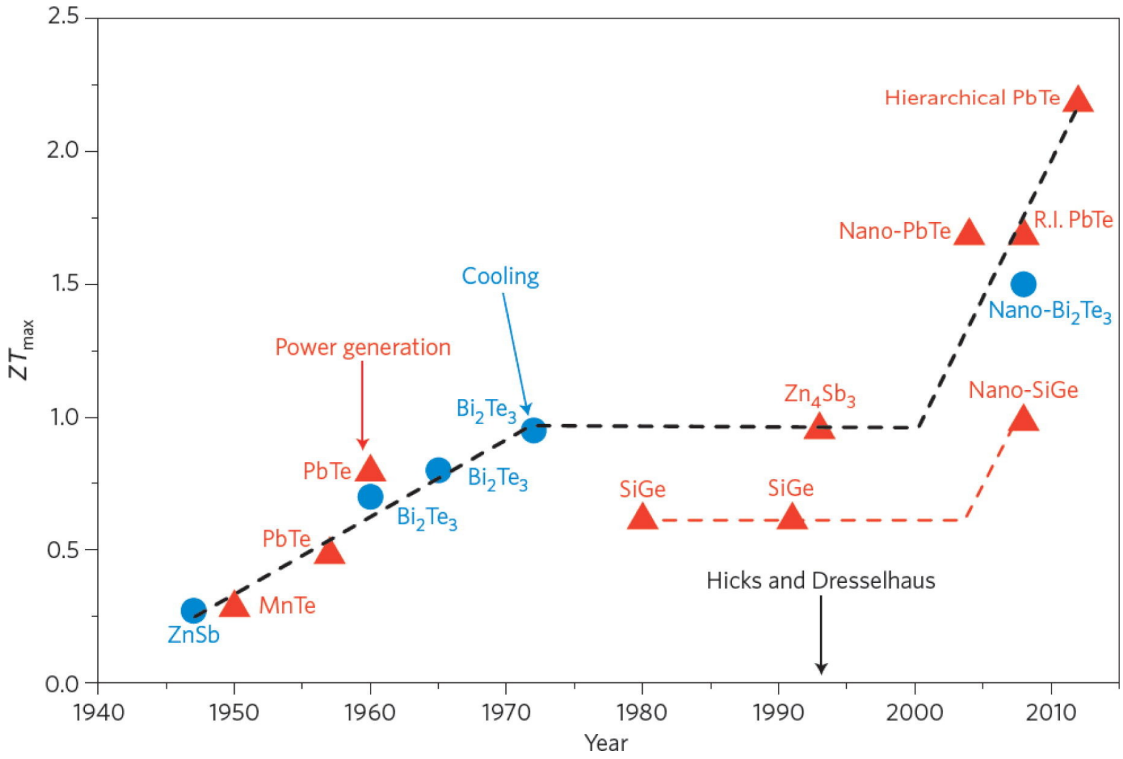

Figure 1.3: *Figure of merit for various compounds in function of the year of their synthesis [28].*

than ever, focusing on identifying some novel nano-materials with high zTs that

can lead to a sufficiently efficient TEG. As we can see in Figure 1.3, since 2000 till today researchers have made great progress in increasing the zT of materials, and recently they have found systems that can lead to a $zT > 2$, more than doubling the results obtained with the earlier studies. There are currently two main strategies that scientist use to increase the zT: a decrease in the lattice thermal conductivity and a increase in the carrier mobility [28].

My work is focused on the first approach and aims to provide some insight in the process of the conduction of heat that take place in two particularly interesting classes of materials, i.e. the two dimensional Transition Metal Dichalcogenides (2D TMD) and some unique molecular crystals formed by organic molecules .

1.2 Transition Metal Dichalcogenides

Two-dimensional transition-metal dichalcogenides (TMDs) are a class of materials that has attracted great interest in a wide variety of different field thanks to their great properties [29]. Some examples of applications are nanoelectronics, nanophotonics, sensing and thermoelectricity [1, 30] TMDs have been extensively studied in the past, but only recently, with the discovery of strong photoluminescence in MoS_2 mono-layers [31, 32] and the synthesis of the first transistor made with TMDs [33], they become one of the main focuses of modern material science research.

1.2.1 History of TMDs

Transition-metal dichalcogenides have a long and rich history. In 1923, Linus Pauling determined their crystal structure for the first time [34] and by the late 1960s, roughly 60 TMD compounds were known, about 40 of which exhibit layered structures [35]. In 1963, Robert Frindt reported using adhesive tape to isolate ultra-thin MoS_2 layers [36], and mono-layer MoS_2 suspensions were subsequently obtained in 1986 [37].

During the 1990s, alongside the surge of research on carbon nanotubes and fullerenes, Reshef Tenne and collaborators pioneered studies of inorganic fullerenes and nanotubes, beginning with the discovery of WS_2 nanotubes and nested particles [38] and later synthesizing MoS_2 nanotubes and nanoparticles [39].

The rapid growth of graphene research after 2004 further advanced techniques for working with layered materials [40], opening the door to renewed investigations of TMDs and their atomically thin films [41].

In the present, TMDs are used in a large array of applications, e.g. semiconductor systems, lightweight wearables, and flexible technologies, because of their mechanical flexibility, optical sensitivity and versatile electronic properties [42]. For example, the TMD MoS_2 is well known among the transistors area of research. In fact, field-effect transistors and light-emitting transistors are widely utilized [33], thanks to MoS_2 incredible carrier mobility of 200 $cm^2V^{-1}s^{-1}$ [43]. The same type of devices are made using WS_2, obtaining similar results [44].

1.2.2 Structure of TMDs

The Transition-metal dichalcogenides material class is defined by the chemical formula TX_2, were T is a transition metal and X a chalcogen atom. Transition metals are typically atoms that belongs in group IV and V in the periodic table. Some examples of transition metals are Molybdenum (M), Tungsten (W), Tantalium (Ta), while some examples of chalcogen atoms are Sulfur (S), Selenium (Se) and Tellurium (Te).

TMDs have a layered structure with a rather peculiar structural arrangement. In fact the single layer can be seen as a material with the structure X-M-X, where a single plane composed by the Transition Metal separates two hexagonal planes of chalcogen atoms. Typical examples of TMDs are molybdenum and tungsten diselenide (respectively MSe_2 and WSe_2) in addition to the aforementioned molybdenum disulfide (MoS_2) and the tungsten disulfide (WS_2). Of course, every combination of a transition metal and a chalcogen atom are theoretically possible and as of today more than forty different blends of TMDs are experimentally synthesized [45].

As can be seen in Figure 1.4, he single TMD layer can be found in different coordinations of the transition metal atoms, or structural phases. Typically those

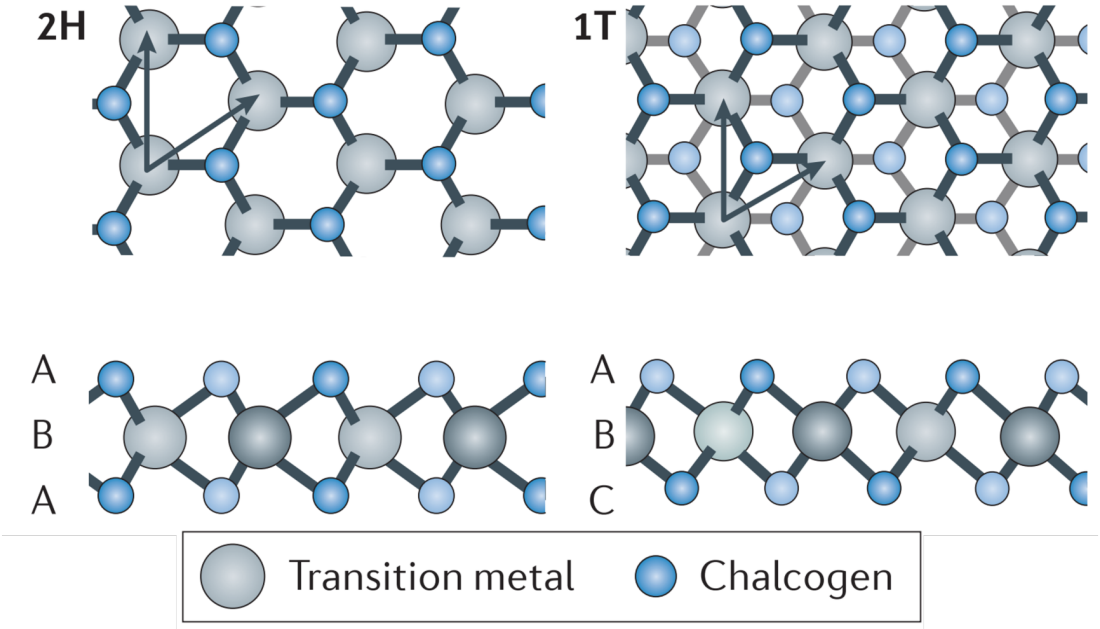

Figure 1.4: *Typical structure of a generic single layer of TMD, showing the two typical structural phases 2H and 1T. The lattice vectors, along with the stacking sequence of the atomic planes, are shown [29].*

coordinations are trigonal prismatic (2H) and octahedral (either 1T or its distortion 1T') and they exhibit widely different properties even in structures with the same atomic components. The 2H coordination can be described as a TMD layer which has his three atomic planes (chalcogen-metal-chalcogen) organized with an ABA stacking, i.e. the chalcogen atoms in the lower plane share the same lattice position as the chalcogen atoms in the upper plane (A) whereas the transition metal plane is located in a different lattice position (B). On the other hand, the 1T and the 1T' coordinations are characterized by a disposition of its three atomic layers of ABC, where none of the three atomic layers share the same lattice position. Typically, 1T' structures are more stable than the respective 1T one (e.g. in MoS_2 the energy of the 1T structure is found to be 0.29 eV/basic unit cell higher than the one of the 1T' structure [46]), but in some other TMDs, e.g. TaS_2, there is no evidence of the presence of a distorted 1T' phase [48].

The stable structural coordination that a TMD take is determined by the chalcogen atom and the transition metal that composes the material. Typically, a TMD has one thermodynamically stable phase (either 2H or 1T') and can be synthesized in the second phase as a metastable structure. For example, all the TMD composed by Molybdenum and a chalcogen atom (i.e. MoS_2, $MoSe_2$ and $MoTe_2$) are stable in the 2H phase, while for the compound with tungsten WS_2 and WSe_2 are stable in the 2H phase and the WTe_2 structure has a stable 1T' phase [47].
When looking at a bulk state TMD, i.e. a TMD composed of multiple atomic layers, another defining structural property is the stacking configuration of the layers.

A good example of different stacking is showed in Figure 1.5. There we can find a visual representation of four different structures of the TMD TaS_2, where the gray spheres represent the Tantalum atoms and the yellow ones are the Sulfur atoms. TaS_2 has three possible phases, 1T, that is unstable at room temperature but becomes stable at $T > 1300$ K, 2H and the peculiar phase 3R [48]. Moreover, we can notice a great difference between the AB and AA' stacking of the 2H phase. The most stable phase is the 2H with AA' stacking, with the 2H-AB and 3R at around the same ground energy and lastly is the 1T phase [48].
Typically, the different layers of a bulk TMD crystal are bonded only by weak van der Walls forces, giving TMDs the structured of a layered material, but distortions in either the single layer or the stacking pattern may give rise to systems with lower periodicity that can generate some metal-metal bonds, on top of some really interesting differences in both electronic and phononic structures. A visualization of the TMDs' layered structure is provided in Figure 1.6.

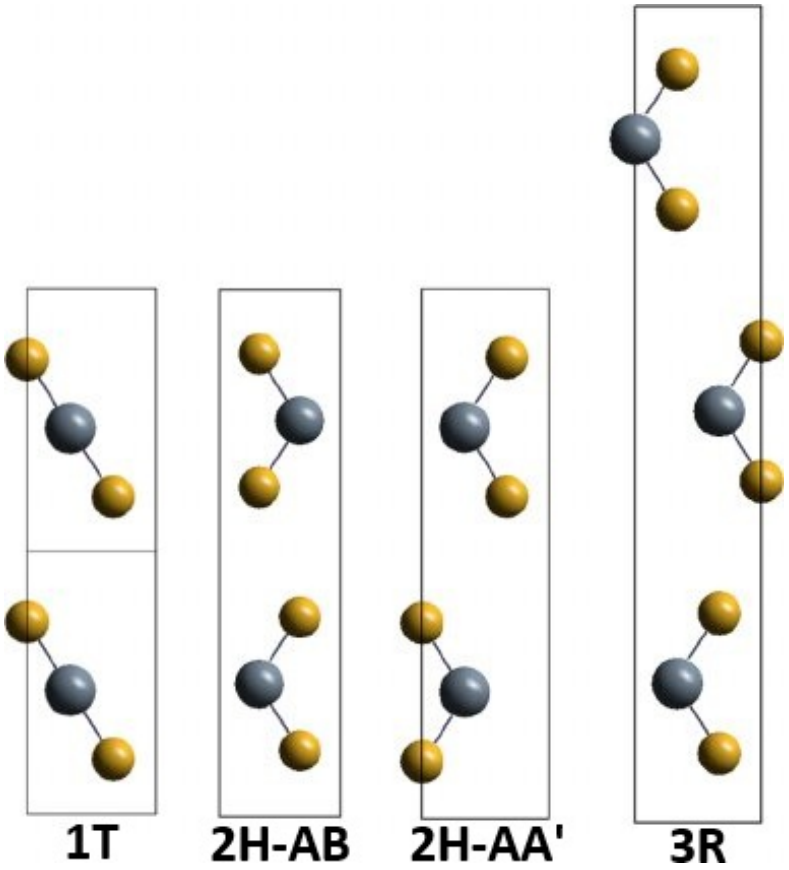

Figure 1.5: *Different structures of multi-layered TaS_2. From the left, we find its metastable 1T phase, its stable 2H phase with two different stacking types (AB and AA') and its more rare 3R phase. The gray spheres are the Tantalum atoms and the yellow ones are the Sulfur atoms [48].*

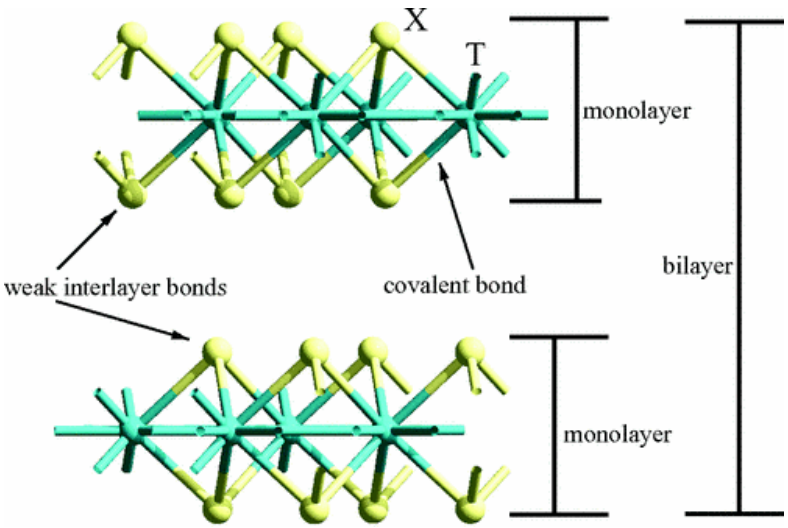

Figure 1.6: *Schematic representation of the layered structure for a TMD [49].*

1.2.3 Synthesis

In nature, from the currently over 60 known TMDs, only two can be found, specifically the layered crystals of MoS_2 and WS_2. In fact, the aforementioned first monolayer MoS_2 transistor was obtained using crystal of molybdenite found in nature [33].

In the present, a wide array of synthesis method are used in order to create and study a wide array of TMDs. The first and most used method still today is the chemical vapor transport (CVT) method, which allow to study bulk crystal of some interesting TMDs, like MoS_2, $MoSe_2$ and WSe_2. This method involves the mixing of the metal and chalcogens reactants (in the case of MoS_2 Mo and S) in a ampoule containing a transport agent (e.g. I2 and Br2). This ampoule is then put in a multi-zone furnace, heated with a suitable temperature gradient, and TMDs crystals form in the colder regions of the ampoule [50].

From the crystals forged in such way, it is needed to employ some other method in order to obtain a single layer TMD, obtaining the 2D material needed for various applications, such as TMD nanotubes and nanosheets. In Figure 1.7 are shown the principal methods used for such purpose.

Historically, the first method that has been employed is the mechanical exfoliation or cleavage. This technique was proposed by Frindit in 1966 and produced the first MoS_2 flakes [51]. This method principal advantages is its ease of application, in fact it requires only the bulk TMD crystal, an adhesive tape and a selected substrate like SiO_2 or Si [52, 53]. This process involves the use of adhesive tape to break the weak van der Walls forces that binds the bulk TMD crystal together and deposit a single MX_2 flake into the substrate. Repetition of this process on the flakes thus obtained is able to reduce the number of layer in each one ad so after some iterations it is possible to obtain single-layered TMDs. While this method is popular due to its ease of application and the quality of the systems produced, it

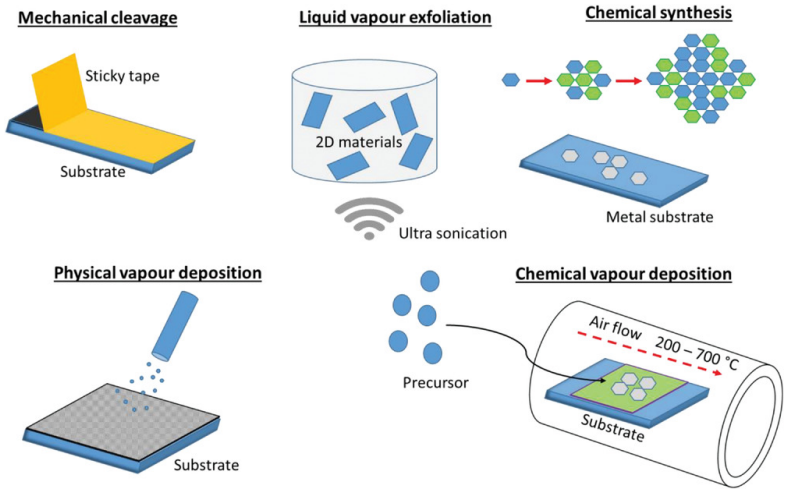

Figure 1.7: *Synthesis methods of 2D TMD from their relative bulk crystal [40].*

has many flaws in its lack of scalability, i.e. the size and shape of the flakes that it produces, and in the small quantity of uniform material obtainable [54]. Recently, a modification of this method was proposed by Gracem that aims to prevents the shortcomings of mechanical exfoliation while retaining its main advantages [55]. This method, called anodic bonding, is able to obtain single-layer materials with quality similar to the bulk that it originates from, without any chemical remains. Overall, mechanical exfoliation is a good method to obtain rapidly some 2D TMDs for preliminary studies, but it is not suitable for extensive research due to its low yield of final product.

A solution of this problem is presented in the form of chemical exfoliation technique, also called the liquid vapour method. The principles of this technique consist in placing an intercalator between the MX_2 layers using ultrasonication in water [56, 57]. Typical intercalators are organiometallic compounds like butyl lithium, naphthyl and sodium. A variation of this method was developed by Zhang which consist in placing the bulk TMD in a electrochemical setup before the insertion of the intercalator [58]. While this method solves the problems with the mechanical cleavage, and the use of organic systems as intercalators make TMDs obtained in

this way viable for biomedical applications, the process of sonification give rise to defect in the product structure making this method not suitable for large scale applications.

A more advanced chemical method is the liquid-phase exfoliation. Discovered by Li and refined during the 1970s [59] and 1980s [37], this method allows the production of TMD flakes in solution with organic solvents. This method improves in scalability if confronted with the mechanical cleavage one, but, as demonstrated by subsequent research for MoS_2 2D systems [60], it forces the TMD from its 2H stable phase to a metastable, metallic 1T phase. Furthermore, the flakes obtained in this way tend to overlap in a large enough system, leading to a large in-plane resistance of the films [56].

Another highly effective method is the Chemical Vapour Deposition (CVD). This method consist in exposing the precursors to a substrate in an environment with high temperature and pressure. The precursors chalcogen and TM atoms react and then they deposit in the substrate. This allows the formation of atomically thin MX_2 layers [61]. This technique was applied in the creation of many 2D pristine TMD, like MoS_2 [62], $MoSe_2$ [63] and $MoTe_2$ [64] to name a few, but it can also be applied to create some modified TMD mono-layers, such as doped layers [65, 66] or heterostructures [67, 68]. This is a great way to tune the properties of TMDs in order to fit the application needs. The CVD method is highly effective and it allows to obtain 2D TMDs with a precise structure and with a controlled purity, but it is limited by its excessive cost and by the difficulty of application.

The most promising synthesis method is the molecular beam epitaxy (MBE). In Figure 1.8 is shown a schematic representation of this method. The experimental setup includes an ultrahigh vacuum chamber (pressure below 10^{-10} mbar) and a substrate heated at a certain temperature. Then the molecular beams (in the case of Figure 1.8 containing Ga and Se) are shoot in the substrate and monitored with

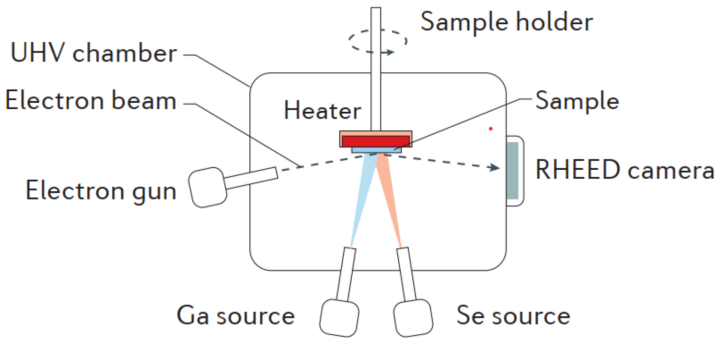

Figure 1.8: *Schematic representation of a molecular beam epitaxy [29].*

a RHEED camera [50].

Today, MBE is widely use to synthesize 2D TMDs not only in their pristine state [69], but also in some form of heterostructures [70]. Because of the reliability of this method in controlling the composition, thickness and structural phase of the resulting material, MBE is as today the most promising technique used to synthesize large-scale 2D TMD samples with high purity, even if it may produce some small grain sizes.

1.2.4 Electronic properties

The electronic properties of TMDs are the most interesting features of this class of materials even in their pristine state. As we can see in Figure 1.9, TMDs have a wide variety of bandgaps, raging from visible to infrared range [71]. Nonetheless, the most interesting property of TMDs is their capacity to mutate their bandgap when reducing their dimensionality. In fact, the bulk state typically shows an indirect bandgap, while few layered or mono-layered systems show a direct bandgap. This promising property is most likely due to the variation of the hybridization of orbitals in both transition metal and chalcogen atoms. Another factor that contributes to this transition is a possible change in the quantum confinement of

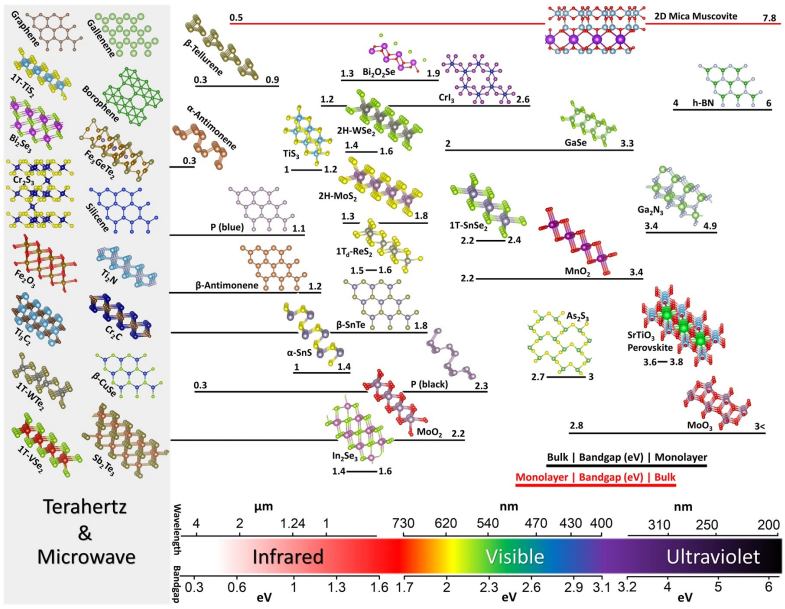

Figure 1.9: *Bandgaps of some 2D materials [72].*

the atoms [50].

While most of TMDs exhibit a semiconductor behavior, especially the systems formed by group VI transition metals, depending on their chemical composition some can exhibit superconductors. As shown in some interesting studies, most of the electric behavior of TMDs is caused by the transition metal part, while the chalcogen atoms barely contribute to its band broadening [73].

Aside from the transition from bulk to monolayer structure, other method to changing the bandgap are possible. Some options are doping [74], mechanical deformation [75] and defects engineering [76].

Another important properties of TMDs is their relatively high electrical conductivity, with values that go as high as 200 $cm^2V^{-1}s^{-1}$ in MoS_2 [43]. The main advantages in using TMDs for their electrical conductivity is that this value can be altered very easily be going from their bulk form to the few or mono layer ones. Furthermore, their electrical conductivities can be altered by doping, giving the possibility to explore behavior like semiconducting, metallic, and charge-density

wave regimes in a low dimensional space [77].

Another consequence of doping is altering the magnetic properties of the pristine material [78]. By doping a TMDs like $MoSe_2$ or $MoTe_2$ with nonmetal elements (e.g. H, B or F), is possible to obtain a total magnetic moment that was not present in their pristine state. For example, the doping of this materials with H developed a antiferromagnetic coupling between the local magnetic moments. Considering all that, these properties open the possibility to use TMDs as high performance electron catalyst.

1.2.5 Optical properties

TMDs optical properties are directly connected to their electrical bandgap. This means that, as explained above, different TMDs will have a variety of photon emission or absorption depending on the energy required for the transition, and so on the chemical composition of the system and on his stacking type. Some TMDs that have a semiconductor behavior, and so that absorb and emit photons in the visible range, have really interesting application in optoelectronic devices [79].

Since TMDs are so optically active, it is possible to use a wide variety of methods to investigate the optical properties. An interesting example is the work of Lee et al. with their characterization of MoS_2 [80]. In their research, they used photolumiscence and Raman spectrography to investigate the band structure of the system. They found that the intensity of the photoluminescence spectrum is inversely proportional to the number of layers of MoS_2, proving in a different way the transition from the direct bandgap in monolayer MoS_2 to the indirect one of its bulk state. Further studies confirmed in this way that the same phenomenon is observed in all of TMDs [81]. In Figure 1.10 is shown the electrical band structures of some TMDs, with the predominant direct and indirect transition highlighted [82]. Another interesting fact is that at room temperature, excitons become the

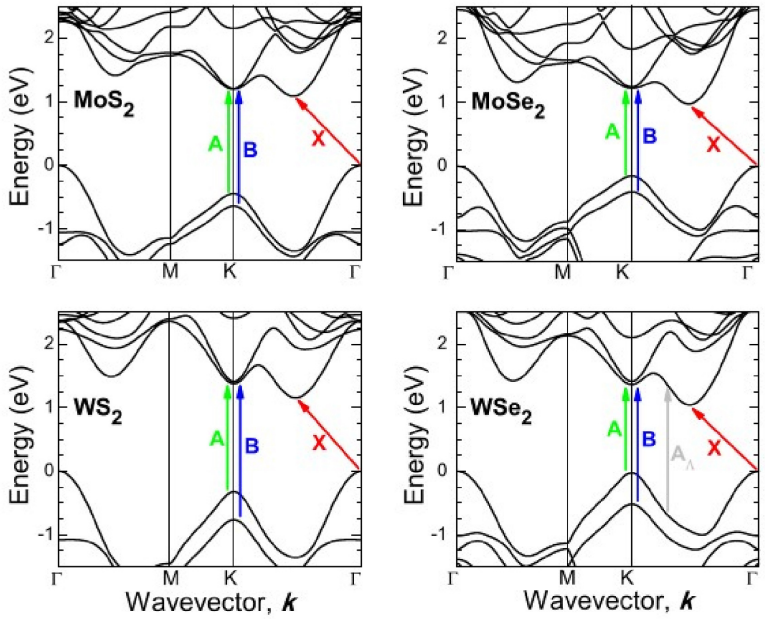

Figure 1.10: *Electronic bands of some TMDs, with the principal electronic transition highlighted [82].*

main agent behind TMDs optical response. In the 2D systems, both normal excitons (i.e. the ones that derive from the Coulomb interactions between TM and chalcogen atoms) and charged excitons (i.e. the ones that derive from the many body interactions of the system) are present [83, 84].

1.2.6 Thermal properties

While classical thermodynamics expects TMDs to have low thermal conductivity, due to the high mass of the atoms that composes the systems, experimental results on pristine TMDs show that this is not always true. While they have in general extremely low thermal conductivity when considering the passage of heat from one TX_2 layer to the next one, their in-plane conductivity is generically not as low as expected. Some examples of in-plane thermal conductivity of the most studied TMDs are: MoS_2 (52 $Wm^{-1}K^{-1}$ [85]), $MoSe_2$ (44 $Wm^{-1}K^{-1}$ [86]), TaS_2 (36 $Wm^{-1}K^{-1}$ [87]), $TaSe_2$ (16 $Wm^{-1}K^{-1}$ [88]).

Those values of thermal conductivity makes them not suitable for thermoelectric

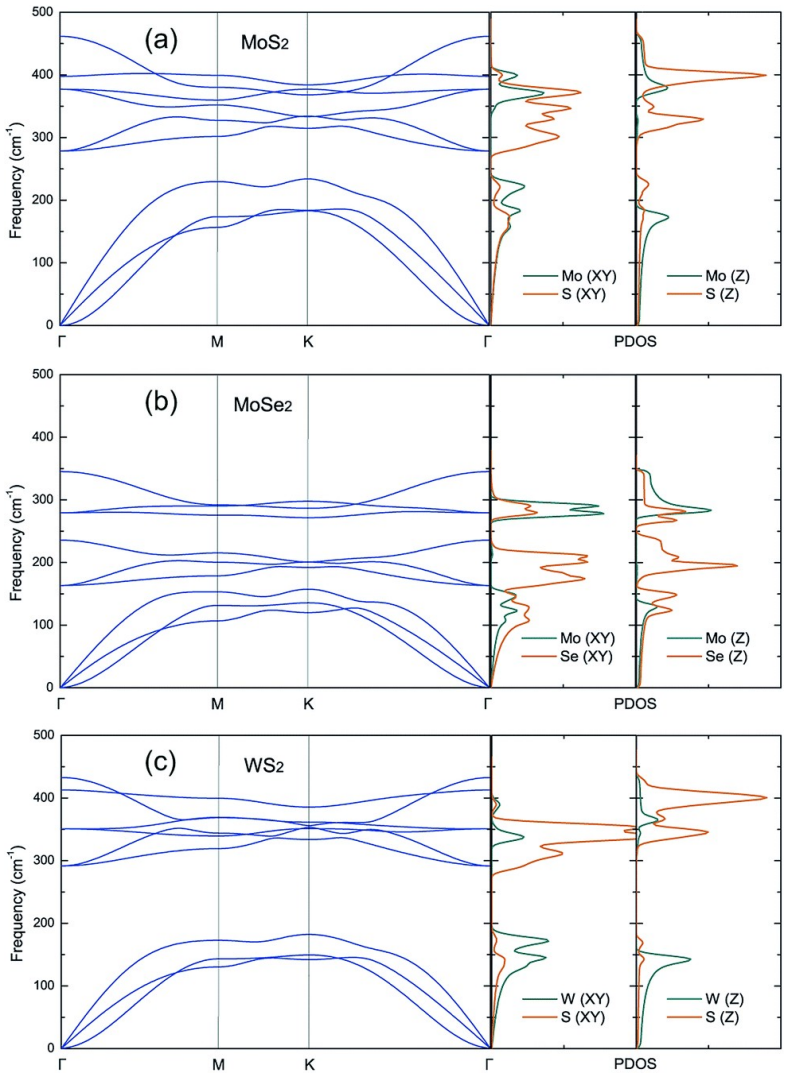

Figure 1.11: *Dispersion curves and phonon density of state of MoS_2, $MoSe_2$ amd WS_2 [89].*

applications, because their high values greatly limits the possible zT. On the other hand, this values are not high enough to be competitive in the heat dissipation applications. Moreover, in their mono-layer state, phonon surface scattering is a problem that further reduces their reliability in this type of applications [90].

Typically, TMDs have show linear phonon dispersion at the center of the Brillouin zone for both the longitudinal and transverse acoustic (LA and TA respectively),

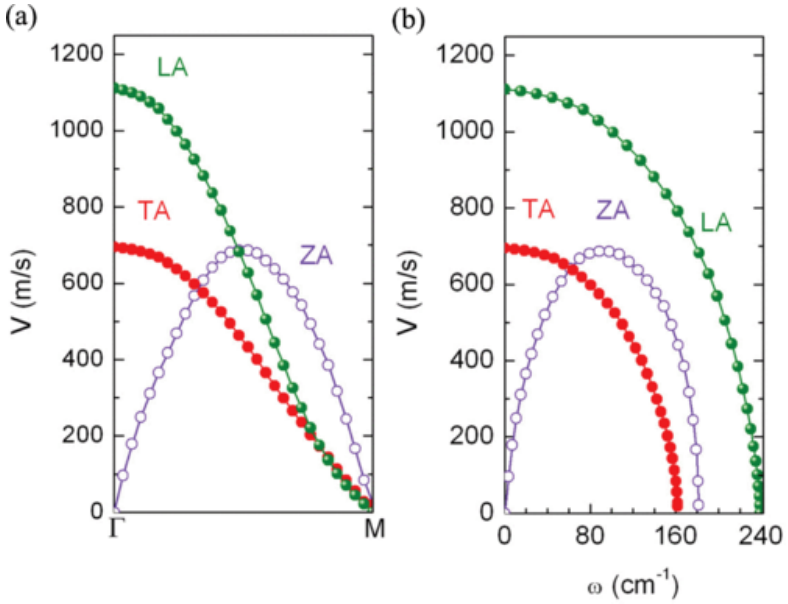

Figure 1.12: *Group velocity of acoustic phonon bands of MoS_2 [91].*

while the flexural acoustic (ZA) shows a quadratic trend. In Figure 1.11 we can see some examples of TMDs dispersion curves and their phonon density of state. In particular, the figures shown are of MoS2, MoSe2 and WS2 in order [89].
Group velocities have generally high values (with typical values around $\sim$ 1000 m/s)but still much smaller than the typical 2D material value (e.g. $v_{LA} = 5953$ m/s for graphene [91]). Another interesting aspect of their group velocities is that while for both LA and TA exhibit a rapid velocity decrease with the increase in frequency, the ZA mode typically shows a low value at low values of frequency, then increase alongside it and after reaching a peak follows the trend of the other two acoustic branches. En example of this can be seen in Figure 1.12 for MoS_2.
In Figure 1.13 s shown the relaxation time and the mean free path fo MoS_2 as reported by [91] Here we can see the typical TMD behavior for such properties. Generally, TMDs exhibit short mean free path that decrease as a function of the frequency. Between the acoustic modes, LA has the longest mean free patch at high frequency.

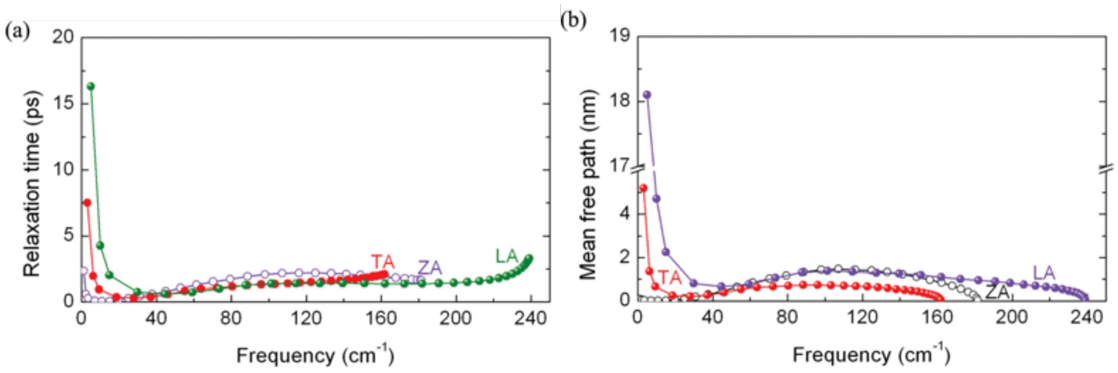

Figure 1.13: *Relaxation time and mean free patch in MoS_2 [91].*

In conclusion, Transition metal dichalcogenides are a really interesting class of materials because of its high mechanical flexibility, electrical and thermal conductivity and their ability to occupy different roles in a complex system depending on the number of layers. Unfortunately, their zT values are too low for extensive use in any thermoelectric applications, thus in the following chapters I will illustrate some methods to reduce their thermal conductivity values along with some explanation of their thermal transport properties.

1.3 Organic molecular crystal

Organic Molecular Crystals are large crystalline structures composed by a multitude of discrete molecular units bonded by weak forces. The nature of these bonds range from van der Waals interactions, $\pi - \pi$ stacking to H-bonds, with some more peculiar interactions like halogen bonds or synthons [92–94].
This bonds give rise to really interesting solids, with properties that strongly depends on the structures. In fact, small variation on the packing or some small polymorfism can lead to large variations in all the properties of the molecule, including optic, electronic, thermal and mechanical properties [95].
Thanks to this variable chemical nature, organic molecular crystals have attracted great attention in the scientific scene for a wide variety of applications, some examples are optoelectronic devices, thermo- or photo- active actuators and thermoelectric generators. Moreover, organic materials are more convenient compared to inorganic ones for a variety of reasons. First of all, they are not toxic and so are viable for bio-medical applications, second organic materials are cheaper to synthesize than inorganic ones, both in term of cost and energy needed for its production [96, 97].

1.3.1 Synthesis

As mentioned above, the properties of organic molecular crystals strongly depends on their structural properties. Molecular packing and polymorfism are linked with the growing condition of the crystal, so understanding the synthesis methods is a crucial step to understand the properties of these materials.
One of the most used technique is the physical vapour transport method. This technique is similar to the chemical vapour method described above, the only

difference being that the physical method does not involves chemical reactions, while the chemical one does. A schematic representation of a physical vapour transport method is shown in Figure 1.14A [98]. The physical vapour transport

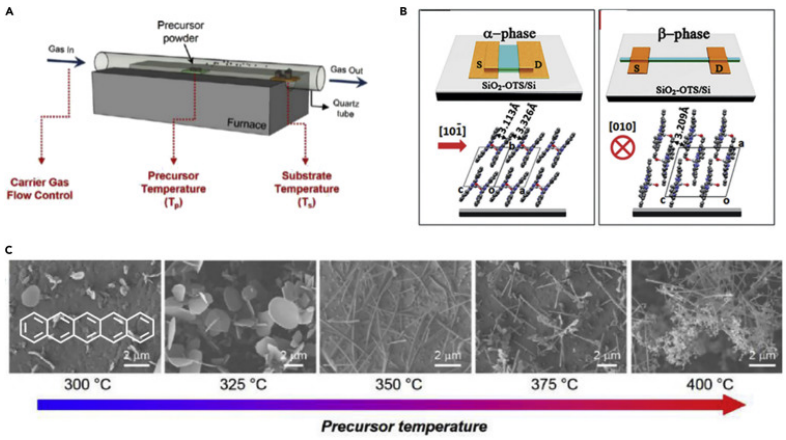

Figure 1.14: *Physical vapour transport method (PVT) apparatus and some examples of materials obtained with it [98]. Panel A shows a schematic representation of a PVT apparatus [99]. Panel B shows the diagram of a PVT device based on α-TiOPc and β-TiOPc [100]. Panel C shows the SEM images that highlight the differences on the morphology of pentacene crystals depending on the temperature [101].*

method consist in heating the precursors until they reach the vapour state, then letting them flow into a chamber with low temperature by a gas and the condensate into a substrate. This method allow high control over the resulting crystal thanks to the many factors that control the technique. Some of such parameters are the gas flow rate, the temperature of both the precursors (T_P) and the substrate (T_S). The general rule is that low deposition rate (i.e. low gas flow rate) and high TS means molecules that stand on the substrate (edge-on orientation) and large domains, due to the high energy that allows the molecule to overcome the substrate forces, while a even lower deposition rate allow the molecules the time to rearrange themselves and the results is an high ordered packed crystal [102, 103]. In Figure 1.14B is reported an example of the different morphology depending on the different interaction precursor-substrate, since β-TiOPc exhibits electronic coupling perpendicular to the current direction, the carrier mobility is as low as

0.1 $cm^2V^{-1}s^{-1}$, while α-TiOPc is 26.8 $cm^2V^{-1}s^{-1}$ [100]. Figure 1.14C shows the difference in pentacene depending of the temperature [101].

Unfortunately, the physical vapour transport method fails in certain circumstances, i.e. when the resulting crystals will have poor thermal stability or when they are formed by large molecules with high molecular weight. In those cases a good alternative are the solution processing methods [104, 105].

Solution processing methods collectively refer to the techniques derived by the recrystalization method and are generally summarized in three different approaches [106]:

1. slow evaporation of solvents;
2. changing the temperature slowly in order to adjust the solubility of organic solvents;
3. slow introduction of poor solvent into a solution in order to obtain crystals with high quality.

In this type of method there are a number of factors that work together to shape the final results: the nature of the solvent used, the evaporation rate, the temperature and the pressure at which the process take place, the concentration of the solvent. A wide variety of techniques follows under the term of solution processing methods, some examples are drop-casting and dip-coating.

The drop-casting method has the peculiarity of not involving any external force. Therefore, the main variable of this process is the solvent. For example, a solvent with high solubility is more likely to produce polycristals, while one with low solubility leads to small crystals. The main disadvantages of this method is the unpredictability of the direction of the growth, while it's main advantage is the simplicity of the process [98].

Instead, the dip-coating method uses external force to facilitate the growth. In

a solution, the substrate with the molecule is first submerged in a solution, then pulled out slowly by the external force. This process results in the production of thin films that generally follow the direction of the force [107]. In addition to the factors described for the drop-casting method, dip-coating technique has additional important variables, such as the entity of the external force (that determines the number of layers in the thin film) and the evaporation rate of the solvent [108]. The main disadvantage of this method is that the introduction of the external force, while it determine the direction of the molecule, may reduce the quality of the crystals that it produces [106].

1.3.2 Structural properties

As stated above, the morphology of the organic molecular crystal directly impacts on its properties, it follows that structural properties are a matter of study of great importance.
In contrast with inorganic structures, in these crystals not only are present interactions between atoms, but even interactions between molecules. These interactions take the shape of bonds weaker than the covalent ones that bound the atoms of the single molecules, i.e. van der Waals forces, hydrogen bonds,$\pi - \pi$ interactions and halogen bonds [109].

Hydrogen bonds Hydrogen bonds are one of the more common type of interactions in organic systems. Identified with the formula $X - H \cdots A$, it is a stable and directional bond with an electrostatic nature that depends on the electronegativity of X and A [110].

$\pi - \pi$ interactions $\pi - \pi$ interactions are bonds that involves the π orbitals of a system. These interactions are controlled by the electrostatic interactions between aromatic rings and have an quadrupole moment associated with them [111]. However, usually the orientation of the molecules in the crystal is determined by the much stronger hydrogen bonds [112].

Halogen bonds The halogen bond is an interaction between an electrophilic region of an halogen atom X and a nucleophilic region of a molecule Y-Z, resulting in a bond identified as $R - X \cdots Y - Z$, where R is the rest of the halogen molecule. This type of bond in similar to the hydrogen one, both in force and in the directionability, but is hydrophobic [113].
The type of interaction that bond the molecules that compose the crystal is the primary responsible for the packing type of the organic molecular crystal. As can be seen in Figure 1.15, there are four principal stacking arrangements [114].

In Figure 1.15, panel A represents the herringbone packing arrangement that is the pattern typical of crystals dominated by hydrogen bonds. This arrangement usually is associated with 2D systems. Panel B represents the motif called cofacial herringbone, typical of crystal with a almost equal presence of both hydrogen and $\pi - \pi$ bonds. This pattern can be either 1D or 2D depending on the ratio between the two types of bonds. The pattern in panel C is called one-dimensional slipped stacking and is typical of systems dominated by $\pi - \pi$ interactions. Lastly, panel D represents the two-dimensional brickwork motif, a pattern that is observed in systems dominated by $\pi - \pi$ interactions and by substituent effects [114].
Not only the packing arrangement, but even the molecular orientation has a not trivial impact on the properties of the crystal. As we can see in Figure 1.16, there

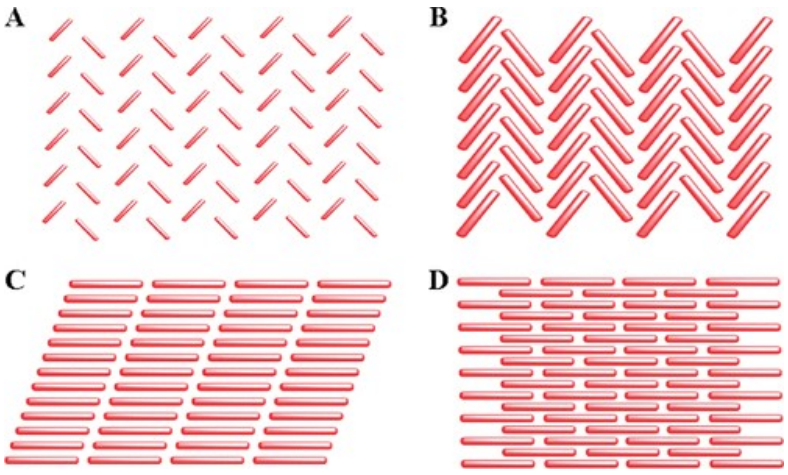

Figure 1.15: *Typical stacking arrangements of organic molecular crystal. Panel A shows the herringbone packing arrangement. Panel B shows the called cofacial herringbone arrangement. Panel C shows the one-dimensional slipped stacking. Panel D shows two-dimensional brickwork motif [114].*

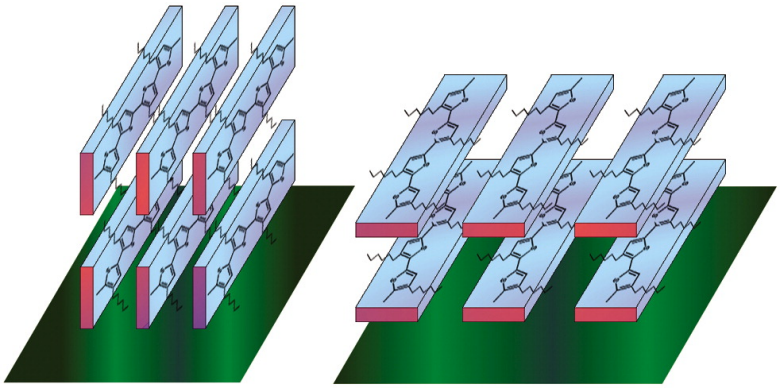

Figure 1.16: *Molecular orientation of organic molecular crystal. The first orientation is called face-on, the second edge-on [115].*

are two typical orientations: the face-on and the edge-on. Typically, face-on crystals have higher carrier mobility and are employed in the field of green energy like photovoltaic, while edge-on crystals is employed in parallel charge transport like in transistors.

1.3.3 Electric properties

Thanks to their weak bonds, the organic molecular crystals have electronic properties heavily linked with the structure of their precursors. In fact, the main contribution on electronic properties is the delocalized electrons that originate from the carbon-carbon bonds. Those electrons in a large systems typically form a conducting π energy band and a second anti-bonding band $\pi*$, limited by the highest occupied molecular orbital (HOMO) and the lowest unoccupied molecular orbital (LUMO). Usually the band gap is defined by the gap between the π and $\pi*$ bands and it depends on the lenght of the molecule components. A representation of this can be found in Figure 1.17, where is shown both the band gap in function of the length and its changes after the introduction of dopants. Usual values of the band gaps are between 1.5 to 3.0 eV [1]. As we can see in Figure 1.17, band

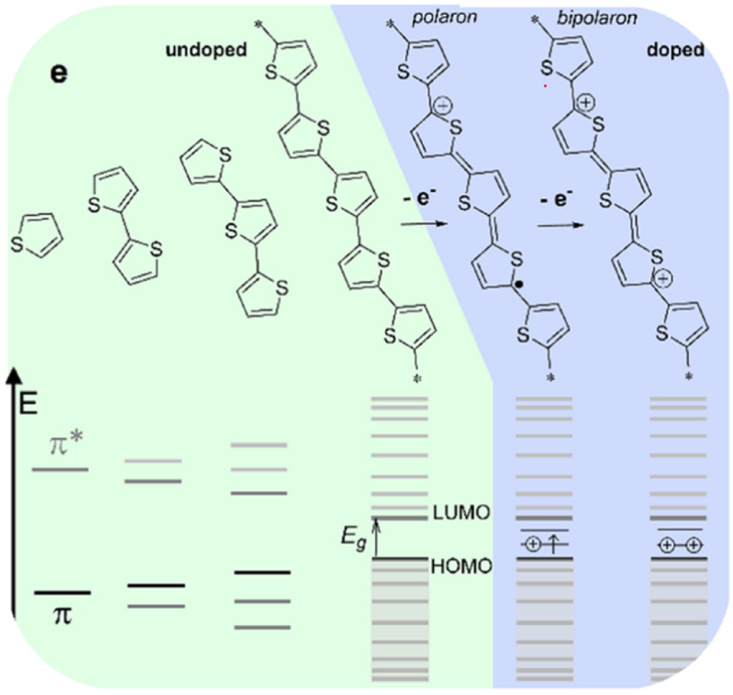

Figure 1.17: *Dependence on the molecule length and on the presence of doping of the band gap in molecular organic systems [1].*

gap and so electrical condictivity can be greatly changed by the introduction of doping. In contrast with inorganic materials, an important factor in the doping of organic molecular crystals is the miscibility value, a factor that quantifies the molecular contact between dopant and organic molecule [116]. Doping can increase electrical conductivity by orders of magnitude, reaching values as high as $sigma > 100\text{Scm}^{-1}$ (PEDOT:Tos [117]).

1.3.4 Optical properties

Since the forces that bond together the molecules in organic molecular crystals are generally much weaker than the covalent forces that bond inorganic materials, the large solids resulting of this bonding typically retains the same optical properties than the molecules that composes them [118].
Typically, in organic systems, the optical absorption spectra reflects the coupling between exciton and vibrational modes of the molecules that compose the system [119].

1.3.5 Thermal properties

Thermal properties are a matter of great importance on the study of organic molecular crystals. In fact, most of the systems that are part of this category have small free energy difference between polymorphs, so a variation in the temperature can change the phase at which the crystal is stable [120]. The cause of this variations in free energy are almost entirely dependent on the anharmonirc properties of the crystals, on the difference in the van der Waals forces due to temperature and in a small part by the thermal expansion coefficient [121].

Aside from that, organic molecular crystals typically shows low thermal conductivities, a trait that is a huge advantage in applications like thermoelectricity. Typical values of lattice thermal conductivity in this class of material range between 0.2 and 0.5 $Wm^{-1}K^{-1}$, while the electronic part is often negligible [27].

In contrast to their charge transport properties, most organic molecular crystals show low anisotropy in their thermal transport behavior. For example, the [1]benzothieno[3,2-b][1]benzothiophene (BTBT) and 2,7-dioctyl[1]benzothieno[3,2-b][1]benzothiophene (C8-BTBT-C8) systems show respectively anisotropy factors below 1.8 (BTBT) and 2.8 (C8-BTBT-C8) [122].

An interesting strategy to reduce the thermal conductivity of this type of materials is the functionalization with inorganic side chains to the aromatic rings. In fact, upon functionalization, the aforementioned BTBT system (now C8-BTBT-C8) halves its thermal conductivity, when looking at both its isotropic approximation and at the single directions [122]. Interestingly enough, this phenomenon is not dependent on the single side chain, since similar reductions are observed in Cn-BTBT-Cn systems, with n = 8,10,12 [123]. Similar results are obtained for the dinaphtho[2,3-b:2′,3′-f]thieno[3,2-b]thiophene (DNTT) system and its deritavies [124].

In contrast, in poly(3,4-ethylenedioxythiophene) (PEDOT), another class of material belonging to the category of molecular organic crystals, the thermal conductivity is found to be extremely direction dependent, with its main contribution derived from the direction of the chains, while the contributions of the perpendicular directions are significantly lower [125].

Moreover, in some PEDOT was found that after a controlled polymerization of the material leads to a shift in its Raman bands, suggesting an increase in its mean chain length and mean molecular weight. These factors have been proven beneficial to thermoelectric properties, suggesting controlled polymerization as a

viable strategy to increase the zT of this type of systems [126, 127]. Indeed, studies have reported a dependence of thermal conductivity on the length of the polymer chains: the longer are the polymer chains, the larger the system thermal conductivity [128], making a PEDOT formed only by monomers the compound of this category with the lowest thermal conductivity possible [125].
Additionally, using the proper polymerization techniques it is possible to obtain compounds where amorphous and crystalline regions coexist. In such materials, the charge transport is enhanced while the thermal conductivity is reduced, further increasing its thermoelectric performance [129]. In fact, the crystalline PEDOT have significantly higher thermal conductivity than the amorphous ones, by almost two orders of magnitude, making a mixed compound the perfect candidate for thermoelectric applications [128].
Another strategy to control the thermal conductivity of a PEDOT is to reduce its dimensionality. A recent study demonstrated how a one dimensional PEDOT possesses characteristic of superdiffusive thermal transport, greatly increasing its thermal conductivity value in comparison to its three dimensional counterpart, which did not show any anomalous behavior [130].

In conclusion, Organic molecular are a really interesting class of material for thermoelectric applications, thanks to their high flexibility, low thermal conductivity and high electrical conductivity especially in doped systems. However much of the properties regarding thermal transport remains up to debate, in particular when considering all the factors that can change with the rising of the temperature from 0 K.
In the following chapters of this thesis I will provide through two different examples (BTBT and DNTT) a description of such termal transport properties in order to shred some light in the Organic Molecular Crystal discourse and provide some insights about their use as thermoelectric generators.

Chapter 2

Methods

In order to understand ad predict the thermal behavior of thermoelectric systems, first-principle simulations based on density functional theory (DFT) and molecular dynamics (MD) have become necessary tools.

These methods enable the investigation of fundamental quantities such as the electronic band structure, phonon dispersion, and thermal transport, with atomistic precision, providing direct insight into the mechanisms that govern heat transport in materials.

This chapter describes the main theoretical concepts behind the study of thermal transport in crystalline materials, alongside a brief description of the main computational frameworks employed throughout this work.

In the first two sections offer a brief review on the phonon theory and its application on the calculation of thermal transport properties. Subsequently, the theoretical foundations of density functional theory, molecular dynamics simulations, and related techniques are introduced.

2.1 Lattice dynamics

In order to understand the thermal properties of a material, is imperative the study of the collective motion of the atoms in the solid. This subject is what we refer to lattice dynamics.

While the approximation of *static lattice* is useful to describe a crystal structure, if we want to understand more complex phenomena we have to abandon it by introducing some factors.

First of all, we have to go beyond the assumption that ions (i.e. the nucleus of the atom and the core electrons) have fixed positions. Only if we assume the ions capable of moving from their lattice position we can explain common properties such as thermal expansion, sound propagation, thermal conductivity and more. So it is pivotal to develop a theory that help us explain the movement of the ions.

Secondly, we have to introduce a finite mass for the ion, that is assumed infinite in the *static lattice* approximation. In order to implement that, remembering the principle of quantum mechanics that links a mass with a mean square momentum even a $T = 0K$, we call R_1 the mean position of an ion in a Bravais lattice.

In order to develop a theory that explains *lattice dynamics*, we can make some assumption. The first is to consider a many-body potential energy $U(R)$ that is associated with the motion of the atoms and includes both the Coulomb interaction between different ions and the kinetic energy of the single ion.

The second approximation is to consider that the motion of the ions is small compared to the lattice spacing, so that the displacement produced by the motion does not influence the lattice structure. This approximation may seem large, but there are many experimental data that confirms it.

Using this assumption, we can use a power series to expand the potential energy

$U = U(R)$:

$$U = \sum_{lb,i} \left.\frac{\partial U}{\partial u_i(lb)}\right|_0 u_i(lb) + \frac{1}{2} \sum_{\substack{l_1b_1,i_1 \\ l_2b_2,i_2}} \left.\frac{\partial^2 U}{\partial u_{i_1}(l_1b_1)u_{i_2}(l_2b_2)}\right|_0 u_{i_1}(lb)u_{i_2}(l'b') + ...$$

$$= \sum_{n=1}^{+\infty} \frac{1}{n!} \sum_{\substack{i_1,i_2,...,i_n \\ l_1b_1,l_2b_2,...,l_nb_n}} U_{i_1,i_2,...,i_n}(l_1b_1, l_2b_2, ..., l_nb_n)u_{i_1}(l_1b_1)u_{i_2}(l_2b_2)\ldots u_{i_n}(l_nb_n)$$

$$where: \left.\frac{\partial^n U}{\partial u_{i_1}(l_1b_1)u_{i_2}(l_2b_2)\ldots u_{i_n}(l_nb_n)}\right|_0 = U_{i_1,i_2,...,i_n}(l_1b_1, l_2b_2, ..., l_nb_n). \tag{2.1}$$

Since we are considering only small displacements from the equilibrium position u(lb), we can stop our expansion at the first non-zero term:

$$U^{harmonical}_{classical} = \frac{1}{2} \sum_{\substack{l_1b_1,i_1 \\ l_2b_2,i_2}} U_{i_1i_2}(l_1b_1, l_2b_2)u_{i_1}(l_1b_1)u_{i_2}(l_2b_2). \tag{2.2}$$

This approximation is often referred as *harmonic approximation* because this potential energy is equivalent to a system composed by n harmonic oscillators with $U_{i_1,i_2,...,i_n}(l_1b_1, l_2b_2, ..., l_nb_n)$ as their *force constants*.

These force constants must be chosen in order to satisfy the following conditions for U:

1. invariance under rigid body translactions or rotations,

2. invariance under symmetry operation of the crystal.

The first condition implies that:

$$\sum_{l_1b_1,l_2b_2,...,l_nb_n} U_{i_1,i_2,...,i_n}(l_1b_1, l_2b_2, ..., l_nb_n) = 0, \tag{2.3}$$

while the second allow us the used of group theory to determine which element of the matrix composed by the force constants of any given order are non-zero.

2.1.1 The harmonic linear chain

The simplest representation of a solid with the properties discussed above is the *monoatomic linear chain* with harmonic approximation. In this representation, we consider a one-dimensional Bravais crystal as a series of N identical ion with mass M and connected by a force in the form of a harmonic spring, as discussed above. Using Born-Von Karman boundary conditions, we can write the ion position as $R_l = la$, where a is the lattice parameter and $l = 0,1,2,...,N-1$. A visualization of such system can be found in Figure 2.1. With this representation, we can see

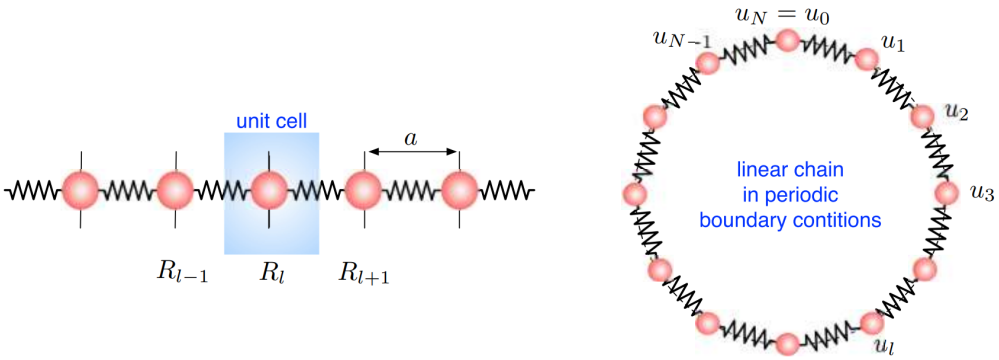

Figure 2.1: *On the left a monoatomic linear chain in which the atoms are bonded with a spring, the unit call is highlighted in blue and the lattice constant is a. On the right the same chain with Born-Von Karman boundary conditions [131].*

a longitudial vibration as a displacement patter in which the ions move in the direction of the chain. Indicating the force constant of the effective spring a $\gamma^{(L)}$, we can use the classical equation of motion:

$$M\ddot{u}_l = \gamma^{(L)}(u_{i+1} + u_{i-1} - 2u_i). \tag{2.4}$$

Using simple mechanics, we can use the typical solution for a vibrating wire. This solution should have a form similar to:

$$u_l = \frac{1}{\sqrt{NM}}|A_q|\cos[qR_l - \omega(q)t + \varphi(q)]. \tag{2.5}$$

In this equation, $\frac{1}{\sqrt{NM}}$ is a normalizing factor, q is the wave-number of the wave, A_q is the amplitude, φ_q is the initial phase and $\omega(q)$ is the angular frequency.
By using in Equation 2.4 the solution presented in Equation 2.5, we obtain the *dispersion relation*:

$$M\omega^2(q) = 2\gamma^{(L)}[1 - \cos(qa)] = 4\gamma^{(L)} \sin^2(\frac{1}{2}qa). \tag{2.6}$$

Since the crystal has transnational invariance, we can consider only a small portion of all the possible solution, i.e. we will consider only the results obtained by q inside the first Brillouin zone, or $q \in [-\pi/a, +\pi/a]$. A visual representation os the dispersion relations obtained in this way can be seen in Figure 2.2 Using the boundary conditions, we can further reduce the number of allowed values of q by imposing that $u_0 = u_n$:

$$q = \frac{2\pi}{a}\frac{\varepsilon}{N} \tag{2.7}$$

with ε = 0,1,2, ..., $N - 1$. This means that only N independent wave-vectors are possible in a monoatomic linear chain.

The group velocity of these waves can be obtained as $v_g = d\omega(q)/dq$. In the limit $q \to 0$, the Equation 2.6 reduces to $\omega(q) = [\gamma^{(L)}/M]^{\frac{1}{2}}qa$ and his group velocity is $v_g = \sqrt{\gamma^{(L)}/M}a$. This description is equivalent to the description of a longitudinal sound wave, as such we can call $\omega = \omega^{(L)}$ *acoustic dispersion*.
The same reasoning can be applied to transverse oscillations. In this case, we use the transverse force constants $\gamma^{(T)}$ instead of the longitudinal ones $\gamma^{(L)}$, and the results are equivalent. Typically, $\gamma^{(T)} < \gamma^{(L)}$. In linear monoatomic chains there are two transverse direction that have the same force constants and degenerate dispersion relations.
Using Equation 2.7, we can now substitute in Equation 2.5 in order to obtain the expression for the lth ion's displacements:

$$u_l = \frac{1}{\sqrt{NM}} \sum_q |A_q| \cos[qR_l - \omega(q)t + \varphi(q)]. \tag{2.8}$$

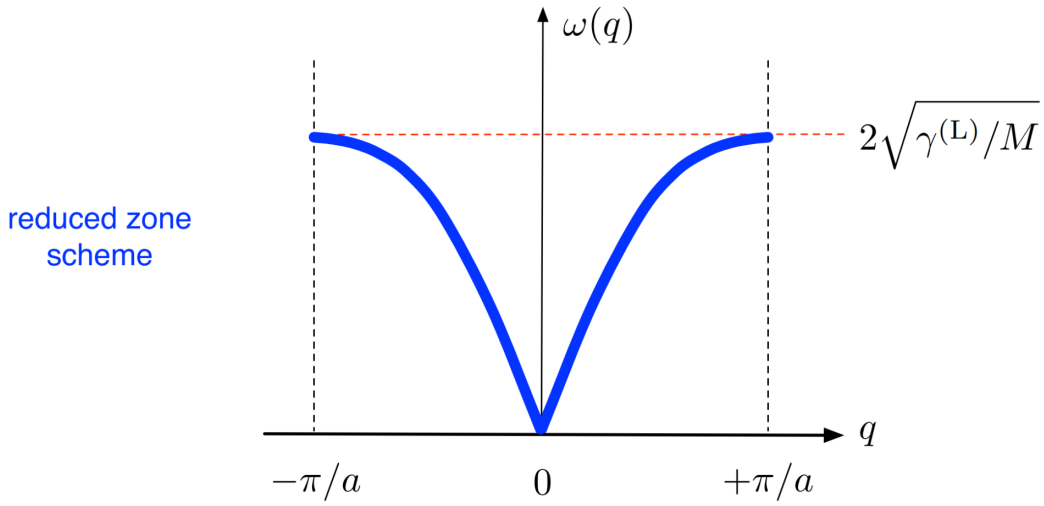

Figure 2.2: *Dispersion relation $\omega = \omega(q)$ for the longitudinal vibrations in the first Brillouin zone of a monoatomic chain [131].*

In summary, using this approximation, we can see how each ion oscillate around its equilibrium position in the same way that an harmonic oscillator and that the entire chain can be represented as by N distinct normal vibrational modes.

We can now introduce some complexity in this model by adding a different ion in the chain. In this situation, we have the first atom in position $R_{l,1} = R_l + R_1$, mass M_1 and effective spring $\gamma^{(L)}$, and the other in position $R_{l,2} = R_l + R_2$, mass M_2 and effective spring $\xi^{(L)}$, where R_l is the position of the lth unit cell and R_1 and R_2 are the position of the two ions inside the cell. A representation of this system is shown in Figure 2.3.

By generalizing Equation 2.4, we obtain a set of two differential equations:

$$\begin{cases} M_1\ddot{u}_{l,1} = \gamma^{(L)}(u_{l,2} - u_{l,1}) + \xi^{(L)}(u_{l-1,2} - u_{l,1}) \\ M_2\ddot{u}_{l,2} = \xi^{(L)}(u_{l+1,1} - u_{l,2}) + \gamma^{(L)}(u_{l,1} - u_{l,2}) \end{cases} . \tag{2.9}$$

Since we want solutions with a similar form to Equation 2.8, we can write:

$$u_i = \frac{1}{\sqrt{NM_i}} \sum_q |A_q||a_i(q)| \cos[qR_i - \omega(q)t + \varphi(q) + \phi_i(q)]. \tag{2.10}$$

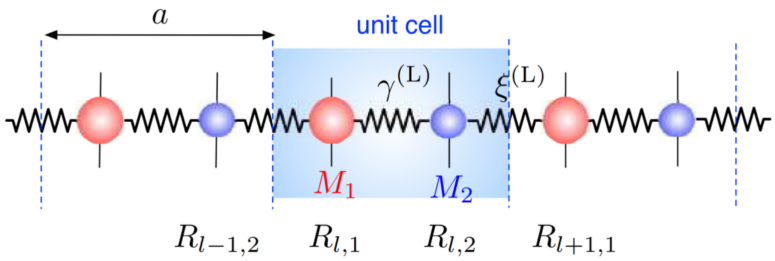

Figure 2.3: *A biatomic linear chain in which the atoms are bonded with a spring, the unit call is highlighted in blue and the lattice constant is a [131].*

Here we did some change in nomenclature: in both amplitude and phase we have separated the part that depends on boundary condition ($|A_q|$ and $\varphi(q)$) and the part that is determined by the equation of motion ($|a_i(q)|$ and $\phi_i(q)$) and the index i is referring to the ion in the basis.

With this in mind, we can use these solutions to solve Equation 2.9, obtaining:

$$\begin{pmatrix} D_{11} & D_{12} \\ D_{21} & D_{22} \end{pmatrix} \begin{pmatrix} a_1 \\ a_2 \end{pmatrix} = \omega^2 \begin{pmatrix} a_1 \\ a_2 \end{pmatrix}, \tag{2.11}$$

This is a Hermitean matrix called *dynamical matrix* $D(\boldsymbol{q})$ whose elements D_{ij} whit $i = 1$ and $j = 2$ are:

$$D_{11} = \frac{\gamma^{(L)} + \xi^{(L)}}{M_1} \tag{2.12}$$

$$D_{12} = -\frac{\gamma^{(L)}}{\sqrt{M_1 M_2}} \exp[iq(R_{l,2} - R_{l,1})] - \frac{\xi^{(L)}}{\sqrt{M_1 M_2}} \exp[iq(R_{l-1,2} - R_{l,1})], \tag{2.13}$$

$$D_{21} = -\frac{\gamma^{(L)}}{\sqrt{M_1 M_2}} \exp[iq(R_{l,1} - R_{l,2})] - \frac{\xi^{(L)}}{\sqrt{M_1 M_2}} \exp[iq(R_{l+1,1} - R_{l,2})], \tag{2.14}$$

$$D_{22} = \frac{\gamma^{(L)} + \xi^{(L)}}{M_2}. \tag{2.15}$$

By solving the Equation 2.11, we obtain the two eigenvalues $\omega = \omega_{\pm}(q)$ that are the dispersion relations for the chain and the eigenvectors are related to the ionic displacements. The quantities $a_i(q)$ are called *polarization vectors*.

This highlight a very important feature: in the diatomic chain, two vibrational

frequencies $\omega_{\pm}(q)$ are associated with each wave-number q.

By inserting the values of $\omega_{\pm}(q)$ in Equation 2.11 is possible to show that is impossible to obtain numerical values for the eigenvectors $a_1^{\pm}(q)$ and $a_2^{\pm}(q)$ but we can determine only their ratio. By using some simplifications (namely $M_1 = M_2$ and $|a_1^{\pm}(q)|^2 + |a_2^{\pm}(q)|^2 = 1$), we can prove that:

$$\frac{a_1^+(q)}{a_2^+(q)} = -\frac{A(q)}{|A(q)|} = -\frac{a_1^-(q)}{a_2^-(q)}. \tag{2.16}$$

Here we can see that with these limitations, in the lower branch the unit cell always oscillate in phase while in the upper branch it always oscillate in phase opposition. This affirmation can be generalized to *ions within the same unit cell vibrate in-phase for the lower modes and in phase opposition for upper modes.* In ionic crystals, vibrations with long wavelength in the upper branch generate a fluctuating electric dipole because the ions have opposite charge. This newly generated dipole can interact with electromagnetic radiation, thus generating an optical response. For this fact, the upper branch is also referred as *optical branch.* Here we can see how the lower dispersion ω_- is very reminiscent of the dispersion of the monoatomic chain, for this reason we call this dispersion *acoustic branch.*

The new figure obtained for the biatomic chain is shown in Figure 2.4.

As for the monoatomic chain, here too the transverse modes are present and for each q wi will have two degenerate transverse modes. In total, six dispersion relations are present in this case.

2.1.2 3D crystals

Starting from the solutions developed in above, we can obtain the equation for the dynamics in a 3D crystal via a process of generalization.

Since now we have a crystal with N_{atom} atoms per unit cell, we will have $3N_{atom}$

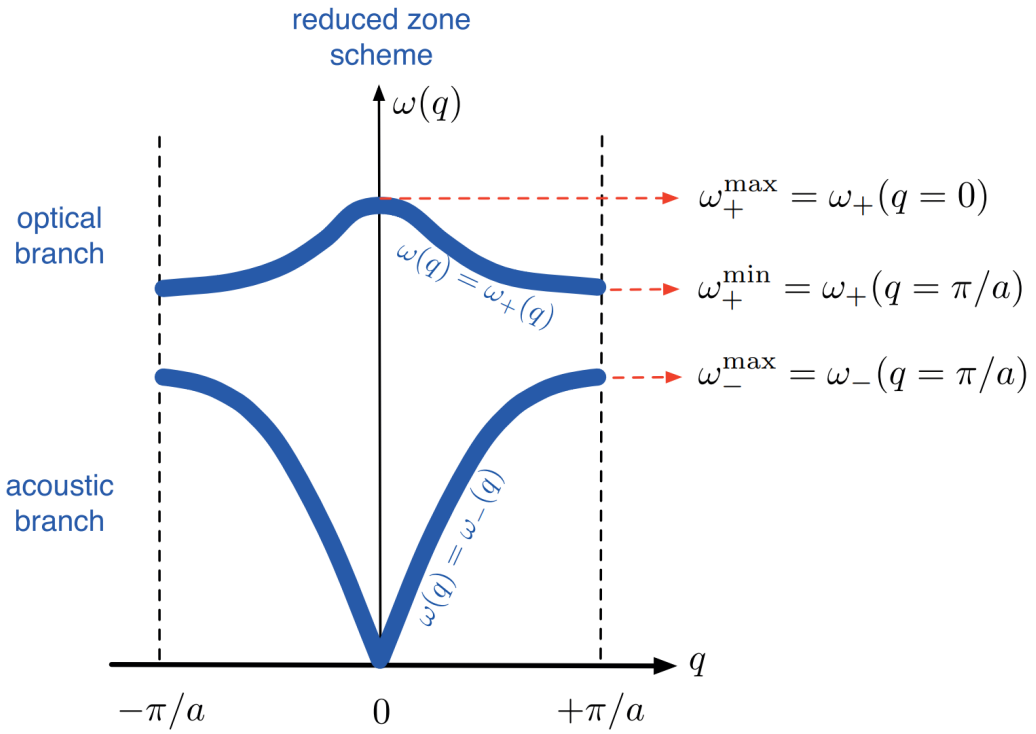

Figure 2.4: *Dispersion relation $\omega = \omega_{\pm}(q)$ for the longitudinal vibrations in the first Brillouin zone of a biatomic chain.[131].*

ionic degrees of freedom and so we will have the same number of dispersion relations. Of the $3N_{atom}$ dispersion relations, 3 are associated with acoustic branches and the remaining with optical ones.

We can now generalize Equation 2.10 to obtain the equation of motion for a 3D crystal

$$M_b \ddot{u}_i(lb) = -\sum_{jl'b'} U_{ij}(lb, l'b') u_j(l'b'), \tag{2.17}$$

and so we want solution for a generic bth atom of this form:

$$u_i(lb) = \frac{a_i(b|\boldsymbol{q})}{\sqrt{M_b}} e^{i\boldsymbol{q}\cdot\boldsymbol{R}_l} e^{-i\omega t}, \tag{2.18}$$

where $\boldsymbol{q}$ is the wave-vector of the vibrational wave and $a_i(b|\boldsymbol{q}$ its corresponding amplitude.

Continuing with the generalization, we can obtain a new version for Equation 2.11:

$$\sum_{jb'} D_{ij}(bb'|\boldsymbol{q})a_j(b'|\boldsymbol{q}) = \omega^2 a_i(b|\boldsymbol{q}). \tag{2.19}$$

$D_{ij}(bb'|\boldsymbol{q})$ are the elements of the new dynamical matrix and can be calculated using:

$$D_{ij}(bb'|\boldsymbol{q}) = \frac{1}{\sqrt{M_b M_{b'}}} \sum_{l'} U_{ij}(lb, l'b') e^{i\boldsymbol{q}\cdot(\boldsymbol{R}_l - \boldsymbol{R}_{l'})}. \tag{2.20}$$

$U_{ij}(lb, l'b')$ are the force constants of the crystal and in case of a ideal crystal it does not depend on the absolute values of l and l' but only on their difference, for this reason we can use a single summation over the index l'.

As for the biatomic case, even in a generic 3D crystal the diagonal matrix is Hermitean. Thus, the solution of the lattice dynamics of a 3D crystal is equivalent to the diagonalization of its dynamical matrix.

In conclusion, if we have a crystal with N_{cell} cells, the number of independent vibrational modes goes to $N_{cell} \times 3N_{atom}$. Each mode will be named by using the indexes s and $\boldsymbol{q}$, where s is the branch index and $\boldsymbol{q}$ is the wave-vector.

2.1.3 Quantum lattice dynamics

Lastly, in order to describe a realistic system, we have to introduce quantum dynamics calculation in our description of the 3D crystal. Experimental findings highlight the shortcomings of a classical description, such as the experimental proof of a reduction in the specific heat along with the temperature, that in the classical description should be independent of the temperature (Dulong-Petit law). The general concept for introducing quantum dynamics in the theory developed above is to replace the description of springs characterized by elastic constant γ with one-dimensional quantum harmonic oscillators. Each of this oscillators have

energy values of $(n_{s\boldsymbol{q}} + 1/2)\hbar\omega_s(\boldsymbol{q})$ where $n_{s\boldsymbol{q}} = 0,1,2,...$ is the vibrational quantum number and $\omega_s(\boldsymbol{q})$ is the dispersion relation obtained by solving Equation 2.19. The states with energy level of these harmonic oscillators can be seen as composed by $n_{s\boldsymbol{q}}$ energy quanta of value $\hbar\omega_s(\boldsymbol{q})$ called phonons.

With this notation, we can describe both dynamical and thermal properties of a crystal using the characteristics of a gas of the pseudo-particles called phonons.

Similarly to other pseudo-particles, like photos, phonons do not have any mass, have an associated energy of $\hbar\omega_s(\boldsymbol{q})$ and have a momentum $\hbar\boldsymbol{q}$. They are delocalised since their momentum is known exactly and so, as stated by the uncertainty principle, their position cannot be determine. Often phonon momentum is also referred as crystal momentum. In fact, we know from the section above that in the classical description that the vibration is transnational invariant ($\omega(\boldsymbol{q}) = \omega(\boldsymbol{q}) + \boldsymbol{G}$ with $\boldsymbol{G}$ a reciprocal lattice vector.). Since this property must be valid even in the quantum description, we can notice that the same phonon can be describe by either $\hbar\boldsymbol{q}$ and $\hbar\boldsymbol{q} + \boldsymbol{G}$.

Furthermore, phonons can be created or annihilated, since the total number of phonons is not conserved. The average number of phonons in a crystal can be obtained with the Bose-Einstein statistics:

$$n_{BE}(s\boldsymbol{q}, T) = \frac{1}{exp\left[\frac{\hbar\omega_s(\boldsymbol{q})}{k_B T}\right] - 1}, \tag{2.21}$$

proving that phonons are bosons.

With this in mind, we can write the quantum vibrational energy of an harmonic crystal as:

$$\langle U \rangle = U_{harmonic}^{quantum} = \sum_{s\boldsymbol{q}} [n_{BE}(s\boldsymbol{q}, T) + 1/2]\hbar\omega_s(\boldsymbol{q}). \tag{2.22}$$

This description allow us to quickly demonstrate the crystalline zero point energy: for $T \to 0$ $U_{harmonic}^{quantum} = 1/2 \sum_{s\boldsymbol{q}} \hbar\omega_s(\boldsymbol{q}) \neq 0$.

2.1.4 Vibrational density of states

Another important property associated with phonons is the vibrational density of states (vDOS or simply DOS) $G(\omega)$. This property represents the number of phonons with a frequency comprehended in the infinitesimal interval $[\omega, \omega + d\omega]$. In order to develop the formalism needed, we will consider first a model crystal, composed of only one atomic species. By using Born-von Karman periodic boundary conditions and setting the nearest neighbors distance to a, we obtain with this model a 3D generalization of the monoatomic chain discussed above.
Using this logic, we can derive the phonon wave-vectors $\boldsymbol{q}$ by generalizing Equation 2.7: $q_i = 2\pi\epsilon_i/L$ with $L = na$, $i = x, y, z$ and $\epsilon_i = 0,1,2,...,(N_{atom} - 1)$. Thus, the number density in the reciprocal space is given by $V/(2\pi)^3$. In order to obtain the DOS in the frequency range between $\omega, \omega + d\omega$, we need only to simply consider the product of this number density with the infinitesimal volume of the spherical shell in reciprocal space $4\pi q^2 dq$ comprised between two surfaces with constant frequency ω and $\omega + d\omega$. This statement is correct only in the approximation of phonon properties that do not depend on their direction. Using this simplification, we can write the DOS as:

$$G(\omega)d\omega = \frac{V}{(2\pi)^3} 4\pi q^2 dq. \tag{2.23}$$

This is a important assumption greatly simplifies the formalism, but it fails in many situation and as such must be removed.
To do so, we need to introduce the branch DOS as $G(\omega) = \sum_s G_s(\omega)$. This branch DOS then can be described using the same principle as before, i.e. as the product between the number density of the phonons and the infinitesimal volume $d\boldsymbol{q}$. Since now we are taking in consideration the direction of phonons, the two surfaces that we used before to delimit the volume are not spherical anymore and theoretically

can be of any shape. Thus we can define the element of volume as:

$$d\boldsymbol{q} = \int_{s_{\omega_s}} dS_{\omega_s} dq_{\perp}(\boldsymbol{q}) \tag{2.24}$$

where $dq_{\perp}(\boldsymbol{q})$ is the distance between the surface with $\omega_s(\boldsymbol{q}) = constant$ and the one with $\omega_s(\boldsymbol{q}) + d\omega = constant$ that can change for every $\boldsymbol{q}$ value and dS_{ω_s} is an element of the first surface. Since we can write $d\omega = |\nabla_q \omega(\boldsymbol{q})| dq_{\perp}(\boldsymbol{q})$, we can further generalize the expression as:

$$d\boldsymbol{q} = d\omega \int_{s_{\omega_s}} \frac{dS_{\omega_s}}{|\nabla_q \omega_s(\boldsymbol{q})|}. \tag{2.25}$$

Using this expression, we can obtain the total DOS as:

$$G(\omega) = \sum_s G_s(\omega) = \frac{V}{(2\pi)^3} \sum_s \int_{s_{\omega_s}} \frac{dS_{\omega_s}}{|\nabla_q \omega_s(\boldsymbol{q})|}. \tag{2.26}$$

With this description an important phenomenon is revealed: since the gradient of $\omega_s(\boldsymbol{q})$ is the group velocity of the associated phonon, we have that when such velocity is zero (e.g. when we have a flat phonon branch) there is a singularity in the DOS called *van Hove singularity*. Furthermore, when we work in a small frequency range, from Equation 2.26 we can deduce that $G(\omega) \sim \omega^2$.

Equation 2.26 is the most general formulation for the DOS, but can be difficult to apply in practice, even with the computational techniques used in this thesis. Therefore, we use the more practical formulation:

$$G(\omega) = \frac{V}{(2\pi)^3} \sum_s \int \delta(\omega - \omega_s(\boldsymbol{q})) d\boldsymbol{q}, \tag{2.27}$$

where the integral is over all the first Brillouin Zone.

Finally, it is important to remind that all of this description of lattice dynamics relies upon the harmonic approximation, that allow us the truncation of the Taylor expansion in Equation 2.1. While for the description of lattice dynamics is sufficient, plenty of other important effects are only described by overcoming it and

using a description that is referred as anharmonic, i.e. that includes other terms of the Taylor expansion. Many experimental evidences support the anharmonic description, some examples are:

1. when we apply some strain in a crystalline crystal, it produces a different variation in the volume depending on the direction of the strain, suggesting that the ions are not confined in their lattice position by an harmonic potential;

2. if we use an harmonic potential, the mean ion-ion distance would be constant even with the increase in temperature and this contradicts thermal expansion;

3. there would be not dampening in the phonons produced by the material, leading to infinite lattice thermal conductivity.

Therefore, even if harmonic approximation give us a good description of lattice dynamics, it fails in predicting some of the most important thermal behaviors of a crystal.

2.2 Thermal transport

In this section we will analyze the thermal transport in a crystal, both using a more classical approach and by expanding the phonon description developed above with some anharmonic effects.

2.2.1 Fourier Law

The first description of heat transport is the classical Fourier Law. This phenomenological description of the phenomenon was proven to be sufficiently accurate by numerous experimental results and it si still useful in various theoretical scenarios.

In order to discuss thermal transport, let us consider the system presented in Figure 2.5. Here we have an homogeneous crystal that is subjected to an heat gradient in the x direction dT/dx. This heat gradient is generated by two thermostats in the left and right extremities of the crystal, the first heated to a temperature T_{hot} and the second T_{cold}, with $T_{hot} > T_{cold}$. After some time, the system will evolve to a steady state with a temperature profile shown with the white line. In this

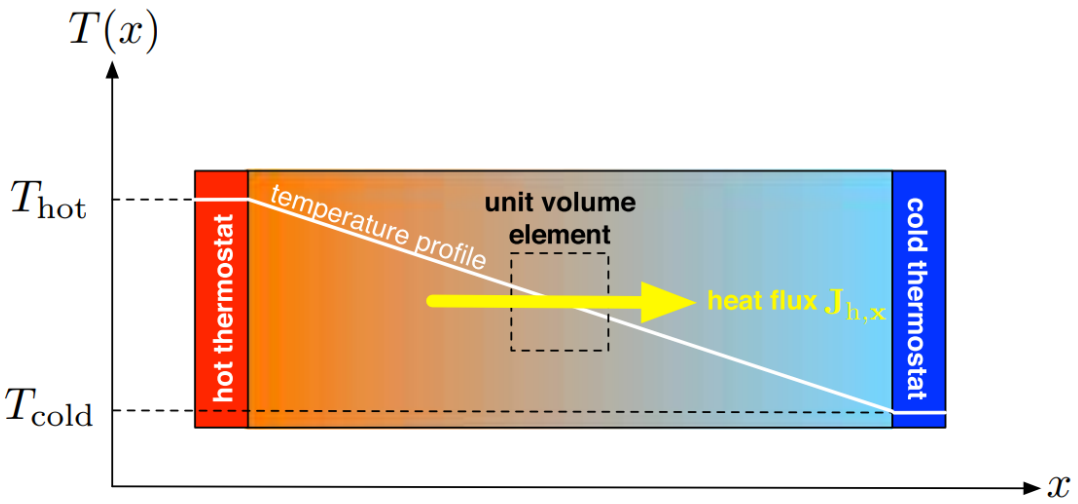

Figure 2.5: *Homogeneous crystal with two thermostats in its extremities, heated at two different temperatures $T_{hot} > T_{cold}$. The white line represents the thermal gradient in the steady state [131].*

situation, we can define the amount of thermal energy that crosses an unit of area normal to the x direction per unit of time as the heat flux $J_{h,x}$ along the x axis

using the Fourier Law:

$$J_{h,x} = -\kappa_x \frac{dT}{dx}. \tag{2.28}$$

Here we can see that there is a proportionality constant between the thermal gradient and the heat flux. This constant is called thermal conductivity and it is the determining factor in heat conduction: high thermal conductivity allow efficient thermal dissipation and characterize a good thermal conductor, while low thermal conductivity is the characteristic properties of a thermal insulator.
While the Fourier Law can predict surprisingly well the values of thermal conductivity in most material, it does not give a satisfying description on the thermal conduction mechanism of a crystal. For this reason, the Fourier Law is often referred as a macroscopic description of thermal transport. In some cases, this description is enough to give all the information needed for a particular study, but in most of other cases we want to develop a microscopical description of thermal transport.

2.2.2 Boltzmann Transport Equation

In a microscopical view of thermal transport, we have to identify the mechanism which are involved in the phenomenon. The first and most general heat carriers are the lattice vibrations that we can treat with the phonon formalism. The second type of carriers are the conducting electrons, active especially in electric conductors. Using this approach, we have to divide the thermal conductivity in two contributions, $\kappa_{lattice}$ is the one associated with the lattice vibrations and κ_{ele} is the one dependent on the conduction electrons. We can say that:

$$\kappa = \kappa_{lattice} + \kappa_{ele} \tag{2.29}$$

In this section we will focus on the calculation of $\kappa_{lattice}$.

Using the phonon theory, we can describe the heat flux in Figure 2.5 as:

$$J_{h,x} = \frac{1}{V} \sum_{s,\boldsymbol{q}} \hbar\omega_s(\boldsymbol{q}) \overline{n}(s\boldsymbol{q}, T) v_{g,x}(s\boldsymbol{q}). \tag{2.30}$$

Here we see that the heat flux is normalized using the volume crossed by the thermal flux (v) and by a sum over all phonons of their properties, in particular: the energy carried by the single phonon $\hbar\omega_s(\boldsymbol{q})$, their group velocity $v_{g,x}(s\boldsymbol{q})$ and the phonon population $\overline{n}(s\boldsymbol{q}, T)$.

In Equation 2.30 we can see that the phonon population is not given by the Bose-Einstein distribution like it was in Equation 2.22, but is a generic population $\overline{n}(s\boldsymbol{q}, T)$. The Bose-Einstein distribution is a correct representation for system at an equilibrium situation while we are currently discussing a steady state. Therefore, we have to develop a theory to understand the relation between the two.

To do so, we use another simplification, called the single mode relaxation time approximation (SM-RTA). This means that we consider each phonon population relaxes independently to all the other phonon populations. With this approximation, we are able to define the relation in this way:

$$\frac{\partial \overline{n}(s\boldsymbol{q}, T)}{\partial t} = -\frac{\overline{n}(s\boldsymbol{q}, T) - n_{BE}(s\boldsymbol{q}, T)}{\tau_{s\boldsymbol{q}}}. \tag{2.31}$$

In this equation is present the therm $\tau_{s\boldsymbol{q}}$ that is the single-mode relaxation time that is coincident with the phonon lifetime. As stated above, in the harmonic approximation phonons do not dampen in a crystal, so the lifetime of a phonon should be infinite. Therefore, we need to extend our previous phonon description with some anharmonic properties. This will be done later in this section.

In order to continue our explanation of thermal transport, we use again the situation described in Figure 2.5. If we look at the volume element identified by the dotted line, we can write a continuity equation for the thermal current:

$$\frac{1}{V}\frac{\partial U}{\partial t} = \frac{\partial J_{h,x}}{\partial x}, \tag{2.32}$$

where U is the enrgy of the system as written in Equation 2.22, with the correction $n_{BE}(s\boldsymbol{q},T) \rightarrow \overline{n}(s\boldsymbol{q},T)$ in order to consider the non-equilibrium situation.
Using this expression for the potential energy and Equation 2.30, we can obtain from Equation 2.32 the following expression:

$$\frac{\partial \overline{n}(s\boldsymbol{q},T)}{\partial t} - v_{g,x}(s\boldsymbol{q})\frac{\partial \overline{n}(s\boldsymbol{q},T)}{\partial T}\frac{\partial T}{\partial x} = 0 \tag{2.33}$$

Now, assuming that the temperature dependence of the new population $\overline{n}(s\boldsymbol{q},T)$ and the one obtained with the Bose-Einstein distribution are the same and inserting the Equation 2.31 in this last expression we can obtain a explicit relation for the non-equilibrium population:

$$\overline{n}(s\boldsymbol{q},T) = n_{BE}(s\boldsymbol{q},T) - \tau_{s\boldsymbol{q}} v_{g,x}(s\boldsymbol{q})\frac{\partial n_{BE}(s\boldsymbol{q},T)}{\partial T}\frac{\partial T}{\partial x} \tag{2.34}$$

This expression is called the linearised Boltzmann Transport Equation (BTE) and was introduced in the early work of Peierls in 1929[132].
Using this, we can finally write an expression for the heat flux that uses only known quantities:

$$J_{h,x} = \frac{1}{V}\sum_{s,\boldsymbol{q}} \hbar\omega_s(\boldsymbol{q}) n_{BE}(s\boldsymbol{q},T) v_{g,x}(s\boldsymbol{q}) - \frac{1}{V}\sum_{s,\boldsymbol{q}} \hbar\omega_s(\boldsymbol{q})\tau_{s\boldsymbol{q}} v^2_{g,x}(s\boldsymbol{q})\frac{\partial n_{BE}(s\boldsymbol{q},T)}{\partial T}\frac{\partial T}{\partial x}. \tag{2.35}$$

Here we see that the heat flux depend on two separate term, the first one ($\sum_{s,\boldsymbol{q}} \hbar\omega_s(\boldsymbol{q}) n_{BE}(s\boldsymbol{q},T) v_{g,x}(s\boldsymbol{q})$) is compose by only equilibrium properties, thus cannot contribute to thermal currents, and the second term only depends on the non equilibrium properties.
By comparing this with the Fourier Law in Equation 2.28, we can derive the expression for the thermal conductivity:

$$\kappa_x(T) = \frac{1}{V}\sum_{s,\boldsymbol{q}} \hbar\omega_s(\boldsymbol{q})\tau_{s\boldsymbol{q}} v^2_{g,x}(s\boldsymbol{q})\frac{\partial n_{BE}(s\boldsymbol{q},T)}{\partial T}. \tag{2.36}$$

This expression for the thermal conductivity is the one most commonly used in calculation, and will be used in some of the work presented here as well.

As we can see, this in contrast with the constant term obtained with Fourier Law, the BTE thermal conductivity has a strong dependence with the temperature. By studying this equation, we can detect three separate trends:

1. very low temperature: $\kappa_x(T) \sim T^3$, since the temperature is too low to have a important population in the vibrational modes, the thermal conductivity is dominated by the increasing creation rate of phonons and by the specific heat;

2. intermediate temperature: $\kappa_x(T) \sim exp[(1/b)T_D/T]$, here the annihilation of phonons due to the scattering begin to lower the thermal conductivity but it is balanced by phonon creation, T_D is the Debye temperature of the system and $2 < b < 3$ for most materials;

3. high temperatures: $\kappa_x(T) \sim T^{-d}$, in this regime phonon annihilation is prevalent, for most materials $1 < d < 2$.

In Figure 2.6 we can find the thermal conductivity of crystalline silicon calculated with the help of the code `QUANTUM ESPRESSO` with this theory and can see a representation of its three trends.

2.2.3 Anharmonic properties of phonons

As stated above, the harmonic description of phonons is not sufficient to describe thermal transport properties, but we have to expand our description introducing some hanarmonic properties.
In a physical view, anharmonicity can be seen as the interaction between different phonons. However, the strength of such interactions is much weaker than the interactions that are treated in the harmonic representation, therefore we can treat the anharmonicity as a perturbation of the harmonic methodology. Experimentally,

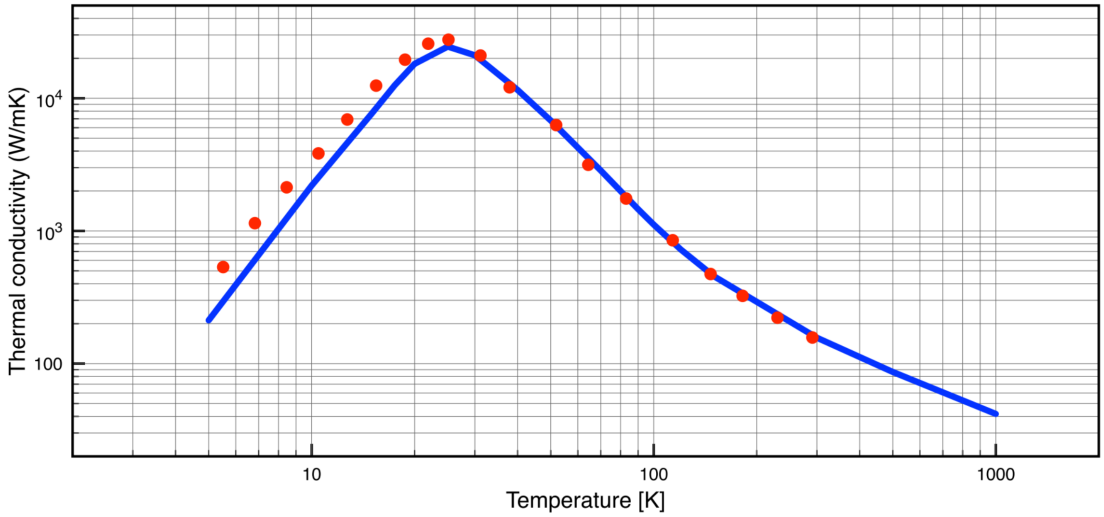

Figure 2.6: *Blue line: thermal conductivity of crystalline silicon calculated using the SM-RTA-BTE approach with the help of* `QUANTUM ESPRESSO` *[131]. The red dots are the experimental data [133].*

we see that the fully harmonic characterization of a material can well reproduce the experimental phonon spectra, but only by introducing anharmonicity we can describe the transition between different harmonic eigenstates of the quantum oscillator.

As a general rule, we can view the nth order of anarmonicity (i.e. the nth order of the Taylor expansion in Equation 2.1 when $n > 3$) as the potential energy associated with the interaction among n phonons. During these n-phonons scattering events, since phonons are bosons, and hence they do not conserve their total number, we can assist to phenomena of annihilation and creation.

In order to discuss more in detail of these events, let us take the example of 3 phonons scattering events. During these, only the three modes $(s_1, \boldsymbol{q}_1)$, $(s_2, \boldsymbol{q}_2)$ and $(s_3, \boldsymbol{q}_3)$ play an active part in the interaction. These three modes can interact

in two possible ways, the phonon generation event:

$$\begin{cases} n_{s_1,\boldsymbol{q}_1} \rightarrow n_{s_1,\boldsymbol{q}_1} - 1 \\ n_{s_2,\boldsymbol{q}_2} \rightarrow n_{s_2,\boldsymbol{q}_2} + 1 \\ n_{s_3,\boldsymbol{q}_3} \rightarrow n_{s_3,\boldsymbol{q}_3} + 1 \end{cases} \tag{2.37}$$

and phonon annihilation event:

$$\begin{cases} n_{s_1,\boldsymbol{q}_1} \rightarrow n_{s_1,\boldsymbol{q}_1} - 1 \\ n_{s_2,\boldsymbol{q}_2} \rightarrow n_{s_2,\boldsymbol{q}_2} - 1 \\ n_{s_3,\boldsymbol{q}_3} \rightarrow n_{s_3,\boldsymbol{q}_3} + 1 \end{cases} . \tag{2.38}$$

We can use the Fermi golden rule to predict the rate of such events:

$$P^{(3)}_{i\rightarrow f} = \frac{2\pi}{\hbar} |\left\langle f|\hat{V}_3|i\right\rangle|^2 \delta(\hbar\omega_{s_1,\boldsymbol{q}_1} \mp \hbar\omega_{s_2,\boldsymbol{q}_2} - \hbar\omega_{s_3,\boldsymbol{q}_3}), \tag{2.39}$$

where $\hat{V}_3$ is te quantum operator that describes the anharmonic perturbation. $\langle i|$ represents the initial state of the system, i.e. the state $(n_{s_1,\boldsymbol{q}_1}, n_{s_2,\boldsymbol{q}_2}, n_{s_3,\boldsymbol{q}_3})$, while $|f\rangle$ is the final state of the system, i.e. $(n_{s_1,\boldsymbol{q}_1} - 1, n_{s_2,\boldsymbol{q}_2} \pm 1, n_{s_3,\boldsymbol{q}_3} + 1)$.
Furthermore, the δ term implies that the total energy of the phonon system is always conserved, limiting the possible type of three phonons events. In Figure 2.7 the possible and impossible events are shown. Another important property of the scattering events is that they conserve the total crystal momentum. As stated above, the same phonon can be described by both $\hbar\boldsymbol{q}$ and $\hbar\boldsymbol{q} + \boldsymbol{G}$, where $\boldsymbol{G}$ is a reciprocal lattice vector. Because of this, the conservation of crystal momentum can be written as:

$$\begin{aligned} \hbar\boldsymbol{q}_1 &= \hbar\boldsymbol{q}_2 + \hbar\boldsymbol{q}_3 \pm \hbar\boldsymbol{G} \qquad \text{for phonon creation} \\ \hbar\boldsymbol{q}_1 + \hbar\boldsymbol{q}_2 &= \hbar\boldsymbol{q}_3 \pm \hbar\boldsymbol{G} \quad \text{for phonon annihilation.} \end{aligned} \tag{2.40}$$

Thanks to this description, we can observe that there are two types of phonon-phonon interactions:

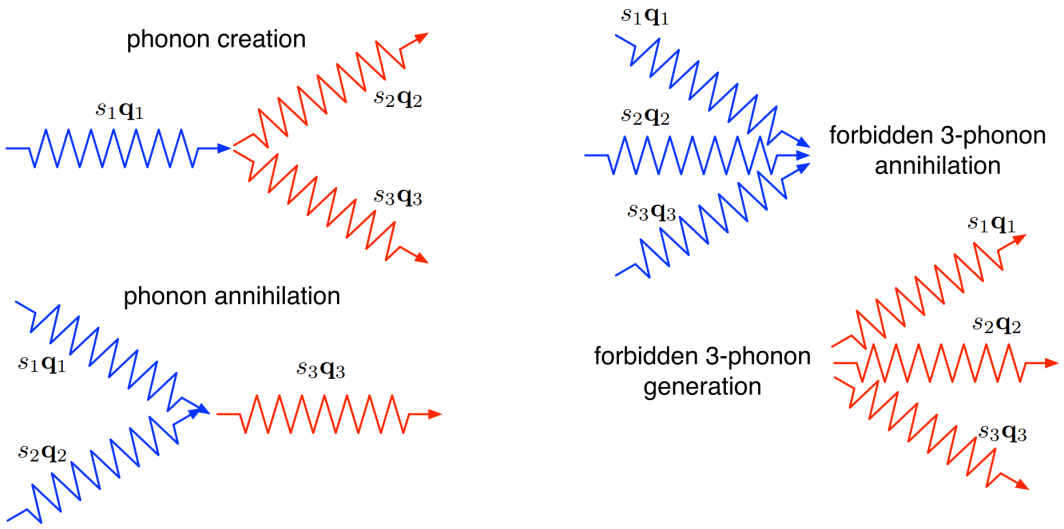

Figure 2.7: *Schematic representation of permitted (left) and forbidden (right) three phonons scattering events [131].*

1. normal processes: events with $\boldsymbol{G} = 0$;
2. Umklapp processes: events with $\boldsymbol{G} \neq 0$, in this type of process the true momentum is not conserved.

Finally, there are two other important properties of phonons that are derive from the anharmonic description.

The first is a slight shift in their harmonic frequencies, $\omega_s(\boldsymbol{q}) \rightarrow \omega_s(\boldsymbol{q}) + \Delta_{s\boldsymbol{q}}$. Usually the difference in frequency $\Delta_{s\boldsymbol{q}}$ is negligible, but in crystals with strong anharmonicity can have a major impact.

The second is the dampening in amplitude. By developing the version of Equation 2.39 that describes an annihilation process, is possible to derive a finite phonon lifetime $\tau_{s\boldsymbol{q}^{(3)}}$. This phonon lifetime is obtained considering only phonon-phonon annihilation events, but other types of annihilation can be observed in crystals, such as interaction with impurities or defects, thus is important to define a phonon lifetime that takes into account all types of annihilation events. By calling $\tau^{(n)}_{s\boldsymbol{q}}$ the annihilation event of the n-type, we can use the Matthiessen rule to obtain the

total relaxation time $\tau_{s\boldsymbol{q}}$:

$$\frac{1}{\tau_{s\boldsymbol{q}}} = \sum_n \frac{1}{\tau_{s\boldsymbol{q}}^{(n)}}. \tag{2.41}$$

This approximation is proven correct in many circumstances, so its use is justified. All the reasoning used in the description of third order anharmonicity is applicable even to terms with an higher level of anharmonicity. Thus, the higher the order m, the more complex the quantum operator $\hat{V}_m$ will be and minor the effect on the description of the system will be.

2.3 Density functional theory

The Density Functional Theory (DFT) [134] is a theoretical framework based on the assumption that a many-electron system can be uniquely described through its electronic density, $n(\mathbf{r})$.

In this way, the original problem, which involves calculating 3N variables, is reduced to a problem depending only on three variables. Moreover, the computational cost is drastically reduced when using DFT-based codes.

The first steps toward this theory were made in 1927 with the Thomas–Fermi model. However, the modern formulation of DFT has its origins in a later development, which took shape following the publication and proof of the two Hohenberg–Kohn theorems [135], which, for the sake of clarity, are reported below.

First theorem For every system of interacting particles in an external potential $V_{ext}(\mathbf{r})$, the potential $V_{ext}(\mathbf{r})$ is uniquely determined, up to an additive constant, by the ground state electron density $n_0(\mathbf{r})$.

Second theorem an universal energy functional $E[n]$ can be defined in terms of the electron density $n(\mathbf{r})$, valid for any external potential $V_{ext}(\mathbf{r})$. for a particular V_{ext}, the ground-state energy of the system corresponds to the

minimum value of this functional, and the density $n(\mathbf{r})$ that minimizes it is the ground-state density $n_0(\mathbf{r})$.

Thanks to these theorems, an exact formalism for DFT can be developed.
Having demonstrated that the electronic density uniquely characterizes the ground-state wave-function, which in turn has a one-to-one correspondence with the external potential $V_{ext}(\mathbf{r})$, Hohenberg and Kohn argued that the knowledge o f$n(\mathbf{r})$ implies the knowledge of all terms of the Hamiltonian operator.
To apply these concepts to practical calculations, they introduced two functionals. The first is a universal functional, $F[n(\mathbf{r})]$, which does not depend on the external potential and can be written as $F[n(\mathbf{r})] = \langle \Psi_N | T + V_{ee} | \Psi_N \rangle$.
The second is the energy functional, $E[n(\mathbf{r}), V_{ext}(\mathbf{r})]$ which can be obtained from the first as follows:

$$E[n(\mathbf{r}), V_{ext}(\mathbf{r})] = \int d\mathbf{r} \Big[V_{ext}(\mathbf{r}) + F[n(\mathbf{r})] \Big]. \tag{2.42}$$

Hohenberg and Kohn also demonstrated that the minimum of this energy functional corresponds to the ground-state energy of the system:

$$E_0 = \min_{n(\mathbf{r})} E[n(\mathbf{r}), V_{ext}(\mathbf{r})]. \tag{2.43}$$

In order to determine the ground-state energy of the system, it is therefore necessary to find an explicit form of the energy functional, but in many cases this is not straightforward.
To address this problem, in 1965 Kohn and Sham decomposed the functional F[n(**r**)] expressing it in the following form:

$$F[n(\mathbf{r})] = T_S[n(\mathbf{r})] + \frac{1}{2} \int n(\mathbf{r}) \Phi(\mathbf{r}) d\mathbf{r} + E_{XC}[n(\mathbf{r})]. \tag{2.44}$$

Where T_S is the kinetic energy that the system would have within the independent-electron approximation, $\Phi(\mathbf{r})$ is the classical Coulomb potential, and $E_{XC}[n(\mathbf{r})]$ is

the exchange–correlation energy (XCE), also referred as exchange–correlation functional.

If all these terms could be determined exactly, Equation 2.44 would be an exact relation, since the exchange–correlation term would account for all quantum exchange and correlation effects.

Unfortunately, however, an exact expression for this term has not yet been found, so it is necessary to use approximations to estimate its value.

It can be shown that the system's energy can be expressed in terms of the exchange–correlation energy alone and the energy the system would have in the case of non-interacting particles (ϵ_i):

$$E = \sum_{i=1}^{N} \epsilon_i + E_{XC}[n(\mathbf{r})] - \int V_{xc}(\mathbf{r}) n(\mathbf{r'}) d\mathbf{r'} + \frac{1}{2} \int \frac{n(\mathbf{r}) n(\mathbf{r'})}{|\mathbf{r} - \mathbf{r'}|} d\mathbf{r} d\mathbf{r'}. \tag{2.45}$$

Furthermore, it can also be shown that the electronic density can be obtained as a combination of wave-functions for the non-interacting system (ϕ_i):

$$n(\mathbf{r}) = \sum_{i=1}^{N} |f_i \phi_i(\mathbf{r})|^2, \quad f_i = 0{,}1 \tag{2.46}$$

where f_i are the occupation numbers of the ith state.

Using this formalism, it is possible to solve the many-body problem by solving the Schrödinger equation for the associated system of non-interacting electrons:

$$\left[-\frac{\hbar^2}{2m} \nabla^2 + V(\mathbf{r}) \right] \phi_i(\mathbf{r}) = \epsilon_i \phi_i(\mathbf{r}), \quad i = 1{,}2, ..., N. \tag{2.47}$$

This system of equation is called Kohn and Sham equations and usually they are solved by means of self-consistent approaches [136]. Using these equation in combination with a correct correlation energy, the many-body electronic problem can, in principle, be solved exactly.

In summary, DFT is an exact theory that allows the determination, in a relatively simple way, all the relevant properties of the system under investigation, although it is based on a functional that is, in practice, unknown.

2.3.1 The exchange–correlation energy

As stated above, in order to use the DFT methodology it is imperative to chose a representation for the exchange–correlation energy.

The simplest functional is the based on the Local Density Approximation (LDA), in which the system is considered as an homogeneous electron gas with a density equal to $n(\mathbf{r})$. Using this approximation, the exchange-correlation energy of a single electron e_{XC} can be obtained analytically. It is possible to write e_{XC} as the sum of two terms, one representing the exchange energy e_X and the second the correlation one e_C, $e_{XC} = e_X + e_C$. Then, we can analytically determine the two terms by [137]:

$$e_x(n) = -\frac{0.458}{r_s(n)} \tag{2.48a}$$

$$e_c(n) = \frac{0.44}{r_s(n) + 7.8} \tag{2.48b}$$

$$r_s(n) = \left(\frac{3}{4\pi n}\right)^{\frac{1}{3}} \tag{2.48c}$$

where r_s is the radius of a sphere that, on average, is occupied by one electron in the homogeneous electron gas (HEG) approximation.

Once the e_{XC} expression is found, the exchange–correlation energy can be calculated by integrating e_{XC}:

$$E_{XC}^{LDA}[n(\mathbf{r})] = \int e_{XC}(\mathbf{r}, [n(\mathbf{r})])n(\mathbf{r})d\mathbf{r}. \tag{2.49}$$

The LDA is accurate for small systems composed by few atoms, but shows its limitations when performing calculations on larger systems.

Therefore, using the LDA as a starting point, there are a number of new functional that try to overcome the LDA limitations. For example, a great shortcoming of the LDA is not accounting for the variations of electron density, that it has been resolved with a slightly more complex functional called Generalized Gradient Approximation (GGA) [138].

In the GGA approach, the exchange-correlation functional depends not only on the electron density but even from its gradient $e_{XC}[n(\mathbf{r}), \nabla n(\mathbf{r})]$. The terms of Equation 2.48 are then changed accordingly and the total E_{XC} of the system is obtained through Equation 2.49 once again.

The GGA scheme provides better results than the LDA one. However, in most systems the required level of accuracy is still not achieved.

A possible improvement is offered by the so-called meta-GGA functionals, that are functionals similar to GGA but they include higher-order derivatives of the electron density. The DFT meta-GGA schemes yield reasonably accurate results, which can be further improved through the use of hybrid functionals. The idea behind this class of functionals is to compute part of the exchange functional exactly, using the Hartree–Fock method, while the remaining part is approximated through one of the approaches described above (LDA, GGA, etc.).

Unfortunately, the more complex the representation of the E_{XC}, the higher the computational cost associated with the calculations becomes. Fort this reason, the choice of representation is a non-trivial problem that must be considered depending on the systems under study.

In thi thesis, the optimal balance between accuracy and computational cost was achieved by the use of the PBESOL representation, an in-between approximation that is more complex of the GGA but still in a lower level than meta-GGA [139].

2.4 Molecular dynamics

In this section, a brief summary of the Molecular Dynamics (MD) simulation methodology will be presented.

Molecular dynamics is a methodology of computational simulations that allows

the numerical solution of the classical Newtonian equation of motion:

$$m\ddot{\mathbf{r}} = \mathbf{f}_i \qquad \mathbf{f}_i = -\frac{\partial}{\partial \mathbf{r}_i} U \tag{2.50}$$

where $\mathbf{f}_i$ is the forces acting on the atoms, $\mathbf{r}^N = (\mathbf{r}_1, \mathbf{r}_2, ..., \mathbf{r}_N)$ is the set of 3N atomic coordinates and $U(\mathbf{R}^N)$ is the potential energy.

$U(\mathbf{R}^N)$ is usually split in two components: the bonding potential energy U_b and the non-bonding potential energy U_{nb}. In order to compute the forces from the Newton equations and thus the atomic trajectories, it is necessary to give a form of this two components. The non-bonding part of the potential energy, also called interatomic potential, can be considered as the sum of energies derived from various types of interactions:

$$U_[nb] = \sum_i u(\mathbf{r}_i) + \sum_i \sum_{j>i} v(\mathbf{r}_i \mathbf{r}_j) + ... \tag{2.51}$$

where $u(\mathbf{r}_i)$ is a potential derived from external forces and usually can be neglected, $v(\mathbf{r}_i \mathbf{r}_j)$ is the potential derived from the two body interactions. There are more terms derived from three-body, four-body and so on interaction that we are choosing to neglect.

Therefore, it is necessary to give an explicit formulation of the two-body term. The simplest representation is the Lennard-Jones potential, that despite its simplicity is able to give great results in certain materials such as liquid argon, and can be used as a testing potential even in more complex system. The representation of such potential can be written as:

$$v^{LJ}(r) = 4\epsilon \left[\left(\frac{\sigma}{r}\right)^{12} - \left(\frac{\sigma}{r}\right)^{6} \right] \tag{2.52}$$

where σ is the diameter and ϵ is the well depth.

The bonding part of the potential usually is a complex function that relies upon a parametrization that depends on the specific simulated system. The set of parameters that are used to determine the bonding potential energy is called a force-field

and choosing the correct representation is often pivotal to obtain accurate results from the simulation. Usually, these parameters include: bond distancing, bend and torsion angles, dihedral angle and some cross-terms such as stretch-bend forces. Typically, these potentials are modeled after experimental parameters or ab-initio simulations.

After the complete potential energy is given, the MD algorithms proceed to solve the equations of motion, using a numerical integration algorithm. The LAMMPS package [140], which is the code that will be used in the analysis what will be presented in the next chapters, use the Velocity-Verlet integration method [141]. This algorithm has great advantages for MD simulation: it is time reversible, it is symplectic, it allows the usage of long timesteps and it has low computational cost. Of course, the timestep of the simulation must be chose accordingly to the properties under analysis.

Then, once the simulation setup is ready, a simulation cell must be provided. Firstly, if not explicitly wanted, surface effects need to be addressed by utilizing Periodic Boundary Conditions (PBC). Even in a large simulation cell, a great percentage of atoms would be on the outer faces of the simulation cell, and these will have a large effect on all the calculated properties. Using the PBC aims to prevent this by surrounding the simulations cell with image of itself and making the surface atoms interact with the atoms from the nearest images. This methodology is called the minimum image convection and is a good approximation in most cases. Finally, an ensemble must be chosen. Worth mentioning are: the canonical one (also referred as the NVT ensemble), in which the number of particles (N), the volume of the simulation cell (V) and the Temperature (T) are considered constants and do not change during the simulation; the microcanonical ensemble (NVE) in which the number of particles (N), the volume of the simulation cell (V) and the energy of the system (E) are considered constants.

In summary, molecular dynamics is one of the classical main simulation methodology that solves the Newtonian equation of motion for a large number of simulated atoms or molecules. It is a method with low computational cost and, when used alongside a good representation of the parameter of the system, it can give accurate estimation of a large array of macroscopic properties.

2.5 Frozen phonon

The frozen phonon methodology(often referred as finite displacements method is a simulation technique that allow us to calculate the thermal properties of a crystalline structure using the phonon formalism that is explained above. This technique needs large simulation cells, often referred as *supercells*, in order to give results that are good approximation of experimental data. Generally, a supercell is composed by a number of repetitions of the unit cell of the crystal, so it is common practice to define the simulation cell as a $n \times m \times o$ supercell, where n is the number of replicas in the x direction, m is the number of replicas in the y direction and o is the number of replicas in the z direction.

2.5.1 Interatomic force constants

In order to develop the formalism needed to understand this methodology, we must start from the Taylor expanded potential in Equation 2.1, as we can use this method to calculate the force constants $U_{i_1,i_2,...,i_n}(l_1b_1, l_2b_2, ..., l_nb_n)$.
Using the properties of translational and/or rotational invariance, we can identify a set of N irreducible force constants $\{U_i\}$ and their column vector $\mathbf{\Phi}$. Using this

formalism, Equation 2.1 become:

$$U_{TEP} = \boldsymbol{b}^T \boldsymbol{\Phi}, \tag{2.53}$$

where for clarity we have change the notation of the potential energy into U_{TEP} (Taylor Expanded Potential). $\boldsymbol{b}$ is a row vector defined as $\boldsymbol{b} = \partial U / \partial \Phi$.
By deriving the potential energy U_{TEP} we can of course obtain the atomic force:

$$\boldsymbol{F}_{TEP}(\boldsymbol{u}) = -\frac{\partial U_{TEP}}{\partial \boldsymbol{u}} = -\frac{\partial \boldsymbol{b}^T}{\partial \boldsymbol{u}} \boldsymbol{\Phi} = \boldsymbol{A}(\boldsymbol{u}) \boldsymbol{\Phi}. \tag{2.54}$$

In this equation we have introduced the matrix $\boldsymbol{A}(\boldsymbol{u}) \in \mathbb{R}^{3N_S \times N}$ where N_S is the number of atoms in the supercell and the matrix u, with $u^T = (u_1^x, u_1^y, u_1^z, u_2^x, u_2^y, u_2^z, ..., u_{N_S}^x, u_{N_S}^y, u_{N_S}^z,)$, that is the matrix composed by the $3N_S$ atomic displacements. Notice how both $\boldsymbol{A}$ and $\boldsymbol{F}_{TEP}$ explicitly depend on the displacements matrix.

The problem now is to obtain a suitable description for $\boldsymbol{\Phi}$. At first, it is convenient to use a *brute force* method in form of a linear regression. We generate N_d displacement patterns and, with a sufficiently large N_d, we obtain a system of N_d equations each in the form of Equation 2.54 from which we can obtain the full $\boldsymbol{\Phi}$ vector. We can call $\boldsymbol{u}_n$ the nth displacement vector ($1 \leqslant n \leqslant N_d$), $\mathbb{F}_{TEP}^T = [\boldsymbol{F}_{TEP}^T(\boldsymbol{u_1}), \boldsymbol{F}_{TEP}^T(\boldsymbol{u_2}), ..., \boldsymbol{F}_{TEP}^T(\boldsymbol{u_{N_d}})]$ and $\mathbb{A}^T = [\boldsymbol{A}^T(\boldsymbol{u_1}), \boldsymbol{A}^T(\boldsymbol{u_2}), ..., \boldsymbol{A}^T(\boldsymbol{u_{N_d}})]$ the matrices composed by the forces and $\boldsymbol{A}$ for every displacement pattern. Using this formalism, we can write a generalized expression that combine all the N_d equations for every pattern:

$$\mathbb{F}_{TEP} = \mathbb{A} \boldsymbol{\Phi} \tag{2.55}$$

This method, while giving a good base, must be further refine in order to give results usable in a scientific research. To do so, we need to adopt some statistical methods and then confront those with the linear regression results. In a way, we can see this process as: we use the linear regression force constants as a validation

for the ones calculated with more refined statistic methods.

There are primarily three type of statistic methods that we can adopt: ordinary least square, elastic-net regression and adaptive LASSO. In the work presented in this thesis, only the first methodology is used.

In the ordinary least square methodology, we obtain an estimation of the force constant matrix $\mathbf{\Phi}_{OLS}$ by the minimization of the residual sum of squares between the forces obtained with the linear regression method and the ones obtained through simulations:

$$\mathbf{\Phi}_{OLS} = \underset{\Phi}{\operatorname{argmin}} \left(\frac{1}{2N_d} ||\mathbb{F}_{SIM} - \mathbb{F}_{TEP}||_2^2 \right) = \underset{\Phi}{\operatorname{argmin}} \left(\frac{1}{2N_d} ||\mathbb{F}_{SIM} - \mathbb{A}\mathbf{\Phi}||_2^2 \right). \tag{2.56}$$

From this we can obtain the fitting error by:

$$\sigma = \sqrt{\frac{||\mathbb{F}_{SIM} - \mathbb{A}\mathbf{\Phi}||_2^2}{||\mathbb{F}_{SIM}||_2^2}} \tag{2.57}$$

Notice that in order to solve Equation 2.56 obtaining all elements of $\mathbf{\Phi}_{OLS}$ uniquely, we need $\mathbb{A}^T\mathbb{A}$ to be full rank.

$\mathbb{F}_{SIM}$ can be obtained through every type of numerical simulation, e.g. DFT or MD simulations.

2.5.2 Phonon properties

Using the force constant obtained above, we can now calculate the dynamical matrix of the crystal using Equation 2.20.

From the dynamical matrix we can then obtain the thermal properties of interest, depending on the level of approximation (harmonic, 3rd order anharmonic, etc...).

The phonon frequency can be derived using:

$$\omega_s(\boldsymbol{q}) = [\boldsymbol{e}_s^*(\boldsymbol{q})]^T D(\boldsymbol{q}) \boldsymbol{e}_s(\boldsymbol{q}), \tag{2.58}$$

where $\boldsymbol{e}_s(\boldsymbol{q})$ is the atomic polarization vector.

From the phonon frequency we can easily derive the phonon group velocity for the ith direction:

$$\boldsymbol{v}_{gi}(s\boldsymbol{q}) = \frac{\partial \omega_s(\boldsymbol{q})}{\partial \boldsymbol{q}} \sim \frac{\omega_s(\boldsymbol{q} + \Delta_{s\boldsymbol{q}}) - \omega_s(\boldsymbol{q} - \Delta_{s\boldsymbol{q}})}{2\Delta_{\boldsymbol{q}}} \tag{2.59}$$

The second term is the exact equation to obtain the group velocity, the third is the relation that is actually used for the numerical calculations.

In order to calculate the phonon DOS, we have to make some adjustments to the Equation 2.27. Namely, we have to find some way to computationally resolve the integral, thus the basic idea is to convert $\int \rightarrow \sum$. After some calculations, we obtain:

$$G(\omega) = \frac{1}{N_q} \sum_{\boldsymbol{q},s} \delta(\omega - \omega_s(\boldsymbol{q})) \tag{2.60}$$

Since we want to apply the thermal conductivity using the SM-RTA-BTE theory, we need to apply Equation 2.36. We have already discussed how to obtain all parameters except for $\tau_{s\boldsymbol{q}}$. As we have already discussed, in order to obtain the phonon lifetime we have to introduce anharmonic terms in our discussion.

As stated in Equation 2.41, there are many quantities that contribute to the total phonon lifetime and in this discussion we will focus only on two: the one connected to the cubic self-energy and the one derive from isotope scattering. Having this in mind, we can rewrite Equation 2.41 as:

$$\frac{1}{\tau}(T) = 2(\Gamma_{qs}^{anh}(T) + \Gamma_{qs}^{iso}), \tag{2.61}$$

where $\Gamma_{qs}^{anh}(T)$ is the phonon line-width associated with the anharmonic self-energy and Γ_{qs}^{iso} is the one associated with the isotope scattering.

Let us discuss the self-energy term first.

We can obtain the phonon line-with $\Gamma_{qs}^{anh}(T)$ as the imaginary part of the phonon

self-energy, which value is given by the following expression:

$$\Sigma_{qs}(i\omega_m) = \frac{1}{2\hbar^2}\sum_{q_1 s_1}\sum_{q_2 s_2}\left|V^{(3)}_{-qs,\,q_1 s_1,\,q_2 s_2}\right|^2 \times\left[\frac{n_1+n_2+1}{i\omega_m+\omega_1+\omega_2}-\frac{n_1+n_2+1}{i\omega_m-\omega_1-\omega_2}+\frac{n_1-n_2}{i\omega_m-\omega_1+\omega_2}-\frac{n_1-n_2}{i\omega_m+\omega_1-\omega_2}\right], \tag{2.62}$$

where $V^{(3)}_{-qs,q_1 s_1,q_2 s_2}$ is the matrix element of the operator $\hat{V}_3$ that we discussed in Equation 2.39. We can define this matrix element as:

$$V^{(3)}_{qs,\,q's',\,q''s''} = \left(\frac{\hbar}{2N_q}\right)^{\frac{3}{2}}\frac{1}{\sqrt{\omega_{qs}\,\omega_{q's'}\,\omega_{q''s''}}}\sum_{\ell,\ell',\ell''}\exp\left[i(q\cdot r(\ell)+q'\cdot r(\ell')+q''\cdot r(\ell''))\right] \sum_{b,b',b''}\frac{1}{\sqrt{M_b M_{b'} M_{b''}}}\sum_{\mu,\nu,\lambda}\Phi_{\mu\nu\lambda}(b\ell;\,b'\ell';\,b''\ell'')\,e_\mu(b;qs)\,e_\nu(b';q's')\,e_\lambda(b'';q''s''), \tag{2.63}$$

Combining these two equation, we can finally define the phonon line-width using the analytic continuation to the real axis ($i\omega_m \to \omega + i0^+$):

$$\Gamma^{anh}_{qj}(\omega) = \frac{\pi}{2\hbar^2}\sum_{q_1 s_1}\sum_{q_2 s_2}\left|V^{(3)}_{-qs,\,q_1 s_1,\,q_2 s_2}\right|^2 \times\Big[-(n_1+n_2+1)\,\delta(\omega+\omega_1+\omega_2)+(n_1+n_2+1)\,\delta(\omega-\omega_1-\omega_2) -(n_1-n_2)\,\delta(\omega-\omega_1+\omega_2)+(n_1-n_2)\,\delta(\omega+\omega_1-\omega_2)\Big]. \tag{2.64}$$

For the isotope scattering we will use the description given in [142], that allow us to write the isotope linewidth as:

$$\Gamma^{iso}_{qs}(\omega) = \frac{\pi}{4N_q}\,\omega^2_{qs}\sum_{q_1 s_1}\delta(\omega-\omega_{q_1 s_1})\sum_b g_2(b)\left|\mathbf{e}^*(b;q_1 s_1)\cdot\mathbf{e}(b;qs)\right|^2, \tag{2.65}$$

where $g_2(b)$ is a dimensionless factor given by:

$$g_2(b) = \sum_i f_i(b)\left(1-\frac{m_i(b)}{M_b}\right)^2, \tag{2.66}$$

where $f_i(b)$ is the fraction of the ith isotope pf an element having mass m_i and $M_k = \sum_i f_i m_i(b)$. Typically, the calculation of both line-width is the most computational heavy process of the calculation of thermal conductivity.

After obtaining the phonon lifetimes, we can proceed in using Equation 2.36 to calculate the thermal conductivity.

An important remark about thermal conductivity is that it depends on both temperature and direction, thus the result of this calculation will be a thermal conductivity tensor. We can rewrite Equation 2.36 in order to empathize this property as:

$$\kappa^{\mu\nu}(T) = \frac{1}{VN_q}\sum_{\boldsymbol{q},s} c_{\boldsymbol{q}s}(T) v^{\mu}_{\boldsymbol{q}s} v^{\nu}_{\boldsymbol{q}s} \tau_{\boldsymbol{q}s}(T), \tag{2.67}$$

where we used the specific heat expression $c_{\boldsymbol{q}s}(T) = \hbar\omega(\boldsymbol{q}s)\partial n_{BE}(s\boldsymbol{q}, T)/\partial T$.

We can define another interesting property from this definition of thermal conductivity:

$$\kappa^{\mu\nu}_{sp}(\omega) = \frac{1}{VN_q}\sum_{\boldsymbol{q},s} c_{\boldsymbol{q}s}(T) v^{\mu}_{\boldsymbol{q}s} v^{\nu}_{\boldsymbol{q}s} \tau_{\boldsymbol{q}s}(T) \delta(\omega - \omega(\boldsymbol{q})), \tag{2.68}$$

called thermal conductivity spectrum. This value tall us how much every phonon with the given frequency ω contribute to the total thermal conductivity. Of course we have that:

$$\kappa^{\mu\nu} = \int_0^{\infty} \kappa^{\mu\nu}_{sp}(\omega) d\omega. \tag{2.69}$$

The methodology presented this far refers to an $3rd$ order anharmonicity, but in theory can be extendable to any order. [143] showed the use of finite displacement in some calculation with $4th$ order anharmonicity obtaining results in great accord to experimental data, were calculation with the $3rd$ order where shown to fail. Of course, the increase anharmonicity order leads to an increase in computational cost.

This type of theory will be adopted in the studies presented in this thesis using the package `ALAMODE` [144].

2.6 Approach to Equilibrium Molecular Dynamics

In the previous section of this chapter we mainly discussed thermal properties in function of the phonon description and the Boltzmann Transport Equation. However, that formalism relies heavily on the crystallity of the system, failing with more complex material like doped or defected systems. Henceforth we will now discuss an alternative method to calculate thermal conductivity based on the approach to equilibrium molecular dynamics (AEMD) [145].

In order to develop this methodology, let us begin from the general heat equation

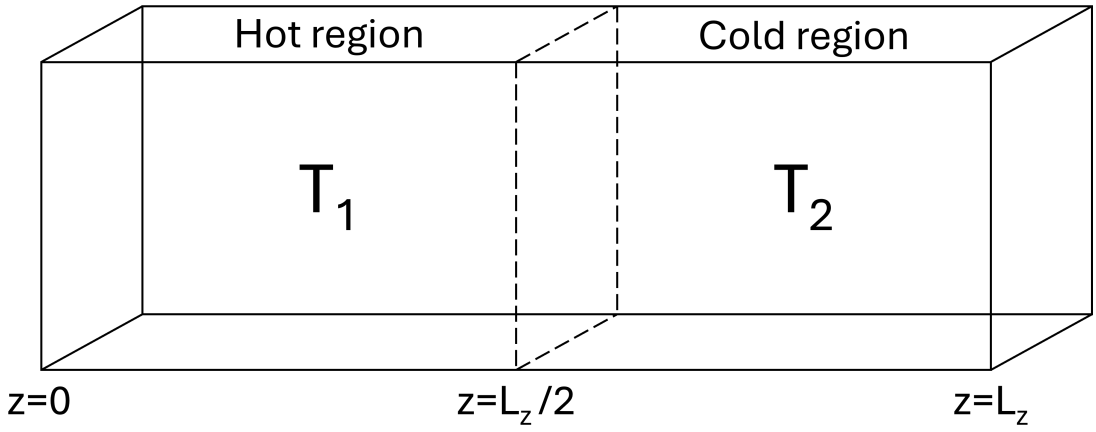

Figure 2.8: *Representation of a generic simulation cell used in AEMD simulations, with periodic boundary condition. The two region are initially set in order to have* $T_1(0) > T_2(0)$ *[145].*

that describe thermal transport along the z axis of a system defined in an interval with $0 \leq z \leq L_z$ (see Figure 2.8):

$$\frac{\partial T}{\partial t} = \bar{\kappa} \frac{\partial^2 T}{\partial z^2} \tag{2.70}$$

where $\bar{\kappa}$ is the thermal diffusivity. If we have a system characterized by density ρ and heat capacity c_v, we can define the thermal conductivity as:

$$\kappa = \bar{\kappa} \rho c_v = \frac{\bar{\kappa} C_v}{V}. \tag{2.71}$$

If the system is at a temperature above its Debye temperature Θ_D, the specific heat can be easily obtained as

$$C_v = 3Nk_B, \tag{2.72}$$

while for $T < \Theta_D$ quantum correction are necessary.
In order to solve Equation 2.70, we can use the method of separation of variables by introducing a function that only depends on the temperature and one that only depends on the direction z:

$$T(z,t) = H(z)T(t) \tag{2.73}$$

We now have to find a suitable expression for both functions. $H(z)$ can be easly found by setting the boundaries condition of the problem. Since we want to use this methodology along with MD simulations, it is convenient to use a step-like temperature profile with periodic boundary conditions (i.e. $T(0,t) = T(L_z,t)$). This situation is showed in Figure 2.8 and is represented by the system:

$$H(z) = \begin{cases} T_1 \text{ for } 0 < z < L_z/2 \\ T_2 \text{ for } L_z/2 < z < L_z \end{cases} \tag{2.74}$$

The most general solution for Equation 2.73 can be written as:

$$T(z,t) = \sum_{n=1}^{\infty} \left[A_n \cos(\alpha_n z) + B_n \sin(\alpha_n z)\right] e^{-\alpha_n^2 \bar{\kappa} t} \tag{2.75}$$

where $\alpha = 2\pi n/L_z$,

$$A_n = \frac{1}{L_z} \int_0^{L_z} \cos(\alpha_n z) H(z)\, dz \tag{2.76}$$

and

$$B_n = \frac{1}{L_z} \int_0^{L_z} \sin(\alpha_n z) H(z)\, dz \tag{2.77}$$

are two parameters connected with the $H(z)$ function. Using Equation 2.74, we can write an explicit expression for these tow parameters:

$$A_n = \begin{cases} \frac{1}{L_z}\int_0^{L_z} H(z)\,dz = \frac{T_1+T_2}{2} (n=0) \\ \frac{1}{L_z}\int_0^{L_z} \cos(\alpha_n z) H(z)\,dz = 0 \quad (n \neq 0) \end{cases} \tag{2.78}$$

and

$$\begin{aligned} B_n &= \frac{1}{L_z}\int_0^{L_z} \sin(\alpha_n z) H(z)\,dz \\ &= \frac{T_1 - T_2}{\alpha_n L_z}\left[\cos(\alpha_n L_z) - 1\right]. \end{aligned} \tag{2.79}$$

Using these expression, we can write the general solution for Equation 2.70 as:

$$T(z,t) = A_0 + \sum_{n=1}^{\infty} B_n \sin(\alpha_n z) e^{-\alpha_n^2 \bar{\kappa} t}. \tag{2.80}$$

Equation 2.74 refers to the situation at $t = 0$, then we can use a microcanonical MD simulation to let the system evolve for $t > 0$. We can see how the initial step-like configuration is progressively smoothed. A visual representation of this phenomenon is provided in Figure 2.9. It is useful to define the average temperature of the two region of the system as:

$$\langle T_1 \rangle = \frac{1}{L_z}\int_0^{L_z/2} T(z,t)\,dz, \tag{2.81}$$

$$\langle T_2 \rangle = \frac{1}{L_z}\int_{L_z/2}^{L_z} T(z,t)\,dz. \tag{2.82}$$

This allow us to find an analytic expression for the difference in temperature of the two regions $\Delta T(t) = \langle T_1 \rangle - \langle T_2 \rangle$. Since the system will go to thermal equilibrium after a large enough amount of time, $\Delta T(t) \to 0$. If we combine this information with the discussion above, we obtain:

$$\Delta T(t) = \langle T_1 \rangle - \langle T_2 \rangle = \sum_{n=1}^{\infty} C_n e^{-\alpha_n^2 \bar{\kappa} t} \tag{2.83}$$

where

$$C_n = 8(T_1 - T_2)\frac{\left[\cos\left(\frac{\alpha_n L_z}{2}\right) - 1\right]^2}{\alpha_n^2 L_z^2}. \tag{2.84}$$

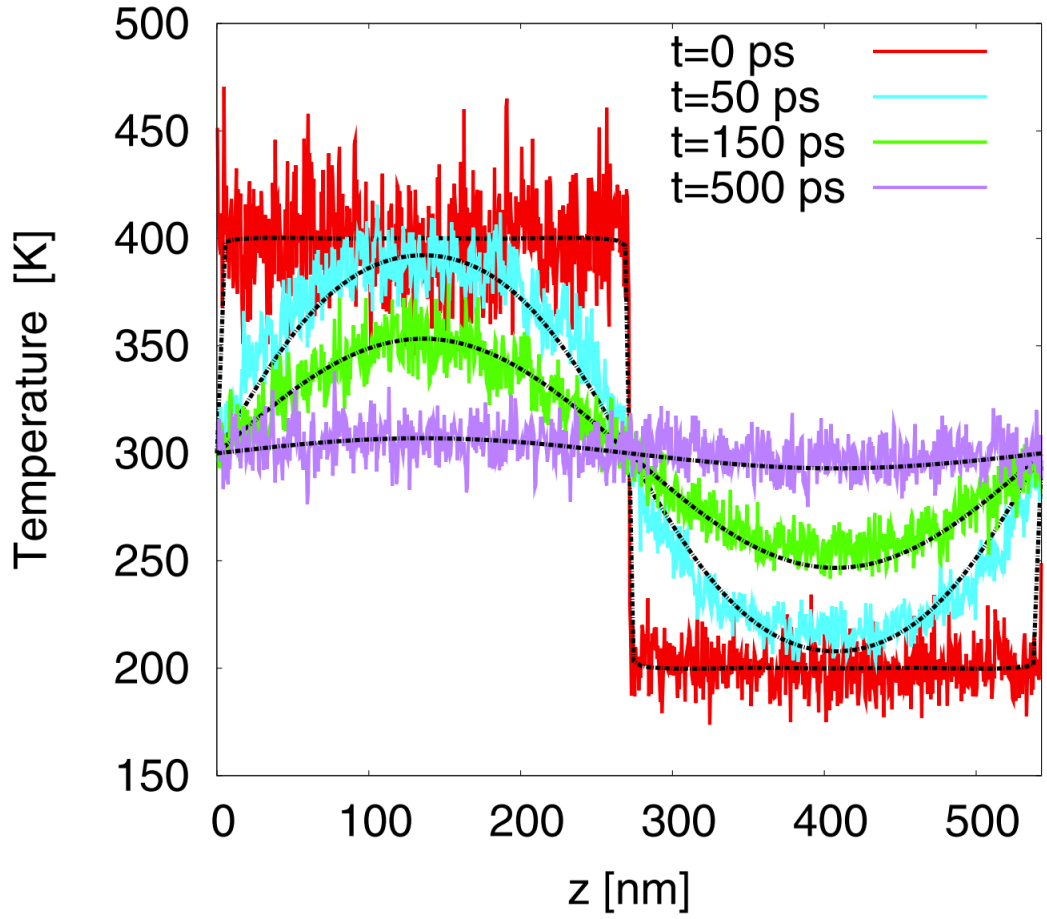

Figure 2.9: *Time profile in function of time in a c-Si sampl. The black lines represent the analytical solution of Equation 2.70, while the colored lines are obtained trough AEMD simulations[145].*

Equation 2.83 is the equation that will allow us to obtain the thermal conductivity. In fact, the simulation protocol using this method is quite simple:

1. we prepare our simulation cell similarly to Figure 2.8, with an initial temperature profile determined by Equation 2.74,

2. through a microcanonical MD simulation the system is evolve for enough time to reach thermal equilibrium and the values of $\Delta T(t)$ is generated,

3. by fitting the values of $\Delta T(t)$ obtained above with Equation 2.83 we obtain

the thermal diffusivity

Then, we can simply use Equation 2.71 to obtain the thermal conductivity. Unfortunately, there are some nuisance when this method is used in the calculation of κ. [145] report a in depth analysis on these problems and here we will just focus on the results.

While not apparent from Equation 2.83, if we repeat the MD simulations for systems composed by the same material and length L_z we can see a dependence on the cross-section $S = L_x \times L_y$ of the thermal conductivity. This is probably due to the difference in the number atoms: fewer atoms means worse statistics in the calculation of Equation 2.81 and Equation 2.82. This hypothesis is also supported by the observed large number of oscillation in $\Delta T(t)$ in the samples with less atoms. However, it is shown that after a large enough S is provided, this dependence dims until the value of κ converges. Therefore, it is of the utmost importance to check the convergence of the cross-section before starting any investigation using AEMD. More apparent is the dependence of κ from the sample length L_z. As discussed in [146], we can rewrite Equation 2.83 in a way that explicitly states this dependence:

$$\kappa(L_z) = \frac{1}{N_q V} \sum_{q,s} c_{q,s} v_{q,s}^2 \tau_{\infty,q,s} \left[1 + \frac{2|v_{q,s}|\tau^{\infty,q,s}}{L_z} \right]^{-1} . \tag{2.85}$$

From this we can observe that $1/\kappa = f(1/L_z)$ and is thus possible to define a function $1/k_\infty$ where L_z is large enough to be representative of a macroscopic sample. In these conditions, we can use the Taylor expansion to study the function $1/k_\infty$:

$$\frac{1}{\kappa_\infty} = f(0) - \frac{f'(0)}{L_z} + \frac{f''(0)}{2L_z^2} + \dots \tag{2.86}$$

Since $L_z \to \infty$, and so $1/L_z \to 0$, we can truncate the expansion at the first term. In this way, we can expect that by plotting $1/\kappa$ versus $1/L_z$ we will find a linear trend, from which we can obtain the true thermal conductivity κ_∞ by a fitting procedure. In order to apply this method, we have to chose L_z values accordingly, and

thus we have to understand the physical meaning behind the dependence of κ on L_z. In general, every phonon have a mean free path λ related to its lifetime shown in Equation 2.41 simply by $\lambda = \tau_s \boldsymbol{q} \times v_{g,i}$. If we take a $L_z < \lambda$ we are effectively excluding from our calculation every phonon with $\lambda > L_z$, underestimating κ in the process. Therefore, in order to apply the fitting procedure discussed above, we must have multiple simulation sample each with increasing L_z, with $\min(L_z) \geq \lambda$. In summary, while the use of AEMD does not give any information about phonon behavior, it bypasses all the approximations used to obtain the SM-RTA-BTE, allowing the estimation of thermal conductivity at any order of anharmonicity, particularly useful in crystal with strong anharmonicity or for non crystalline materials, e.g. doped system or defected one.

2.7 Thermal transport in the Wigner formalism

As stated above, the phonon formalism give us an understanding of the microscopical behavior of the solid. However, The Boltzmann Transport Equation described above fails to predict the properties of non-crystalline solids. Historically, two fundamentally different pictures have coexisted:

- In **crystalline solids**, heat is carried by well-defined phonon quasiparticles. These phonons propagate with a group velocity $\mathbf{v}_{qs}$ and scatter via anharmonic interactions or impurities. Their dynamics is successfully captured by the Boltzmann transport equation (BTE)[132].

- In **amorphous solids and glasses**, phonons cannot be described as long-lived wave packets. Instead, heat diffuses through wave-like tunneling processes between quasi-degenerate vibrational eigenstates, as described by Allen and Feldman [147].

For decades, these two regimes were treated as fundamentally distinct. However, many materials of technological interest, including complex crystals, thermoelectrics, and halide perovskites, do not fit neatly into either category. Their thermal conductivity is too low to be explained by the BTE, yet their crystalline order prevents a description solely in terms of the Allen-Feldman model. This long-standing gap motivated the development of a more general framework: the **Wigner transport equation (WTE)** [148].

In order to develop this unified theory, we have to rewrite Equation 2.33 in a way that explicitly incorporates anharmonicity:

$$\frac{\partial n_{qs}}{\partial t} + \mathbf{v}_{qs} \cdot \nabla_{\mathbf{r}} n_{qs} = \left.\frac{\partial n_{qs}}{\partial t}\right|_{\text{scatt.}}, \tag{2.87}$$

where n_{qs} is the non-equilibrium population of a phonon with wavevector q and branch index s, $\mathbf{v}_{qs} = \nabla_q \omega_{qs}$ is its group velocity, and the right-hand side describes scattering processes. According to this new notation, the thermal conductivity derived from this equation can be written as

$$\kappa_{\alpha\beta}^{\text{BTE}} = \frac{1}{NV} \sum_{qs} C_{qs} v_{qs}^{\alpha} v_{qs}^{\beta} \tau_{qs}, \tag{2.88}$$

with C_{qs} the mode heat capacity and τ_{qs} the phonon lifetime.

This formulation is extremely successful for *simple crystals*, where phonon interband spacings are much larger than line-widths. However, when line-widths become comparable to or larger than interband separations, the quasiparticle picture breaks down. In such cases the BTE overestimates κ by orders of magnitude [148, 149].

The idea behind the Wigner formalism is to overcome this limitation by starting from the quantum Liouville equation for the density operator $\hat{\rho}$ and applying the Weyl quantization procedure [150]. The central object becomes the **Wigner distribution**, which naturally includes both phonon populations ($s = s'$) and off-diagonal **coherences** ($s \neq s'$). The resulting Wigner transport equation (WTE)

reads:

$$\frac{\partial}{\partial t}n_{ss'}(q,t) + i\big(\omega_{qs} - \omega_{qs'}\big)n_{ss'}(q,t) + \frac{1}{2}\Big\{\mathbf{v}(q), \nabla_{\mathbf{r}} n(q,t)\Big\}_{ss'} = \frac{\partial}{\partial t}n_{ss'}(q,t)\Big|_{\text{scatt.}}. \tag{2.89}$$

Here:

- The **diagonal terms** ($s = s'$) reduce to the BTE description of phonon populations.
- The **off-diagonal terms** ($s \neq s'$) describe wave-like tunneling between bands, a mechanism absent from the BTE.

2.7.1 Energy density and heat flux

The Wigner approach allows us to define a well-posed local vibrational energy density:

$$U(\mathbf{R},t) = \frac{1}{(2\pi)^3}\sum_{ss'}\int_{\text{BZ}} d^3q\, \hbar\omega_{qs}\, n_{ss'}(\mathbf{R},q,t)\, \delta_{ss'}, \tag{2.90}$$

and the associated harmonic heat flux:

$$\mathbf{J}(\mathbf{R},t) = \frac{\hbar}{(2\pi)^3}\sum_{ss'}\int_{\text{BZ}} d^3q\, \frac{\omega_{qs}+\omega_{qs'}}{2}\, \mathbf{v}_{ss'}(q)\, n_{ss'}(\mathbf{R},q,t). \tag{2.91}$$

The crucial insight is that the heat flux is not carried exclusively by particle-like phonons, but also by coherent superpositions of phonon states. This reconciles the particle-like and wave-like views of thermal transport.

2.7.2 Thermal conductivity in the Wigner framework

Solving the WTE in steady state yields the general expression for the conductivity [151]:

$$\kappa_{\alpha\beta} = \kappa^P_{\alpha\beta} + \frac{1}{(2\pi)^3}\int_{\mathrm{BZ}} d^3q \sum_{s\neq s'} \frac{\omega_{qs}+\omega_{qs'}}{4}\left(\frac{C_{qs}}{\omega_{qs}}+\frac{C_{qs'}}{\omega_{qs'}}\right) \times \frac{v^\alpha_{ss'}(q)\, v^\beta_{s's}(q)}{(\omega_{qs}-\omega_{qs'})^2 + \left[\frac{\Gamma_{qs}+\Gamma_{qs'}}{2}\right]^2}, \quad (2.92)$$

where Γ_{qs} are phonon line-widths. The first term κ^P corresponds to the particle-like Boltzmann contribution, while the second term represents the additional wave-like tunneling channel.

Furthermore, the Wigner formalism introduces a natural timescale, foten referred as the **Wigner time limit**:

$$\tau_\omega = \frac{1}{\Delta\omega}, \quad (2.93)$$

where $\Delta\omega$ is the average phonon interband spacing.

Therefore, we can identify two different regimes, depending on the relation between τ and τ_ω. In details, we have that:

- if $\tau \gg \tau_\omega$, phonons behave as well-defined quasiparticles and transport is Boltzmann-like.
- if $\tau \lesssim \tau_\omega$, coherences dominate and wave-like conduction emerges.

This condition is directly connected to the well-known **Ioffe-Regel limit**, where the phonon mean free path approaches the interatomic distance [148].

Thanks to this mixing of particle-like and wave-like descriptions, the predictive power of the WTE has been demonstrated in several classes of materials for which the normal BTE as been proved to fail:

- In **thermoelectric skutterudites**, filler atoms ("rattlers") such as Yb reduce phonon lifetimes down to the Wigner limit, leading to a crossover from

Boltzmann to Wigner transport. At operating temperatures, particle-like and wave-like contributions become comparable, explaining the exceptionally low conductivity and high thermoelectric performance [151].

- In **complex oxides and halide perovskites**, the WTE captures ultralow thermal conductivity that the BTE fails to describe [148].

- In **glasses**, the WTE reduces analytically to the Allen–Feldman theory, validating its generality.

To summarize, the Wigner transport equation provides a unified quantum framework for lattice thermal transport. It manage to unify the particle-like Boltzmann and the wave-like Allen-Feldman descriptions, explains the microscopic origin of ultralow thermal conductivity and introduces new physically motivated microscopic descriptors such as the Wigner time limit. Beyond its conceptual importance, it offers practical tools for materials discovery, enabling rational design of thermoelectric and thermal-barrier materials where both particle-like and wave-like phonon transport mechanisms are crucial. On the downside, it increases the already long computational cost of microscopical thermal conductivity calculations, such as the finite displacement method described above, since we have to separately calculate the BTE term and the additional contribution in Equation 2.92.

2.8 Mode decomposition technique

Both BTE and Wigner based approaches shows their limitations when the crystal under study shows strong anharmonicity. In some cases, even fourth order anharmonicity may not be enough to adequately characterize the system, leading to false prediction on properties like thermal expansion, Raman and infrared spectra, phonon lifetimes and thermal conductivity. For this reason, a new approach to

calculate the anharmonic force constants is needed.
A novel method that helps resolving this issue is the normal mode decomposition technique [152]. This method is based on molecular dynamics and allow us to extract anharmonic properties from the atomic trajectories, thus accounting for anharmonicity to all orders. Unfortunately, this technique have two large limitations:

- high computational cost due to long molecular dynamics simulations with large simulation cells required to achieve convergence;
- need of very accurate force fields that account for high anharmonic behavior.

Although, since the computational cost is inferior to the one of a fourth order DFT based methodology, thereby in systems that exhibit strong anharmonic behavior this technique is very helpful.
In details, the normal mode decomposition technique enables the extraction of both temperature-dependent vibrational frequencies and phonon lifetimes by calculating the power spectrum of atomic velocities projected onto phonon eigenvectors:

$$G_{qs}(\omega) = 2\int_{-\infty}^{\infty} \langle v_{qs} * (0) | v_{qs}(t) \rangle e^{i\omega t}\, dt \approx \frac{\left\langle |v_{qs}(t)|^2 \right\rangle}{\frac{1}{2}\Gamma_{qs}\pi \left(1 + \left(\frac{\omega - \widetilde{\omega}_{qs}}{\frac{1}{2}\Gamma_{qs}}\right)^2\right)} \tag{2.94}$$

where $\widetilde{\omega}_{qs}$ is the temperature-dependent phonon frequency.
This power spectrum is then fitted to a Lorentzian function. By calculating its peak position it is possible to estimate the $\widetilde{\omega}_{qs}$ and by its full width at half maximum it is possible to obtain the line-width Γ_{qs}.
The combination of this power spectrum and their Lorentzian fit can be considered as spectral energy density that yields important information. If a purely harmonic system is considered, the resulting Lorentzian spectrum would be composed only by distinct and defined peaks, while in systems with strong anharmonicity, where

phonon mixing is present, the peaks would appear as blurred and overlapping. The spectral energy density can therefore serve as a practical tool for analyzing phonon mixing.

Furthermore, this methodology can be used as an alternative way to obtain the factors for calculating thermal conductivity, both in the BTE approximation and with the Wigner approach.

The code that was used for the analysis that employed the mode decomposition technique is the DynaPhoPy code, that allow the estimation of phonon line-widths and frequency shifts from molecular dynamics trajectories after their projection onto a series of harmonic phonon modes obtained by Phonopy [153, 154]. The power spectrum is then calculated by means of Fourier transform and Lorentzian functions are employed for the calculation of the peaks, in order to extract the anharmonic properties [155].

Unfortunately, the spectral energy density obtained via Equation 2.94 gives only qualitative indication of phonon mixing, thus must be refined in order to obtain a quantitative measure of it.

A possibility is to use the cross correlation as a tool to study quantitatively phonon mixing. This approach consists in calculating the power spectrum of the cross-correlation of atomic velocities projected onto two different phonon modes:

$$G_{q_i q_j s}(\omega) = 2 \int_{-\infty}^{\infty} \langle v_{q_i s} * (0) | v_{q_j s}(t) \rangle e^{i\omega t} \, dt \tag{2.95}$$

where q_i and q_j are two wave-vectors. By calculating the $G_{q_i q_j s}(\omega)$ for every q_i and q_j it is possible to create the correlation matrix $G(\omega)$ where the diagonal terms will be called auto-correlation terms (for $i = j$, $G_{q_i q_i s}(\omega)$) and the off-diagonal terms will be called cross-correlation terms (for $i \neq j$, $G_{q_i q_j s}(\omega)$). The cross-correlation terms are correspondent to the overlapping of peaks found in Equation 2.94 and thus can provide a quantitative measurement of phonon mixing.

In summary, an purely harmonic crystal will be characterized by $G_{q_i q_j s}(\omega) = 0$ for

$i \neq j$, while the stronger the anharmonicity, the higher this value will be.

Chapter 3

Thermal transport of pristine and functionalized TaS_2

TaS_2 is a material that belong to the class of transition metal dichalcogenoid discussed above. Typically, it is synthesized using the Chemical deposit method [156] in both its 2D mono-layer and 3D bulk configurations. TaS_2 has 4 different stable and metastable stacking types, as shown in Figure 1.5, the stable phase being the 2H-AB and the metastable ones the 1T, 2H-AA' and 3R [48].

In its pristine bulk state, it shows an high electrical conductivity and Seebeck coefficient, but it also have a really high in-plane thermal conductivity. Combining this, the figure of merit calculated using Equation 1.6 is unfortunately very low. In fact, at room temperature, the TaS_2 2H $\sigma \sim 3000$S cm^{-1}, $S \sim -7.6$ V K^{-1} and $\kappa \sim 36$ W m^{-1}K^{-1} for a total figure of merit $zT_{300K} \sim 5 \times 10^{-5}$. At higher T, its Seebeck coefficient drastically increase ($S_{440K} \sim -30$ µV K^{-1}) while both electrical and thermal conductivities lightly decrease, leading to an higher figure of merit value of $zT_{440K} \sim 3 \times 10^{-3}$, a value much higher than the one at room temperature but still far from ideal for thermoelectric applications [87].

A solution for making TaS_2 a competitive material in the thermoelectric scenario

was proposed by [87]. In their work, the manage to create a covalent bond between the TaS_2 and an organic molecule, the tert-Butyl isocyanate (C_5H_9NO), obtaining a stable system with interesting properties. In details, the managed to force the covalent bond between a C atom of the tert-Butyl isocyanate and an S atom from the TaS_2, leading to a positioning of the molecule in the inter-layer space. Similar strategies were already employed in other types of material, e.g, some organic crystals [96, 124], and these modification have all shown significant influence on thermal transport properties.

Since the TaS_2 have no dangling bonds, the crystal typically do not react with other substances. Thus, they had to employ a sophisticated strategy to bond the two systems. Firstly, they used an electrochemical reduction to charge the TaS_2 crystal, then they used an electron doping effect to enhance the electron cloud density of S atoms and finally they immerse the system in a solution of tert-Butyl isocyanate at room temperature to form the bonded structure. A visual representation of this technique can be found in Figure 3.1. The results showed in

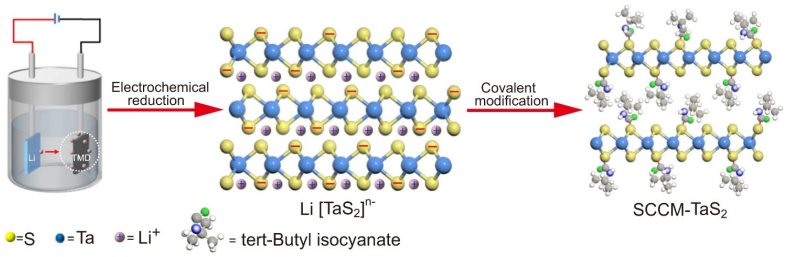

Figure 3.1: *Representation of the synthesis method of the hybrid structure TaS_2 + tert-Butyl isocyanate [87].*

this experimental work are encouraging:

- the electrical conductivity showed an overall increase at all temperatures with a peak at room temperature of double the original value;
- the Seebeck coefficient is practically unchanged;

- the thermal conductivity is reduced by almost two orders of magnitude at all temperatures;

- the figure of merit is largely increase overall, with a peak at 440 K of ~ 0.04.

While this value is still not ideal for thermoelectric applications, the increase in the figure of merit, especially at high temperature, is remarkable. Although the experimental results give ample characterization of the macroscopic properties of the material, they do not give any insight of the microscopic ones, especially in the thermal transport properties.
My work aims to reproduce computationally these results, in particular the ones regarding thermal transport, in order to obtain a theoretical explanation of the reduction in thermal conductivity. Once we understand the mechanism of this change, we would be able to use this mechanism in other systems. To achieve this, a full atomistic investigation was performed [157].

3.1 Computational details

All calculations presented in this chapter rely on the Density Functional Theory (DFT) with periodic boundaries condition. To perform the calculation, the Quantum espresso package was employed [158].
In all calculations I used the corrected generalized gradient approximation of Perdew, Burke and Ernzehof [159], PBEsol [139], with Projector-Augmented Wave (PAW) pseudopotentials [160] and a plane-wave basis set.
In all calculations, a plane-wave kinetic energy cutoff of 60 Ry and a charge-density cutoff of 480 Ry were employed. The convergence thresholds for forces and total energy were set to 10^{-12} Ry$\mathring{A}^{-1}$ and 10^{-15} Ry, respectively. For each of the three

systems considered, the k-point mesh was generated with a reciprocal-space sampling density corresponding to 0.1 $\mathring{A}^{-1}$.

The estimation of thermal properties was performed using the finite displacements method presented in section 2.5, using the code ALAMODE [144]. The anharmonicity was calculated to the $3rd$ order.

To evaluate the harmonic force constants, a supercell containing 96 atom was used for the pristine system and one with 232 atoms was used for the functionalized system, corresponding to a $4 \times 4 \times 2$ replica of the unit cell of both systems. In these calculations, no interatomic interactions cutoff was imposed.

Since the computational cost for the anharmonic calculations is exponentially greater, a smaller number of replicas were employed for the $3rd$ order force constants calculations, i.e. a $2 \times 2 \times 2$ supercell, corresponding to 24 atoms in the pristine system and 58 in the functionalized one. Furthermore, while for the pristine system no interatomic interactions cutoff was imposed, for the functionalized system a cutoff corresponding to the distance between first-neighbor atoms was introduced, to further reduce the computational cost.

To ensure the validity of this method, A size-effect assessment was conducted for the bulk TaS_2 system and no appreciable variations in the calculated properties were found between the $4 \times 4 \times 2$ and $2 \times 2 \times 2$ supercells.

After comparing the results obtained with this methodology to the experiment, this level of theory was deemed sufficient to fully describe the system, without the need to further extend the order of anharmonicity with $4th$ order and beyond or to use the Wigner formalism.

3.2 Systems under study

The introduction of the organic side chain has two important structural effects. The first is an increase of the inter-layer separation, from 6.03 Åto 10.36 Å. The second is the effect of the covalent bond between the sulfur atoms of TaS_2 and the C of the isocyanate group of thert-Butyl isocyanate molecules. In order to investigate the reduction in thermal conductivity, three different systems are taken into account in order to see the effect of both modification interdependently.

The first system is the pristine bulk TaS_2 (Figure 3.2, left). In order to recreate the experimental setup, we chose the 2H-AA' stacking configuration. After a very accurate geometry optimization, the inter-layer distance was found to be 6.02 Å, very similar to the experimental value of 6.03 Å, and the cell angle to be 90°, as was in the experimental setup.

The second system is the pristine TaS_2 with the increased inter-layer distance due to the introduction of the molecule, but without the explicit molecule (Figure 3.2, center). The inter-layer distance used in this elongated system is the one obtained after the accurate optimization of the system with the molecule and not the experimental distance.

The third system is the TaS_2 with the explicit introduction of organic side chains (Figure 3.2, right). As stated above, the procedure to obtain this covalent bond is rather complex and it is out-of-reach of the theoretical methodology adopted in this investigation, furthermore it would be overwhelmingly computational heavy to reproduce using ab-initio techniques. Thus, an alternative method was adopted. At first, the tert-Butyl isocyanate molecules were introduced between the pristine bulk TaS_2 obtained before, with a C-S distance of 3 Å. Then, the oxygen atom in the isocyanate group was fuctionalized by adding an extra hydrogen atom, obtaining a reduction of the double bond C=O. This leaves the C atom with the

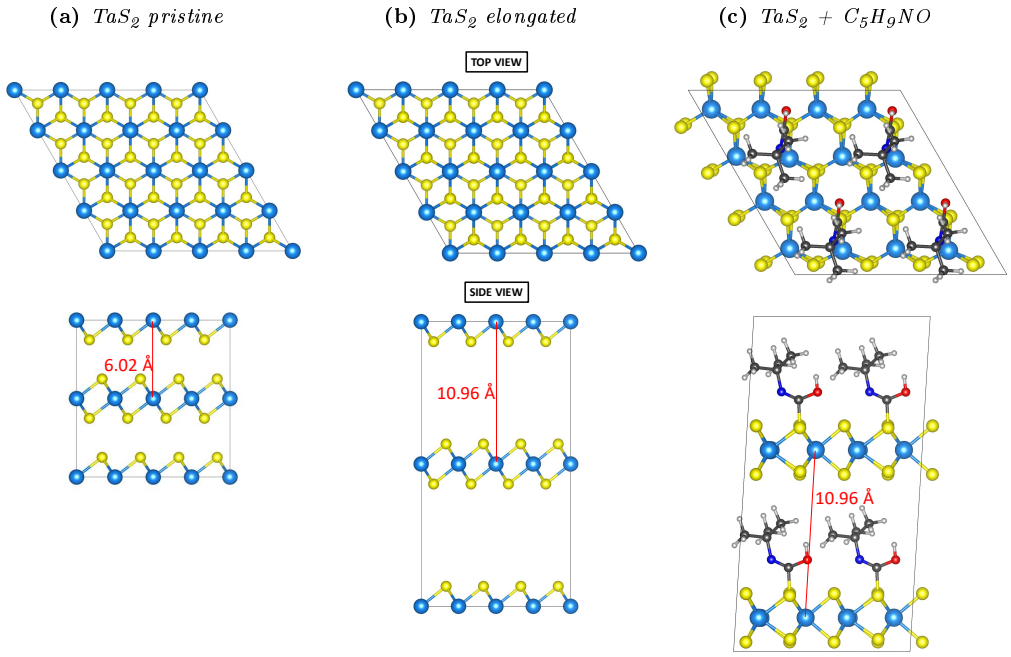

Figure 3.2: *Stick and balls representation of the three geometry optimized structures under study: a) bulk TaS_2; b) elongated TaS_2 and c) TaS_2+tert-Butyl isocyanate.*

potential of forming an additional bond, promoting the creation of the corresponding C-S covalent bond. As no information regarding the molecular concentration was available, we assumed the highest possible value, namely one tert-butyl isocyanate molecule per four TaS_2 unit cells. After a careful geometry optimization, the inter-layer distance was found to be 10.96 Å, which shows a good agreement with the experimental value of 10.36 Å. Furthermore the C-S distance obtained was 1.8 Å, which confirms the formation of the C-S covalent bond as the typical length of C-S covalent bonds is 1.7 Å. Additionally, the shortest S-H distance, where S is a sulfur in TaS_2 and H an hydrogen in tert-Butyl isocyanate, is found to be 3.25 Å, far longer than the typical S-H bond length of 1.4 Å, excluding the formation of any S-H bond. Finally, a variation of less than 1% was observed in the supercell angle α.

3.3 Results and Discussion

To summarize, there are three systems under study:

(a) the pristine bulk TaS_2

(b) the pristine elongated TaS_2

(c) the functionalized TaS_2+C_5H_9NO

In Figure 3.3, it is reported the dispersion relations calculated using the harmonic BTE methodology, color coded according to their respective phonon lifetimes calculated using $3rd$ order anharmonicity approximation. In both pristine bulk and elongated systems we have 6 atoms per unit cell (3 atoms for the top layer and 3 atoms for the bottom layer) and we obtain a total of 18 dispersion curves, as expected, 3 of which are acoustic branches and 15 are optical ones. In the functionalized system we have 29 atoms per unit cell, therefore 87 dispersion curves were found. In Figure 3.3 only a portion of system (c)'s dispersion curves are shown in order to offer more clarity in the analysis.

In the pristine bulk system there are three phonon branches that are not present

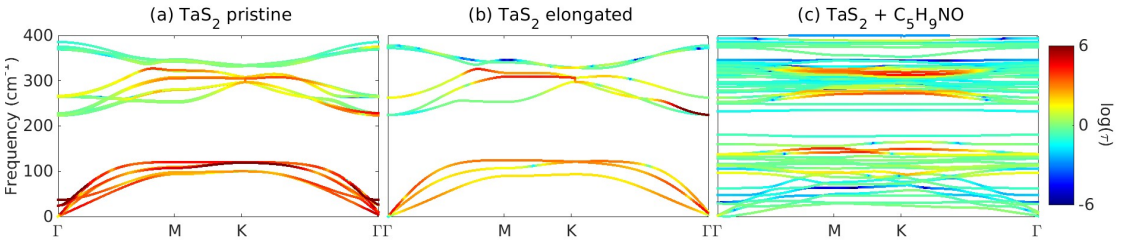

Figure 3.3: *Phonon dispersion relations. Color code (right) showing their respective lifetimes for the three systems under study (a log scale is used for phonon lifetimes).*

in the elongated structure. They show low frequency and large group velocity and lifetimes, showing great similarities with the acoustic branches while being optical in nature. These modes are called quasi-acoustic modes [161], and have

been successfully identified in numerous layered and 2D materials. Their likely cause is the weak interaction between two layers of the material. The results of these quasi-acoustic modes can be summarized in two separate effect in thermal conductivity:

- they add terms in the sum in Equation 2.36, enhancing the thermal conductivity values;
- they scatter the acoustic phonons, decreasing their lifetimes and consequentially decreasing the thermal conductivity.

In literature are reported analysis of these modes for graphene [162, 163] and more recently in BN mono-layers [164], predicting a total negative impact of quasi-acoustic modes in the value of thermal conductivity.
In TaS_2, these quasi-acoustic modes are dominated by the van der Waals interactions between adjacent layers. As we can see in Figure 3.4, they are related to specific inter-layer shear vibrations.
In the elongated system, we cannot identify these quasi acoustic branches. This is caused by the increased inter-layer separation that reduces the effects of the van der Waals forces ($F_{vdW} \propto 1/d$, where d is the inter layer separation). At the distance considered in this study, the interactions are found negligible, so the inter-layer shearing vibrations found in the pristine material disappeared and the phonon branches become two times degenerate. Furthermore, a slight decrease in phonon lifetimes is seen.

By introducing the organic side chains, the dispersion relations change drastically. First of all, there are a great decrease in phonon lifetimes. Furthermore, in this system are present many flat optical branches even at low frequencies that may be considered near dispersionless. These optical modes cross with the acoustic TaS_2 modes causing a flattening even in acoustic branches. Phonon-crossing is a

well known and documented phenomenon found in various materials [165–167] and usually it causes an important decrease in the group velocity of acoustic phonons and a noteworthy decrease in the material anharmonicity, producing a important decreases of thermal conductivity [168]. In the specific case of the TaS_2+C_5H_9NO structure, these low-frequency optical modes are associated with molecular vibrations. In Figure 3.5 is showed a representation of the first three of such modes, in particular we see:

- two rotations of only the butyl group of every side chain introduced in the system;
- the third is a rotation of the hole tert-butyl isocyanate.

In this case, the functionalized system exhibits a significant decrease in phonon lifetimes in both acoustic and optical modes in addition to the flattening of acoustic branches.

In Figure 3.6, it is reported a detailed visualization of the group velocities associated with the acoustic phonons of the three systems. For the bulk TaS_2 the quasi-acoustic phonon's group velocities are reported as well.
By comparing the pristine and elongated TaS_2 systems, the acoustic group velocities are very similar with only small variations. The ZA is the only exception of

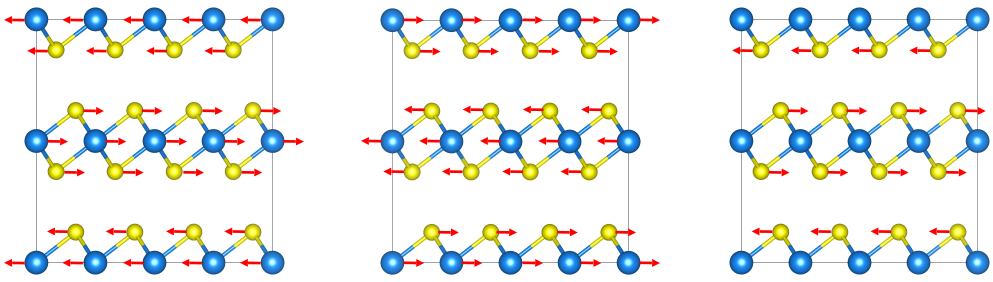

Figure 3.4: *Red arrows visualize the atomic displacements associated with the, first, second and third quasi-acoustic modes in bulk TaS_2.*

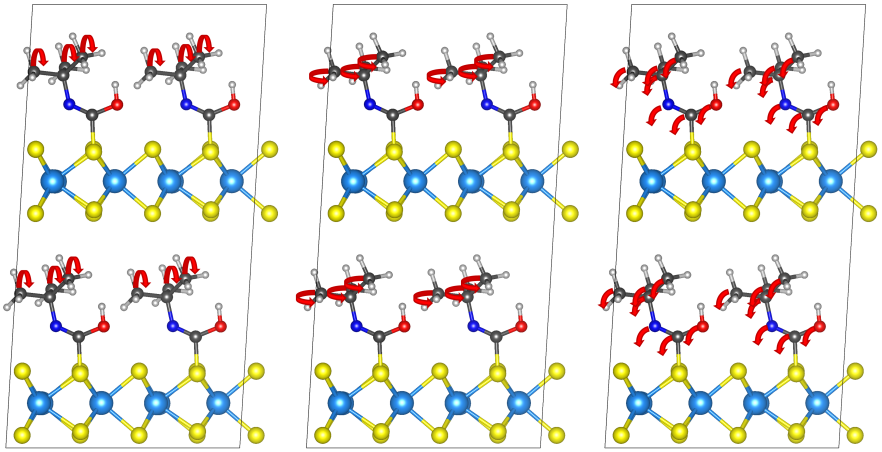

Figure 3.5: *Red arrows visualize the atomic displacements associated with the, first, second and third optical modes in the functionalized system TaS_2 + tert-butyl isocyanate.*

this, being the mode that exhibits the lowest group velocity in the pristine system and an even lower group velocity in the elongated one. Interestingly, the three quasi-acoustic branches in the pristine bulk system have large group velocities comparable with the acoustic ones, confirming their beneficial role in the thermal conductivity calculations.

Finally, in the TaS_2+C_5H_9NO structure, the group velocities are much smaller than the other two systems. This is caused by the mixing of the low-frequency optical modes corresponding to the molecular rotations with the acoustic TaS_2 modes.

In Figure 3.7, a visual representation of phonon lifetimes is reported, in order to further analyze the effects of both increase in inter-layer separation and functionalization.

In the pristine bulk system, it is found that the highest phonon lifetimes values are above 100 ps and they are associated with the quasi-acoustic modes. This, in conjunction with they high group velocity, mark them as only beneficial to the thermal conductivity, in contrast to their role in other system like graphene o BN mono-layers.

Beside the presence of these quasi-acoustic branches, the acoustic phonon lifetimes show only slight differences between the bulk and elongated systems.
In contrast, the functionalized system shows a dramatic decrease in the phonon lifetimes, in both acoustic and optical modes. This is another effect of the phonon-crossing phenomenon and of the high density of phonon branches.

Combining the values for group velocity and phonon lifetime, it is possible to estimate the thermal conductivity with the SM-RTA-BTE method.
The out-of-plane direction shows negligible thermal conductivity values in all of the three structures under study and the presence of the side chain seems to not contribute in neither increasing nor decreasing it.
In contrast, the in-plane lattice thermal conductivity has some noticeable difference. In Figure 3.8 is reported the values of in-plane lattice thermal conductivity as a function of the the temperature in a range 200 K $\leq$ T $\leq$ 500 K.
Here we see the red line representing the thermal conductivity of the pristine bulk TaS_2, the blue line representing the one of the elongated system, the green line representing the thermal conductivity of the functionalized system and the black dots the experimental values. Since the thermal conductivity calculated by [87] is the total value, i.e. the sum of lattice and electronic thermal conductivity, and thus

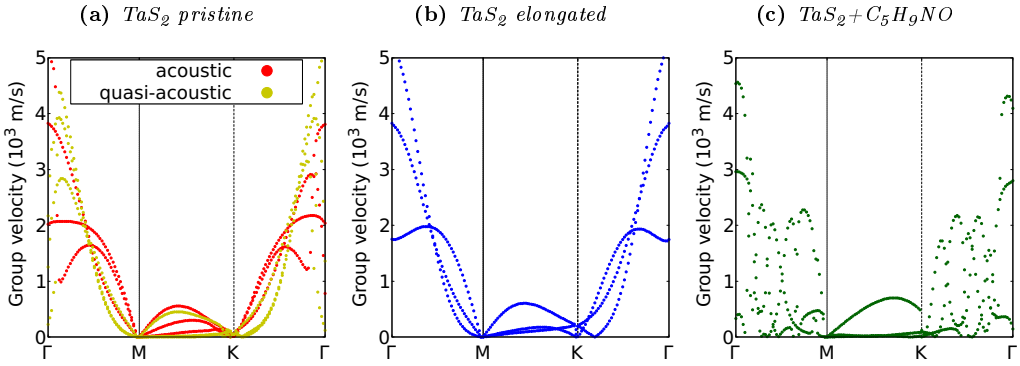

Figure 3.6: *Group velocity of acoustic and quasi-acoustic modes for a) bulk TaS_2, b) elongated TaS_2 and c) TaS_2+C_5H_9NOOS.*

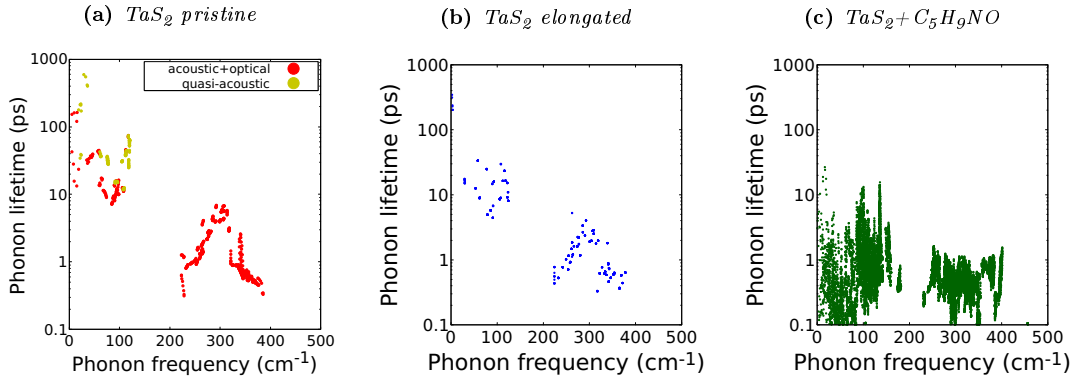

Figure 3.7: *Phonon lifetimes of a bulk TaS_2, b) elongated TaS_2 and c) TaS_2 + C_5H_9NO.*

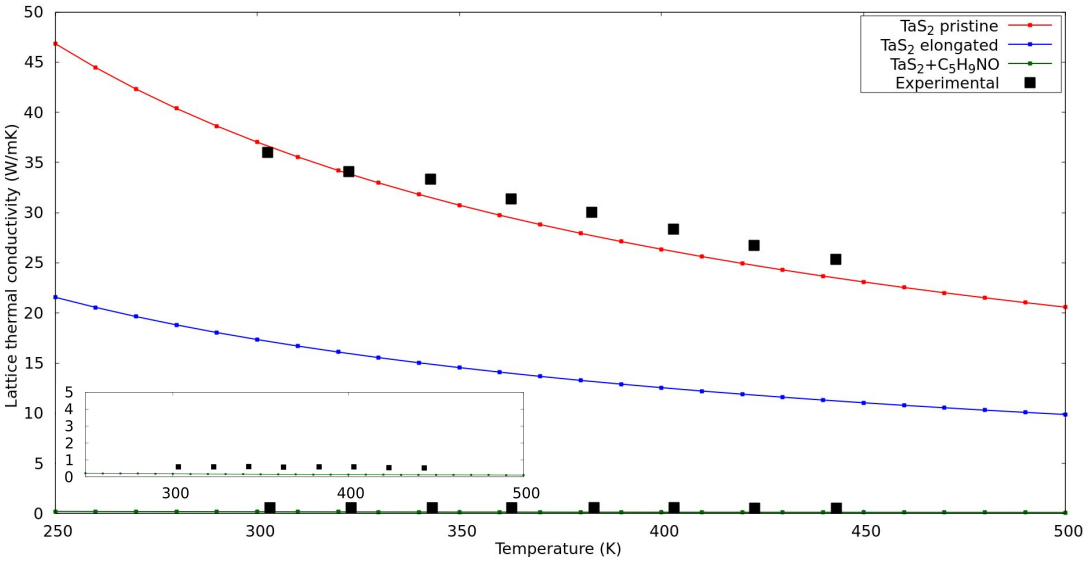

Figure 3.8: *In-plane thermal conductivity of every system in respect of the temperature. The inset emphasizes the comparison between the estimated thermal conductivity and the experimental values for TaS_2 + C_5H_9NO.*

not comparable with the one presented in study (that is only the lattice part), the values showed in Figure 3.8 are obtained by subtracting the electronic contribution calculated using the Wiedemann-Franz law [169]. Interestingly enough, while in the pristine TaS_2 the electronic contribution to thermal conductivity is as small as $\sim$ 10%, in the pristine system becomes predominant, growing as large as the $\sim$ 89% of the total thermal conductivity.

Table 3.1 shows both experimental and calculated values of in-plane lattice ther-

System	Calculated	Experimental [87]
TaS_2 Bulk	37.03	36.00
TaS_2 elongated	17.35	- -
TaS_2 + C_5H_9NO	0.19	0.60

Table 3.1: *Thermal conductivity at 300 K ($Wm^{-1}K^{-1}$).*

mal conductivity fo the three system under study at 300 K.

The calculated values are in strong agreement with the experimental ones. At 300K they showed a deviation from the experimental results as small as 3%, while at higher temperatures there is a small increase in the discrepancy to 5%. This increase is likely due to the Widemann-Franz law implementation to obtain the lattice thermal conductivity. In fact, the Lorentz number was assumed constant with temperature in the calculation of the electronic part of thermal conductivity, but it can exhibit a small temperature dependence [170].

Notable insight can be obtained by comparing the values of thermal conductivity at 300 K.

Figure 3.8 make apparent the results of the presence of quasi-acoustic modes in the pristine bulk system. In fact, only by decreasing the inter-layer separation form 6.02 Åto 10.96 Åa dramatic reduction in thermal conductivity is observed. This reduction is estimated to be $\sim 53\%$ of the original values, from 37.03 $Wm^{-1}K^{-1}$ to 17.35 $Wm^{-1}K^{-1}$. In contrast with other types os 2D materials, in TaS_2 the quasi-acoustic modes give an truly beneficial contribution at the thermal conductivity, thanks to their high phonon group velocity and lifetime.

An additional reduction is obtained by the introduction of the organic molecule, leading to another reduction of $\sim 46\%$. In total, from a value of 37.03 $Wm^{-1}K^{-1}$ to 0.2 $Wm^{-1}K^{-1}$, a reduction almost 99% of the original κ value is observed. This reduction can be attributed to two factors:

1. the disappearance of quasi-acoustic phonon modes discussed above

2. the reduction on both phonon group velocity and lifetime due to the presence of the low frequency optical modes attributed to rotations of the organic molecule.

Finally, from Table 3.1 a discrepancy between the experimental value and the calculated one can be observed in the functionalized system. This may have a number of different causes, but the most convincing one in my opinion is a discrepancy to molecular coverage. In order to make the simulation, as stated above, an uniform distribution of molecule was implemented in the simulation cell, using the highest molecule-TaS_2 ratio possible (1 molecule every 4 TaS_2 unit cells). This two assumption may not be true, since [87] do not explicitly state the molecular concentration. Furthermore, it is possible that the molecules were not distributed uniformly in the TaS_2 crystal, possibility that is not reproducible in our computational setup with periodic boundaries conditions. This two factors combined are expected to affect the calculated lattice thermal conductivity, leading to the found discrepancy.

Another interesting analysis is the one showed in Figure 3.9. The Figure shows:

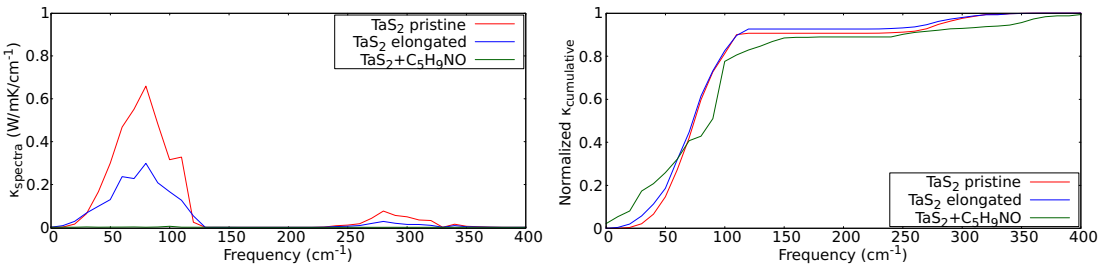

(a) **(b)**

Figure 3.9: *a) Thermal conductivity spectrum b) Cumulative thermal conductivity*

on the left, the spectral thermal conductivity, on the right the corresponding cumulative normalized thermal conductivity. This helps the observation of an interesting phenomenon. In both pristine bulk and elongated TaS_2, almost all the contribution for thermal conductivity originates from the lowest frequencies modes, reaching the 90% value of the lattice thermal conductivity with only contribution from frequencies below 100 cm^{-1}. In contrast, the functionalized system reach a similar percentage of the total values at higher frequencies, i.e. 150 cm^{-1}, denoting the abundance of optical modes in the range of frequencies from 100 to 150 cm^{-1}. In this case, even if the contribution of optical mode is generally low and typically negligible, the overall decrease in both group velocity and phonon lifetime is so predominant that even these otherwise negligible contributions play a significant role in the total thermal conductivity. The Figure 3.10 shows another important

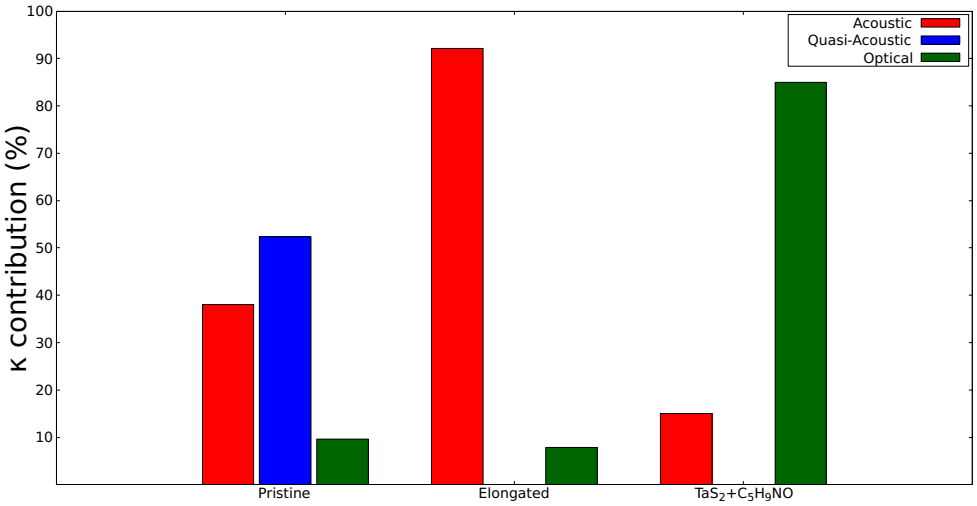

Figure 3.10: *Acoustic, quasi-acoustic and optical contributions to thermal conductivity for the systems of interest*

analysis. By decomposing the thermal conductivity in its acoustic, quasi-acoustic and optical contributions, we can observe some interesting facts. Firstly, the main contribution for the pristine bulk TaS_2 system is derived from the quasi-acoustic mode ($\sim 55\%$), while the acoustic modes contribute by a 35% (for a total of ~ 14

$Wm^{-1}K^{-1}$) and the optical modes contribute by a $\sim 15\%$. In the elongated system, since the van der Waals interaction are negligible, the quasi-acoustic modes are not present, leading to a main contribution derived from acoustic modes, for a total of ~ 15 $Wm^{-1}K^{-1}$ or $\sim 90\%$ of the total thermal conducitvity value. This result is of great import because not only we can finally confirm the pivotal role of quasi-acoustic modes in the thermal conductivity of the pristine system, but we can see how the contribution of the acoustic modes are effectively reduced by the presence of the quasi-acoustic modes. As predicted in other types of material, the increased phonon scattering do decrease the thermal conductivity associated with the acoustic branches (by a small ~ 1 $Wm^{-1}K^{-1}$), but the additional therm is large enough to compensate this reduction and almost double the total thermal conductivity.

Chapter 4

Thermal transport of pristine and defected MoS_2

The investigation presented in the above chapter highlighted a peculiar results: in contrast to the most study 2D materials, TaS_2 shows quasi-acoustic phonon branches in which the positive contribution to thermal conductivity surpass the negative one derived from the addition of scattering channels. To further expand our understanding of this phenomenon, in this chapter a similar study is proposed in MoS_2, a TMD that shows great potential for thermoelectric applications. Furthermore, an investigation on the effect of vacancies is proposed, since this material is often modified with defects before its applications.

Among transition metal dichalcogenoids, MoS_2 has attracted particular attention for its excellent semiconducting properties and mechanical stability. It has been extensively studied for its use in field-effect transistors (FETs), where its high on/off current ratio and atomically thin geometry make it a promising candidate for the development of low-power, high-performance electronic devices [171, 172]. MoS_2, similar to other 2D materials, undergo a drastic change in its properties

when transitioning from bulk to monolayer phase. Notably, variations were found in electronic band-gap [173], Young's modulus [174] and in thermal conductivity. Experimental studies have reported in-plane thermal conductivities for monolayer MoS_2 ranging from a few tens to several hundred $W{\cdot}m^{-1}{\cdot}K^{-1}$, depending on synthesis methods and measurement conditions [85, 175, 176]. Similarly, theoretical estimates vary considerably, from about 20 to over 100 $W{\cdot}m^{-1}{\cdot}K^{-1}$, highlighting the sensitivity of the predicted values to the employed computational methods and assumptions [91, 177–180].

For this reason, a detailed study of the bulk and mono-layer thermal transport properties of MoS_2 is needed, with a particular focus on the effects on quasi-acoustic branches. This investigation was performed using a methodology coherent with the one used for the study of TaS_2, i.e. ab-initio DFT simulations in conjunction with the finite displacements method.

The moderate thermal conductivity combined with the relatively high electrical conductivity of MoS_2 makes it a promising candidate for thermoelectric energy conversion. Efforts to optimize its thermoelectric performance, that is optimizing its figure of merit ZT, have explored strategies such as chemical doping and strain engineering [181, 182]. In this context, nanostructuring and defect engineering have emerged as particularly effective approaches for tailoring lattice thermal conductivity [183–186]. Point defects (e.g., vacancies, interstitials, antisites), line defects (such as grain boundaries), and surface imperfections disrupt lattice periodicity and act as phonon scattering centers, thereby reducing heat transport. Among these, sulfur vacancies are the most commonly observed in MoS_2 and are known to cause a pronounced decrease in thermal conductivity [187]. Extended defects can also serve as phonon barriers, further limiting phonon propagation and enhancing thermal resistance [185, 188, 189].

However, despite the extensive studies performed with the aim of investigate this

topic, the detailed influence of defect spatial distribution on phonon transport remains insufficiently understood. By the development of a deeper understanding of this subject the control of thermal properties of MoS_2 and possibly TMDs as a whole will become possible.

Therefore, this chapter will present a further investigation with the aim of clarify how different spatial arrangements of sulfur vacancies influence the thermal transport properties of monolayer MoS_2. Firstly, a system with randomly distributed point vacancies at various concentrations is considered, in order to explore the impact of a random distribution of vacancies. Subsequently, those previous random vacancies are organized into ordered strips of vacancies, effectively creating a super-periodicity on our simulation cells [190].

Since by introducing vacancies we are losing the crystal periodicity, while it is still possible to obtain some harmonic results using the finite displacement method, fully characterize the defected systems with this methodology is computationally unsustainable, especially if used in conjunction with DFT ab-initio simulations. For this reason, the of all defected systems was performed using the AEMD method. In order to obtain further clarification, a lattice dynamics calculation using the finite displacement method is reported, using molecular dynamics simulation to calculate the 2nd order interatomic force constants.

4.1 Computational details

The calculations of the pristine systems, both in the bulk and mono-layer phases, presented in this chapter rely on the Density Functional Theory (DFT) with periodic boundaries condition performed with the Quantum espresso package [158].

In all calculations the corrected generalized gradient approximation of Perdew,

Burke and Ernzehof [159], PBEsol [139], with Projector-Augmented Wave (PAW) pseudopotentials [160] and a plane-wave basis set were used.

In all DFT calculations, a plane-wave kinetic energy cutoff of 60 Ry and a charge-density cutoff of 480 Ry were used. The convergence criteria for the total energy and atomic forces were set to 10^{-15} Ry and 10^{-12} Ry Å^{-1}, respectively. For each of the three investigated systems, the Brillouin zone was sampled using a k-point mesh corresponding to a reciprocal-space density of 0.1 Å^{-1}.

The thermal properties were evaluated using the finite-displacement method described in section 2.5, as implemented in the ALAMODE package [144]. Anharmonic interactions were included up to third order. The supercell employed for both harmonic and anharmonic calculations contained 96 atoms, corresponding to a $4 \times 4 \times 2$ replica of the unit cell. For the harmonic calculations no inter-atomic interactions cutoff was imposed, while for the anharmonic calculations a cutoff corresponding to the distance between first-neighbor atoms was introduced.

However, by introducing vacancies in the system, the symmetry of the crystal is lost and performing ab-initio, DFT calculations with finite displacements would be computationally overwhelming. For this reason, the calculations of the defected systems presented in this chapter are molecular dynamics calculations preformed with the LAMMPS package [140] with a modified Stillinger–Weber potential for TMDs and MoS_2 [191, 192].

The simulation cell employed was a $L_x \times 16b$ replica of the unit cell, with L_x ranging from 31.2 to 623.5 nm, corresponding to $100a$-$2000a$. As discussed above, the AEMD method is influenced by size effects, thus the need to investigate the thermal conductivity in systems with increasing length.

Furthermore, to avoid any interaction between MoS_2 layers caused by the periodic boundaries conditions, an artificial cell height of $L_z = 5$ nm was set.

To ensure statistical reliability, configurational averages were calculated over several independent simulations, ranging from 20 replicas for the smallest systems to 2 replicas for the largest one, each initialized with different atomic velocities.
Moreover, every simulation with random point vacancies was initialized using a different distribution of vacancies, in order to avoid thermal conductivity's dependence on the specific vacancies distribution. The number of simulations per system varied from 20 replicas for the smaller systems to 2 for the larger ones.
Finally, the initial condition for the simulation (i.e. the step-like temperature profile described above) were imposed by performing two separate NVT runs, both of the duration of 10 ps, in order to create two regions with different temperature, $T_H = 325$ K and $T_C = 275$ K. Then, the system was evolved through NVE simulations with a duration depending on the system length, varying from 360ps to 7 ns, in order to let every configuration reach thermal equilibrium.

4.2 Systems under study

Bulk MoS_2 has two main stacking types, the 2H-AA' and 2H-AB. Both configurations posses comparable amount of energy, and usually the 2H-AA' is considered stable at 0 K while the 2H-AB is considered metastable [193].
Therefore, both AB and AA' stacking types were considered for this investigation. After a meticulous optimization of both the unit cell and atomic positions, the resulting systems showed similar lattice parameters, as shown in Table 4.1. The most noticeable difference is in the c parameter, that corresponds to the inter-layer separation, that has a variation of 6% in the transition from the AA' to the AB stacking.
As shown in Table 4.1, the mono-layer shows similar lattice parameters to the bulk

Stacking type	a (Å)	b (Å)	c (Å)
AA'	3.18	5.21	6.59
AB	3.12	5.11	6.22
mono-layer	3.14	5.13	–

Table 4.1: *Lattice constants of MoS_2 obtained via DFT simulations.*

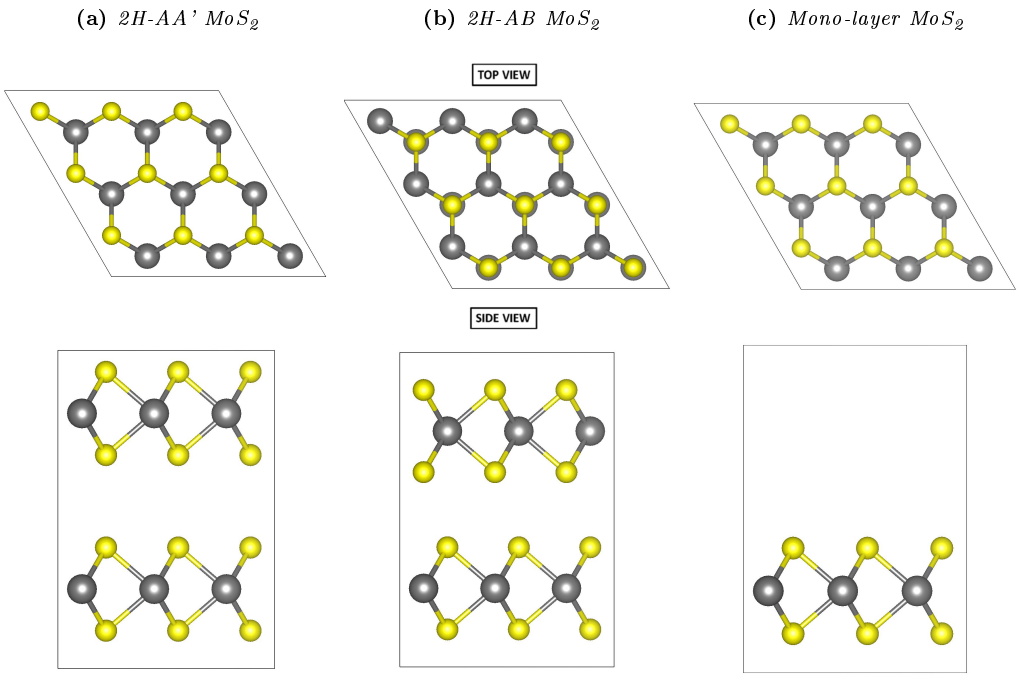

Figure 4.1: *Stick and balls representation of the three structures under study: a) 2H-AA' MoS_2; b) 2H-AB MoS_2 and c) mono-layer MoS_2.*

systems.

In Figure 4.1 is found the stick and balls representation of the three systems. As discussed above, the effects of vacancies in MoS_2 mono-layer were investigated using the AEMD method. Since this techniques relies on molecular dynamics instead of DFT, starting from the optimized structure obtained above a new MD relaxation was performed. The lattice parameter obtained are reported in Table 4.2 along with the results of the DFT optimization. As showed, the lattice parameters

Simulation method	a (Å)	b (Å)
DFT	3.14	5.13
MD	3.12	6.39

Table 4.2: *Lattice constants of mono-layer MoS_2.*

of the systems resulting from the optimizations performed with the two methodologies give similar results. The lattice constant c, corresponding to the out-of-plane dimension, is not calculated because the system studied are composed of only a single atomic layer.

Next, the vacancies were introduced in the MD-optimized system. In order to simulate the experimental etching process, only sulfur atoms belonging to the top S layer. To clarify, even if we are referring to the system as "mono-layer", the single layer of MoS_2 is composed by three different atomic layer: a top Sulfur layer, a in between Molybdenum layer and a bottom Sulfur layer. The bulk material is compose by a multitude of this three layers systems stacked atop each other, hence the studied system can be classified as a monolayer.

Firstly, the vacancies were introduced with a random distribution. This point Sulfur vacancies had a density defined as $\rho_s = N^S_{removed}/N^S_{top}$, where $N_{removed}$ is the number of Sulfur atoms removed and N^S_{top} is the number of atoms present in the top Sulfur layer. The densities of vacancies considered is ρ_S = 1%,2.5%,5% and 10%. An example of such system is provided in the top panel of Figure 4.2, where the blue region represent the Sulfur atoms and the pink regions represents the random point vacancies.

Next, the vacancies were rearranged in a ordered distribution, forming strips of vacancies. As for the random distributions, this strips of atoms were removed only from the top Sulfur layer and the vacancy lines are arranged along the direction perpendicular to the heat propagation. From this point, the direction of heat propagation will be referred as the x direction.

Furthermore, in order to maintain the number of vacancies fixed at given ρ_S, the width w_S of each strip is chosen as:

$$w_S = \frac{h}{n_S}\frac{L_x}{a}\rho_S; \tag{4.1}$$

where $h = 3.14$ Åis the minimum distance between two Sulfur atoms in the x direction, n_S is the number of vacancies strips etched in the system and L_x is the simulation cell length in the x direction. By defining the strips width in this way, it is possible to easily determine the width of the strips in function of their number, observing that in systems with the same number of vacancies a larger number of strips corresponds to a smaller width.
Finally, the distance between strips can be defined as:

$$d_S = (L_x - w_S)/n_S. \tag{4.2}$$

In the bottom panels of Figure 4.2, some examples of systems with ordered line Sulfur vacancies are showed. Notice how in all panels the vacancy density is constant.

Furthermore, after the creation of the vacancies, an additional structural optimization was made for every sample, in order to observe the presence of eventual modifications in lattice parameters induced by the removal of Sulfur atoms. These modification were found in every system, although they are only of minor entity, with strain of the order of 0.6% for L_x and 0.7% for L_y in the systems with random vacancies, while they were even smaller for the system with ordered strips (in the order of 10^{-3} Å). So we can conclude that structural modification do not play a role in the results discussed below.

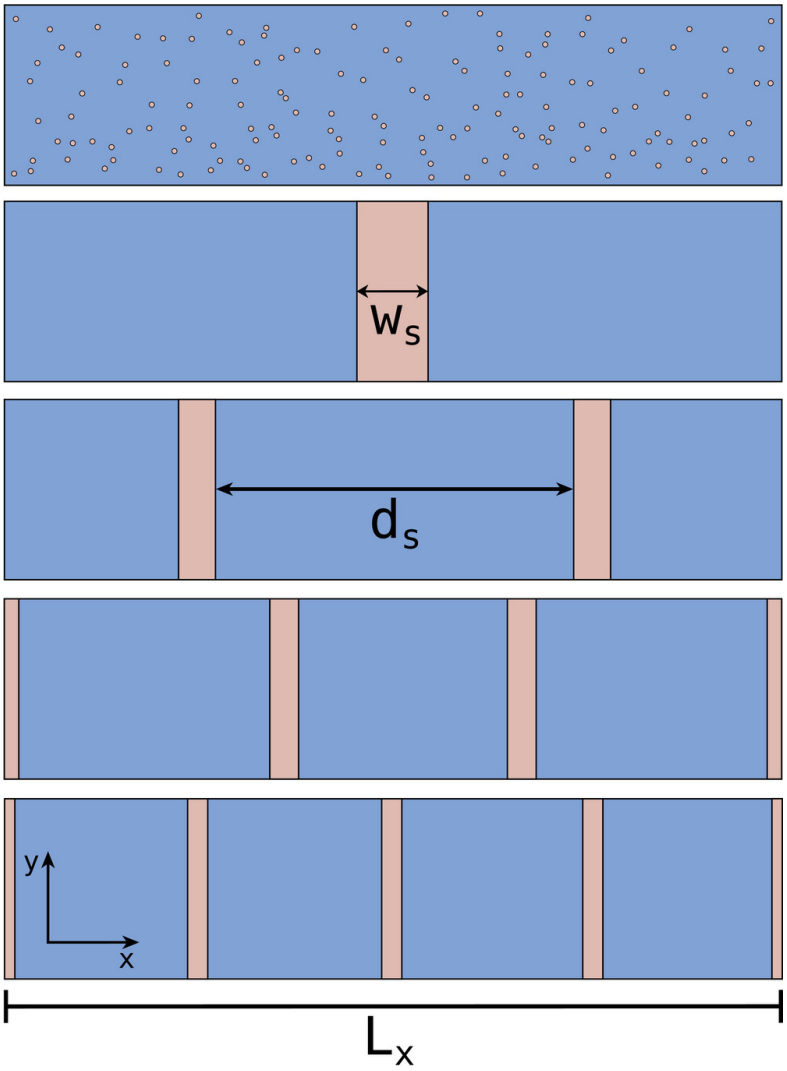

Figure 4.2: *Representation of some defected systems under investigation. The blue regions represent the pristine MoS_2, while the pink regions represent the Sulfur vacancies.*

4.3 Results and discussion

Firstly, the results of the DFT ab-initio investigation will be showed. To summarize, we have three different systems under analysis:

(a) the pristine bulk MoS_2 in its 2H-AA' stacking;

(b) the pristine bulk MoS_2 in its 2H-AB stacking;

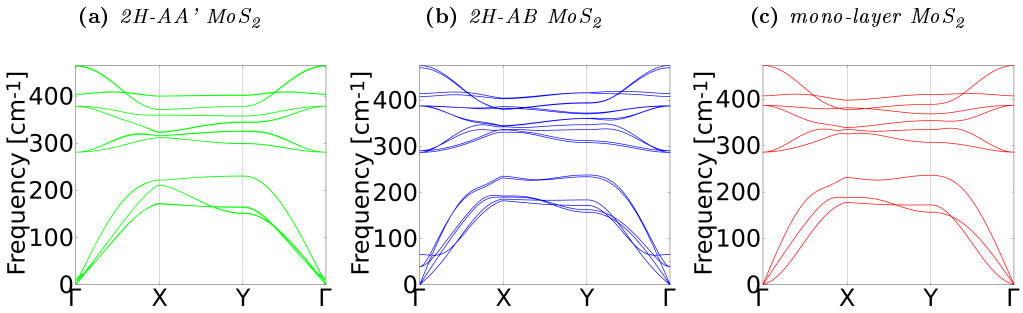

Figure 4.3: *Dispersion relation curves for a) 2H-AA' MoS_2, b) 2H-AB MoS_2 and c) mono-layer MoS_2.*

(c) the mono-layer MoS_2.

In Figure 4.3 are reported the dispersion relations of these three systems. In both bulk systems, the quasi-acoustic curves are present and are related to inter-layer sheer vibrations, similar to the ones found in bulk TaS_2. However, the two systems show large differences in their quasi-acoustic branches.

In the AA' system, the quasi-acoustic modes are almost degenerate with the acoustic ones and at the Γ point have very low frequencies ($\omega^{qa}_{AA'} < 10\text{cm}^{-1}$) . Meanwhile, in the AB system, the quasi-acoustic branches are more similar to the ones found in TaS_2: they show low frequency but higher than the AA' system ($\omega^{qa}_{AB} \geq 40\text{cm}^{-1}$), and cross the acoustic phonon curves relatively far from the Γ point.

The mono-layer system does not show any quasi-acoustic modes, as expected, and show phonon dispersion curves similar to the ones observed in the AB system.

In Figure 4.4 are shown the group velocities for acoustic and quasi-acoustic phonons of the three systems. As expected, the group velocities of acoustic and quasi-acoustic phonons in the AA' are nearly degenerate, showing high group velocity in all six modes. In contrast, in the AB system, while the group velocity of acoustic phonons is nearly identical to the one in the AA' system, the quasi-acoustic phonons exhibit lower group velocities compared to the previous case, yet still high enough to provide a positive contribution to the thermal conductivity.

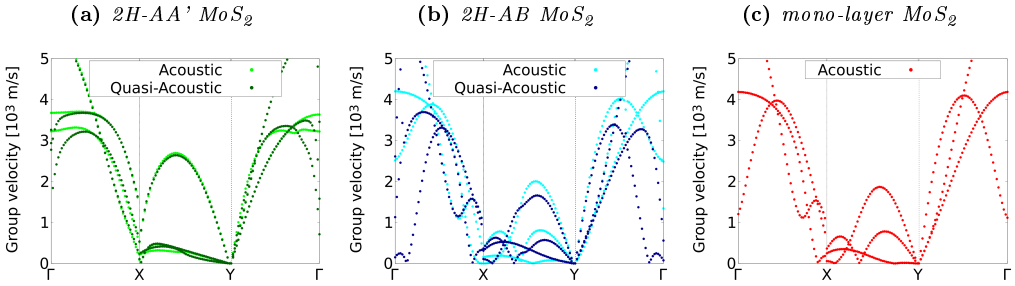

Figure 4.4: *Group velocity for acoustic and quasi-acoustic phonons for a) 2H-AA' MoS_2, b) 2H-AB MoS_2 and c) mono-layer MoS_2.*

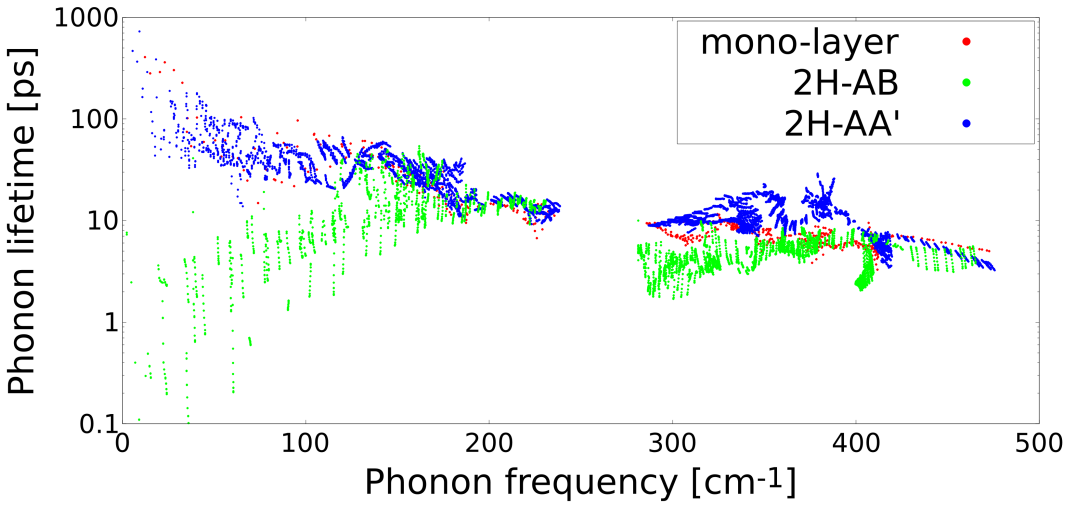

Figure 4.5: *Third order phonon lifetimes of 2H-AA' MoS_2, 2H-AB MoS_2 and mono-layer MoS_2.*

In Figure 4.5 are showed the phonon lifetimes of the three systems.

As shown, while AA' and mono-layer systems exhibits similar phonon lifetimes, the AB system undergoes a drastic reduction.

Combining the informations just presented, we can calculate the thermal conductivity of the systems. As for the TaS_2 investigation, in MoS_2 too the out-of-plane direction gives thermal conductivity near zero and its variations are too small to be appreciable. For this reason, only the in-plane thermal conductivity will be analyzed. Such thermal conductivity can be seen in Figure 4.6.

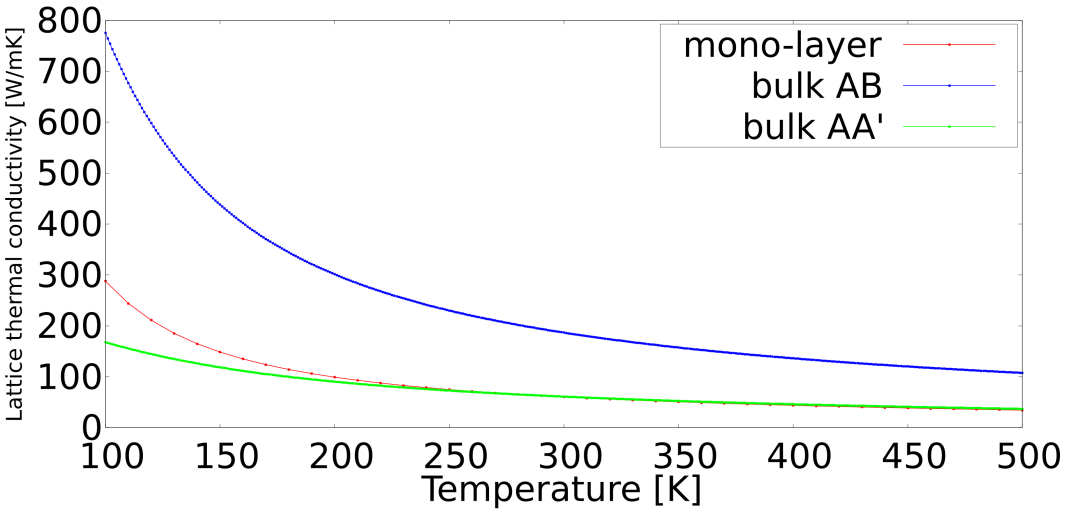

Figure 4.6: *Third order in-plane thermal conductivity of 2H-AA' MoS_2, 2H-AB MoS_2 and mono-layer MoS_2.*

While the relation between bulk 2H-AB and the mono-layer systems is similar to the one discovered between the TaS_2 systems, in the AA' system the thermal conductivity becomes similar to the one of the mono-layer system, becoming even smaller at low temperatures. The thermal conductivities at 300 K can be found in Table 4.3.

This is a really interesting fact, because with this it is possible to see both

Table 4.3: *Thermal conductivities at 300 K of MoS_2 various systems.*

System	Thermal conductivity (W/mK)
2H-AA'	61.1002
2H-AB	186.7594
Mono-Layer	58.2680

quasi-acoustic mechanism in action. As mentioned in the previous chapter, quasi-acoustic phonon modes have two different effects on the system: they add terms in the equation for the thermal conductivity but they increase the scattering channels for acoustic phonons. In TaS_2, the combination of those two effect leaded to an overall increase in thermal conductivity and in the 2H-AB phase of MoS_2

the same is true. In contrast, the increased scattering effect in 2H-AA' MoS_2 is much greater than before, as shown by the drastic reduction in phonon lifetimes, thus leading to a thermal conductivity comparable to the one in the mono-layer system. This shows how a different stacking type may greatly affect the in-plane thermal conductivity and consequently a material performance in thermoelectric applications.

4.3.1 Effect of defects

Starting from the geometry of the mono-layer system described above, now the defected systems will be discussed using the AEMD method.

Figure 4.7 presents the evolution of the thermal conductivity (κ) as a function of the system length (L_x), the number of strips (n_s), and the sulfur-vacancy concentration (ρ_s).

As stated above, finite-size effects are intrinsic to non-equilibrium methods like AEMD, often resulting in the broad range of κ values reported in literature. Since the aim of this study is to estimate the effects on thermal conductivity derived from the introduction of Sulfur vacancies, he present work does not extrapolate κ_∞ for either pristine or defected configurations, as this lies beyond the intended scope. Instead, defected systems are directly compared with pristine counterparts of the same dimensions. The results show that ordered samples exhibit a length dependence comparable to the pristine system, supporting a consistent comparative approach.

As expected, MoS_2 mono-layers with randomly distributed sulfur vacancies display a reduction in thermal conductivity, which tends to saturate for increasing simulation lengths. The introduction of random vacancies enhances phonon scattering, thereby shortening their mean free paths and resulting in a pronounced decrease

of κ with increasing density of vacancies.

In contrast, systems with ordered vacancy strips show a distinctly different behavior: the thermal conductivity is reduced, but in a non-trivial manner. Remarkably, increasing the number of vacancies (or equivalently, the width of the defective region) does not necessarily lead to a further suppression of thermal conductivity. This finding highlights that by creating ordered vacancy a superlattice periodicity is imposed and that it plays a predominant role in determining thermal transport. To further analyze this result, Figure 4.8 summarizes the thermal conductivity de-

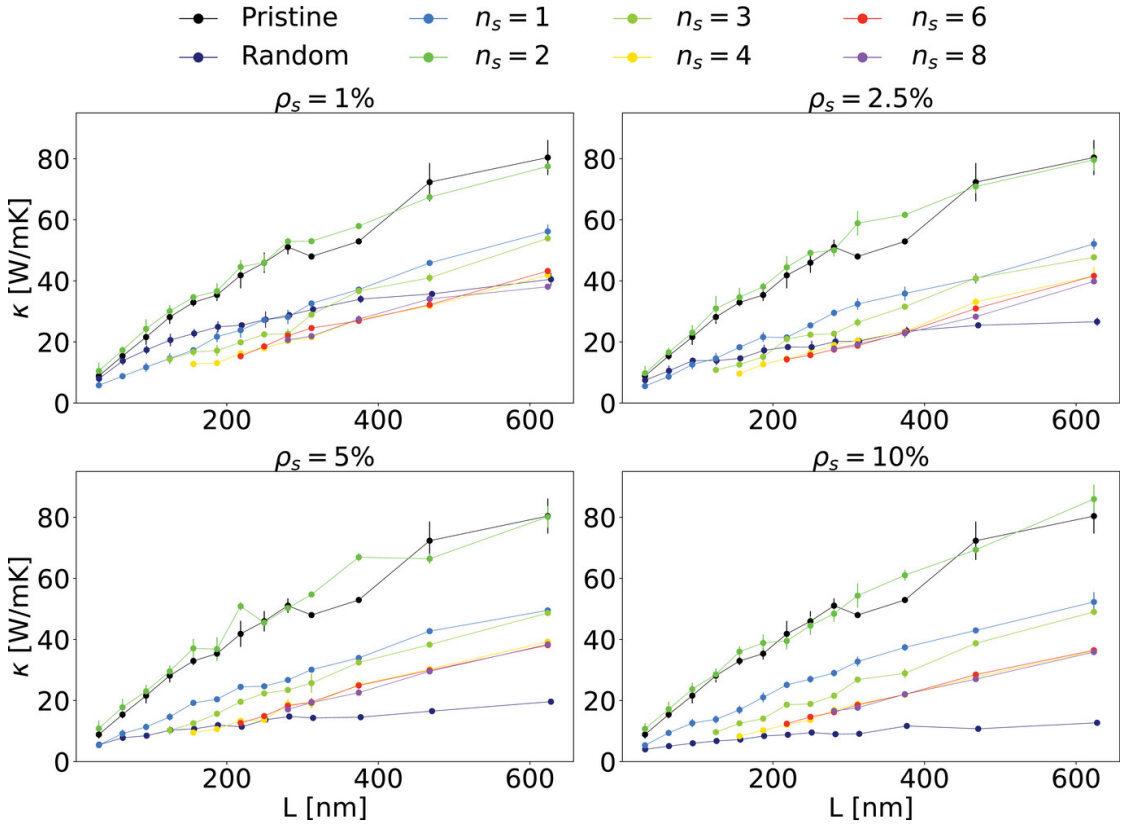

Figure 4.7: *Thermal conductivity at 300 K of pristine MoS_2 (black line), MoS_2 with random point vacancies (dark-blue line) and MoS_2 with n_S strips of ordered vacancies (other colored lines) in function of the simulation cell length. The four panels represent, in order from to left to bottom right, the system with $\rho_S = 1\%.2.5\%.5\%$ and 10% [190].*

pendence on the superlattice periodicity n_s. Notably, for $n_s = 2$, κ nearly coincides with that of the pristine system, independently of both vacancy concentration and

system size. This result demonstrates that a specific defect periodicity can effectively restore the intrinsic phonon transport of pristine MoS_2, despite the presence of atomic vacancies.

In general, reduced thermal conductivity is associated with a decrease in phonon

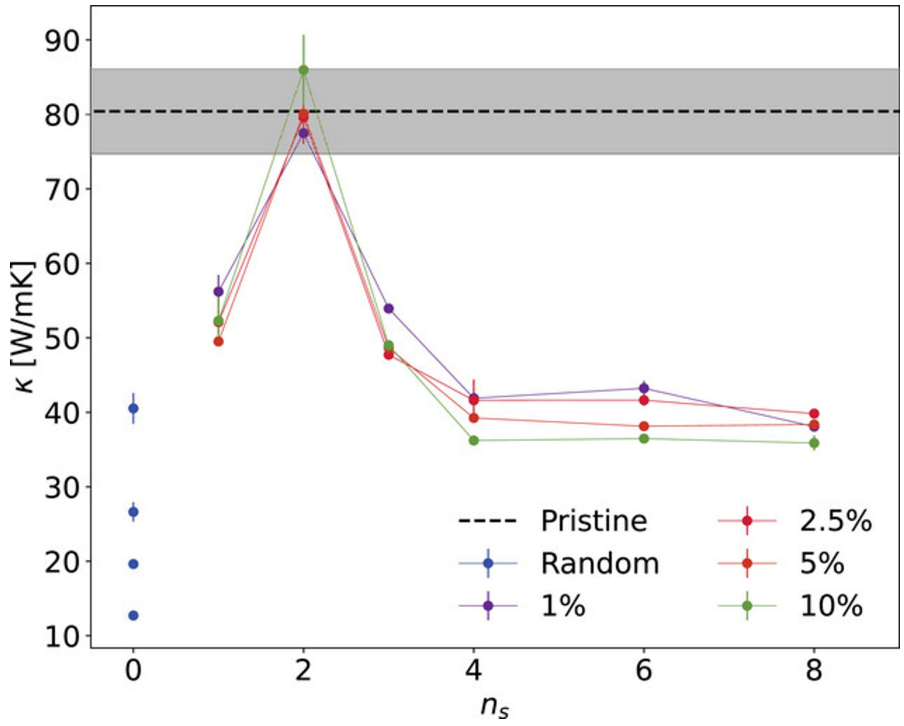

Figure 4.8: *Thermal conductivity at 300 K of the various defected systems in function of the number of vacancies' strips. The system with random point vacancies is considered as having $n_S = 0$. The black line represents the thermal conductivity of the pristine system and the gray band represent its standard error [190].*

mean free paths caused by defect or interface scattering. However, in the case of ordered defect superlattices, the imposed periodicity enables phonons of particular wavelengths to propagate coherently across the structure. As shown in Figure 4.9, the thermal conductivity of the system for a given superlattice period of $n_S = 2$ depends monotonically on the distance between two strips. In fact, when the distance between adjacent defect strips is below approximately 20 nm, κ approaches the value obtained for the $n_s = 1$ configuration. Conversely, when four strips are

merged into two equispaced ones, κ rapidly converges to the $n_s = 2$ value even before full coalescence occurs. This behavior indicates the presence of a critical separation distance, beyond which phonons perceive multiple adjacent vacancy regions as a single coherent scattering center.

While the realization of super lattices obtained by combining two materials is extensively studied for the purpose of creating phonon barriers, superlattices that actively increase the thermal conductivity by enhancing phonon propagation are not so common.

Such behavior closely resembles that observed in Moiré-type superlattices, where the imposed superperiodicity modulates phononic and electronic properties as a function of the twist angle. To further clarify the microscopic origin of these effects,

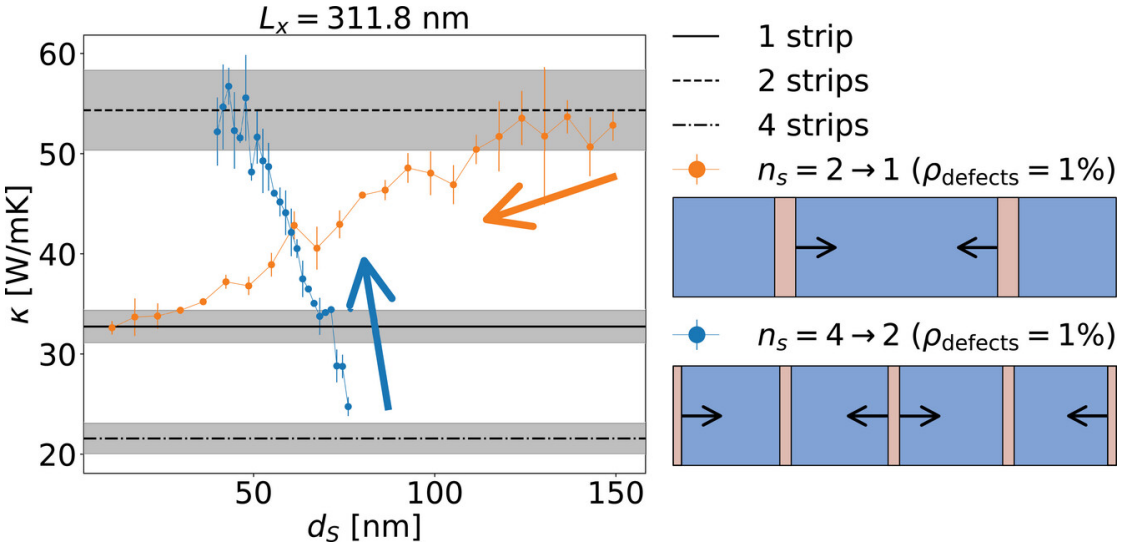

Figure 4.9: *Effect of merging two vacancy strips into a single one, or four strips into two equally spaced ones, in the $L_x = 311.8$ nm sample, as indicated by the arrows in the plot and the schematic on the right. The shaded regions represent the standard errors associated with the calculated thermal conductivities for the corresponding configurations. [190]*

a lattice dynamics study is needed. As stated above, the introduction of defects leads to a loss of symmetry in the crystal. More specifically, this actively decrease the number of symmetry operation allowed during the building of the dynamical

matrix, leading to a drastic increase in the number of both atomic displacements and inter-atomic force constants needed to fully estimate the dynamical matrix. This limits the maximum dimension possible for the simulated cell. For this reason, the system considered is a simulation cell containing a total of 96 atoms from which 6 sulfur atoms were removed from the top layer. The distributions of vacancies considered were random point and ordered distributions with $n_s = 1$,2 and 3.

The calculated cumulative and spectral thermal conductivity (Figure 4.10) reveals

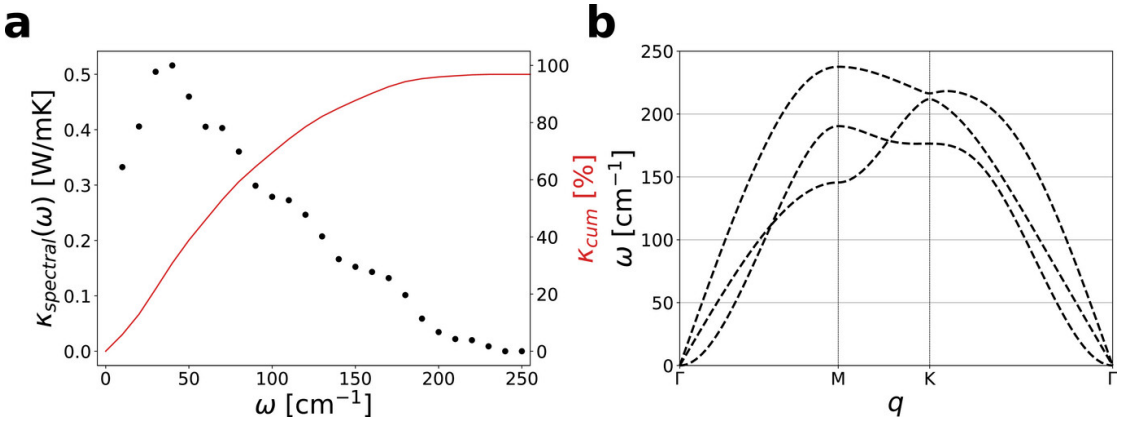

Figure 4.10: *a) Spectral thermal conductivity (black dots) and cumulative thermal conductivity (red line) of pristine mono-layer MoS_2 obtained with MD simulations in function of the frequency; b) acoustic phonon dispersion curves of pristine mono-layer MoS_2 obtained with MD simulations [190].*

that the dominant contribution to the thermal conductivity arises from frequencies below 250 cm^{-1}, confirming that acoustic phonons are the primary heat carriers in MoS_2. Approximately 70% of the total κ originates from phonons below 100 cm^{-1} as shown by the dispersion curves for the pristine mono-layer; thus, the subsequent analysis focuses on this frequency window. Note that these results are obtained using the software LAMMPS in conjunction with MD simulation that relayed on the same potential used for the AEMD simulations, thus explaining the differences from the dispersion curves discussed before.

The mode-averaged phonon group velocities along both the x- and y-directions

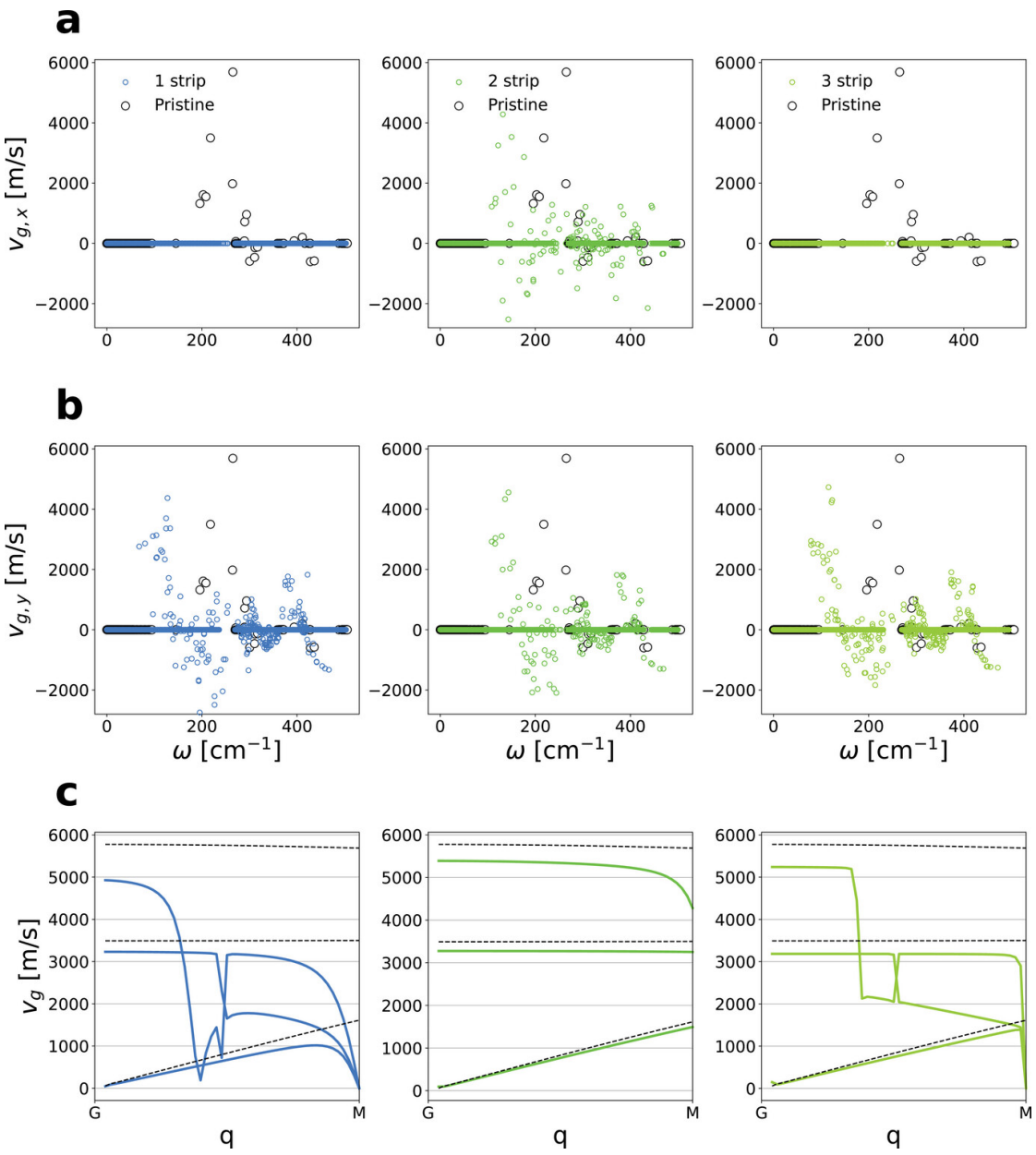

Figure 4.11: *a,b) Mode-averaged phonon group velocities along the x and y directions, respectively. c) Absolute values of the group velocity (v_g) along the $\Gamma \rightarrow M$ direction for the acoustic modes of pristine MoS_2 (black dashed lines) and the defected monolayers [190].*

$(v_{x,y}(\omega)\frac{1}{m}\sum_{\boldsymbol{q}j}^{m}\boldsymbol{v}_{\boldsymbol{q}j}(\omega)$ see Figure 4.11 a,b) show that while vacancy-induced defects generally reduce v_x, the $n_s = 2$ superlattice preserves a significant fraction of propagating modes with finite group velocities. This implies that the periodic

defect ordering maintains efficient phonon transmission. Along the y-direction, parallel to the vacancy strips, the group velocities remain nearly identical to those of pristine MoS_2, indicating minimal influence on in-plane anisotropy.

A detailed inspection (Figure 4.11) shows that in the $n_s = 1$ and 3 configurations, both longitudinal acoustic (LA) and transverse acoustic (TA) modes experience a marked reduction in group velocity near the Γ point, particularly for the LA branch, which contributes most significantly to heat transport. This reduction stems from localized vibrational states at the interfaces between defective and pristine regions, which strongly scatter LA phonons. In contrast, for $n_s = 2$, the group velocities remain almost unchanged compared to the pristine case, with minor deviations only at the Brillouin-zone edges. Consequently, κ is effectively preserved in this configuration. The phonon dispersion relations (Figure 4.12 a) reveal that defect introduction generally produces additional low-frequency optical modes, which tend to hybridize with acoustic branches and enhance phonon-phonon scattering. However, in the $n_s = 2$ system, these defect-induced modes shift toward higher frequencies, resulting in the formation of a phononic bandgap that minimizes coupling between acoustic and optical branches. This suppression of acoustic-optical scattering leads to longer phonon mean free paths and hence higher κ.

This conclusion is further substantiated by the participation ratio (PR) analysis (Figure 4.12 b). In pristine MoS_2, PR values remain close to unity for all modes, indicating fully delocalized vibrations. For the $n_s = 1$ and 3 configurations, 10-15% of the modes exhibit PR < 0.8, denoting substantial localization. Conversely, in the $n_s = 2$ superlattice, fewer than 3% of modes are localized, confirming a predominance of delocalized phonons and reduced scattering. The reduced localization directly limits Umklapp scattering, thereby decreasing thermal resistance.

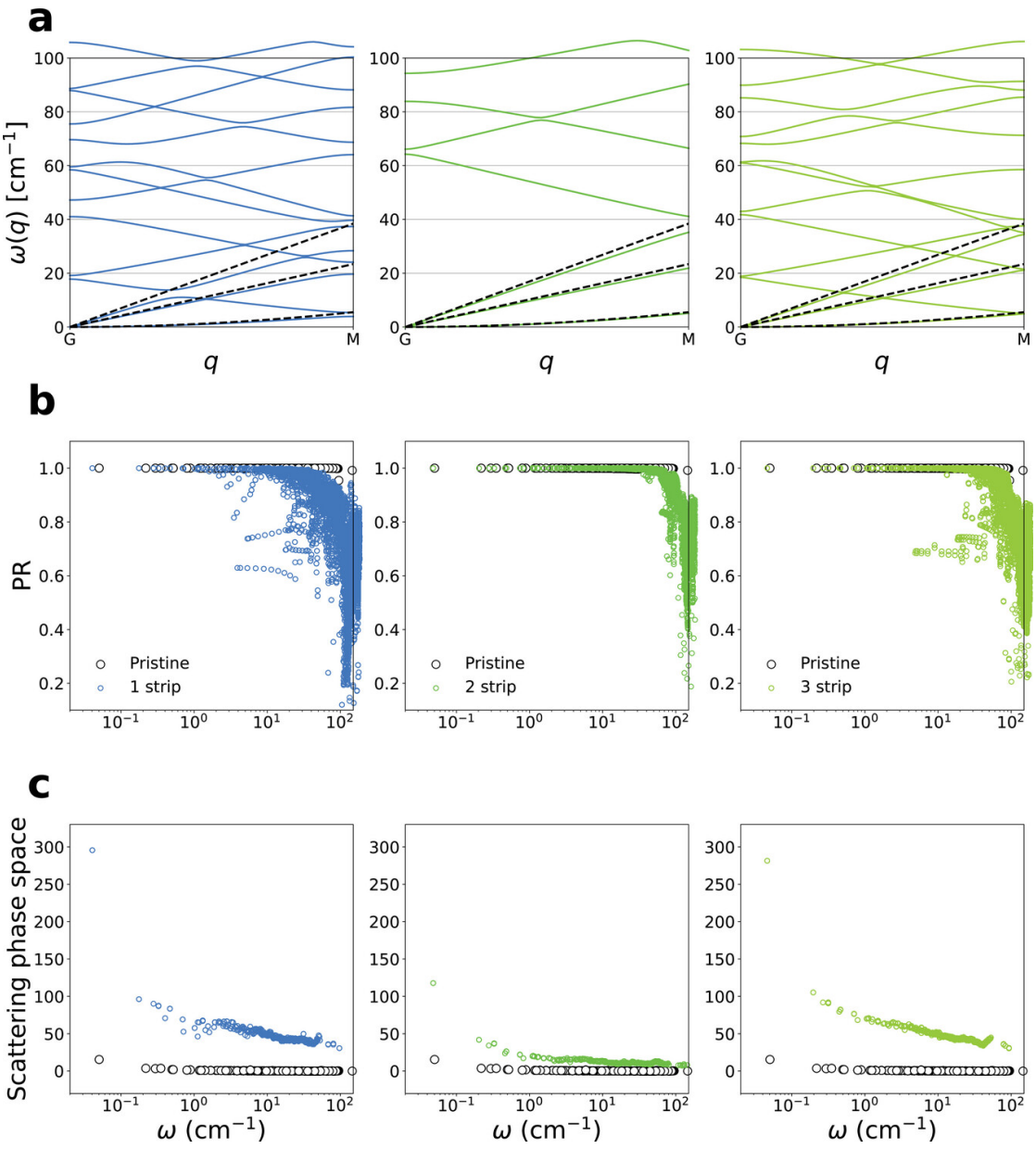

Figure 4.12: *a) Phonon dispersion curves along the $\Gamma \rightarrow M$ direction. Black dashed lines indicate the acoustic branches of the pristine monolayer. The dispersions are folded according to the Brillouin zone of the supercell used in the lattice-dynamics (LD) calculations; b) participation ratio of defected systems (colored circles) and pristine mono-layer MoS_2 (black circles); c) three-phonon scattering space of defected systems (colored circles) and pristine mono-layer MoS_2 (black circles) [190].*

Finally, the three-phonon scattering phase space (Figure 4.12 c) provides quantitative insight into phonon-phonon interaction probabilities. While pristine MoS_2 displays a narrow phase space, implying limited scattering channels, the $n_s = 1$ and 3 systems exhibit a significantly expanded phase space, consistent with their reduced κ. In contrast, the $n_s = 2$ configuration presents a considerably restricted phase space, likely due to the enhanced lattice symmetry and stricter selection rules governing three-phonon processes. This outcome highlights the possibility of tuning phonon dispersion and scattering through defect periodicity, enabling the design of phononic metamaterials with tailored thermal properties.

In summary, the combined AEMD and lattice-dynamics analyses demonstrate that ordered sulfur-vacancy distributions in MoS_2 can substantially modulate phonon transport. Specifically, a defect periodicity corresponding to $n_s = 2$ enables the recovery of pristine thermal conductivity by suppressing acoustic-optical phonon interactions and reducing mode localization. These findings establish defect superlattices as an effective strategy for phonon engineering in two-dimensional materials, providing a pathway toward controlled thermal management in nanoscale devices.

Chapter 5

Anomalous thermal transport of BTBT and DNTT

Organic molecular crystal are materials belonging to the class of organic semiconductors that have been used extensively in the last decades for a wide range of applications, such as organic field-effect transistor and solar cells. Thus, both electrical and optical properties have been extensively investigated, while their thermal behavior is relatively unexplored.

In order to investigate their effectiveness as thermoelectric generators, a thorough study of their thermal transport properties is needed.

In the previous chapter was shown how harmonic properties, such as quasi-acoustic modes or phonon crossing, can lead to massive change in a material thermal behavior and in their anharmonic properties, such as phonon lifetimes and scattering rates being lowered by the presence of low frequency optical modes. This behavior is due to the low anharmonicity of the materials proposed and a third order investigation was enough to fully characterize their thermal properties.

However, organic molecular crystals can show strong anharmonic behavior that sometimes can affect their harmonic properties. Some example of this are the

temperature dependence on phonon frequencies or phonon mixing [97]. In such cases an investigation to the third order is not enough to fully characterize the thermal properties of the material, leading to false prediction of their thermal conductivity and Raman spectrum. It is possible to compute higher order of anharmonicity, but it would greatly increase the computational time and for larger systems it would lead to unsustainable computational times.

Recent studies have shown that certain prototypical molecular crystals exhibit pronounced higher-order anharmonic effects. In particular, [1]benzothieno[3,2-b]-benzothiophene (BTBT) displays temperature-dependent vibrational frequencies in its Raman spectra,an effect typically attributed to quasi-harmonic behavior arising from thermal lattice expansion [97]. However, polarized Raman measurements have also revealed evidence of phonon mixing in BTBT, which can be interpreted as a deeper manifestation of anharmonicity. This phenomenon cannot be explained within the conventional framework of independent harmonic oscillators, thus the inclusion of high level of anharmonicity is mandatory to the study of this material. The most appreciable manifestation of anharmonicity is in thermal conductivity, thus a detailed study of this property in BTBT can be useful to demonstrate the importance of accounting effects beyond third order anharmonicity.

For this purpose, a detailed investigation of thermal conductivity based on multiple approach is proposed in this chapter. Specifically, the methods used are:

- AEMD, a more phenomenological approach that accounts for every level of anharmonicity but do not give information about the microscopical thermal transport;
- SM-RTA-BTE with finite displacement methodology both using normal mode decomposition MD and to the third order of anharmonocity simulations;
- Wigner approach using normal mode decomposition MD simulation.

In the MD simulations, a GAFF force field was employed. The force field was validated against ab-initio and experimental results [97].
Moreover, since the AEMD and the Wigner methods showed an unexpected similarity, a analogous study on the 2,9-Dioctylnaphtho[2,3-b]naphtha[2',3':4,5]thieno[2,3-d]thiophene (DNTT) system was performed.
DNTT is another organic molecular crystal with similar properties to BTBT. In fact, DNTT too showed great anharmonicity and phonon mixing [124]. In order to confirm and further explore the similarity between AEMD and the Wigner approach, all the calculations already performed for the BTBT systems were replicated for the DNTT system.

5.1 Computational details

In this chapter, as stated above, various calculation methods were employed that are based on molecular dynamics. The code LAMMPS was employed to perform all the MD simulations. The GAFF force field was used to perform the simulations after validation with ab-initio results [194].
For the finite displacements approach, a $2 \times 4\times$ supercell was used, for a total of 1536 simulated atoms. Using a timestep of 1 ps in a NVT ensemble, the system underwent a relaxation of only its atoms for 25 fs, with the lattice parameters fixed in a previous MD simulation. Then, after obtaining this relaxed system, another NVT simulation was performed for 150 ps in order to obtain all the required quantities
Both Wigner thermal conductivity and SM-RTA-BTE with normal mode decomposition were obtained using the code Dynaphopy, while the results of the third order BTE calculations were obtained with the code ALAMODE.

The AEMD thermal conductivity was obtained, as stated above, using two NVT simulations to heat the two parts of the simulation cell and one NVE simulations to let the system reach thermal equilibrium. All the simulations had 1 fs of timestep and, while the NVT runs had a fixed length of 20 ps, the NVE ones had a variable length, depending on the time needed to teach $\Delta T = 0$. Since thermal conductivity is very small, the simulation time needed had to be high, raging from 0.3 to 20 ns. These long simulation times in addition to the high number of atoms (117600 atoms in the largest systems) lead to an high computational cost, limiting the maximum length of the cell that can be simulated.

In particular, the surface convergence for the AEMD runs for the BTBT system was achieved with a 7×7 replica of the unit cell base and the L_z dimension was varied in a range between 10 and 60 nm, that correspond to a 10 to 50 replicas of the z direction of the unit cell.

In the right panel of Figure 5.1 is showed the κ convergence study at the variation of L_z for the BTBT system. Every value is calculated with via a configurational

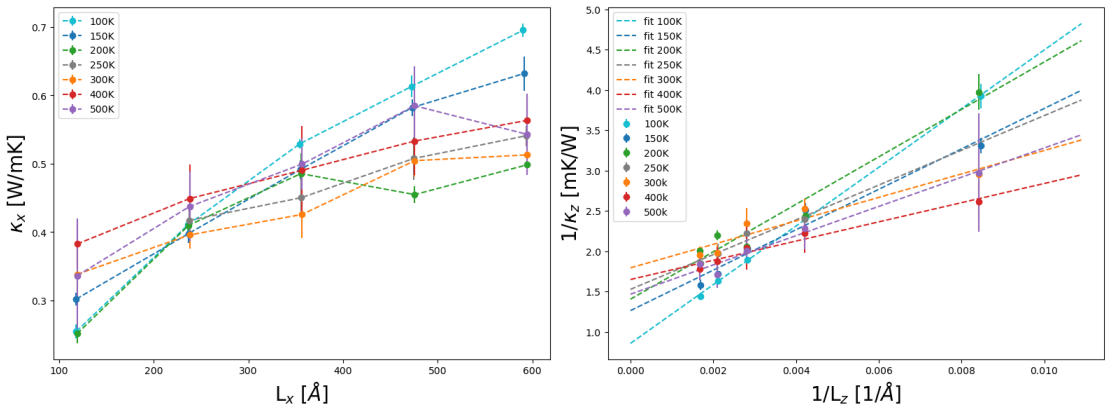

Figure 5.1: *Left: thermal conductivity of BTBT at various temperatures in function of the simulated cell length. Right:* $1/\kappa$ *in function of* $1/L$ *at different temperatures; the dotted lines are the linear fit from which* κ_∞ *is obtained.*

average of 5 statistically independents runs each with different initial atomic velocities.

The final value of thermal conductivity obtained for each temperature was extracted by the fit discussed above, showed in the left panel of Figure 5.1.
Similarly, for the DNTT system the surface convergence was achieve with a 7×7 replica of the unit cell and the L_z dimension was varied between 15 and 65 nm , that correspond to a 10 to 50 replicas of the z direction of the unit cell.

As for the BTBT systems, Figure 5.2 shows the process for obtaining the thermal

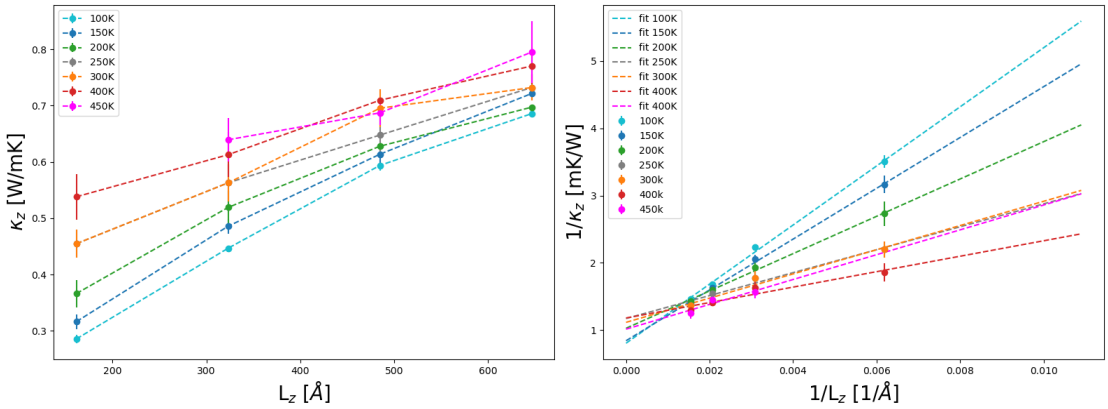

Figure 5.2: *Left: thermal conductivity of DNTT at various temperatures in function of the simulated cell length. Right:* $1/\kappa$ *in function of* $1/L$ *at different temperatures; the dotted lines are the linear fit from which* κ_∞ *is obtained.*

conductivity. The left panel shows the the dependence of κ from the system length and the right panel shows the linear relation of $\frac{1}{\kappa}$ and $\frac{1}{L_z}$, leading to the extraction of κ_∞ via linear fitting.

Finally, as stated above, the GAFF force field was employed in the MD simulations. This force field is a generalization of the harmonical AMBER one that aims to extend AMBER to organic and non-organic molecules and to be a complete force field. The General AMBER Force Field (GAFF) can describe well all the parameters of biologic and organic molecules by changing the AMBER function

form to:

$$E_{\text{pair}} = \sum_{\text{bonds}} K_r(r - r_{\text{eq}})^2 + \sum_{\text{angles}} K_\theta(\theta - \theta_{\text{eq}})^2 + \sum_{\text{dihedrals}} \frac{V_n}{2}[1 + \cos(n\phi - \gamma)] + \sum_{i<j} \left[\frac{A_{ij}}{R_{ij}^{12}} - \frac{B_{ij}}{R_{ij}^{6}} + \frac{q_i q_j}{\varepsilon R_{ij}} \right] \tag{5.1}$$

Furthermore, the GAFF uses a HF/6-31G* as charge method, while its parametrization for the van der Waals force is the same as the AMBER.

GAFF has been proved multiple times a good force field for describe organic systems and thus is a great potential for the description of both BTBT and DNTT [194].

5.2 Systems under study

BTBT is a π-conjugated molecular crystal containing two molecules per unit cell and belonging to the low-symmetry space group $P2_1/c$, visualized in Figure 5.3. The geometry was obtained by relaxing an experimental cell via MD simulations. Since the temperature dependence of phonon frequencies is vital to the understanding of thermal transport properties in this system, it is necessary to account the thermal expansion of the cell. In order to do so, the system was relaxed at different temperatures, showing differences on the order of 1% between 100 K and 300 K. The lattice constants and the cell angle are reported in Table 5.1. Although this may seem a little difference, since the system is strongly anharmonic it leads to macroscopic differences. The DNTT organic molecular crystal can be considered as a π-extended analogue of BTBT and thus it belongs to the same space group as the BTBT [195, 196]. The system obtained is showed at Figure 5.4. However, contrary to BTBT, DNTT transport does not depend on temperature [197], the unit cell of the system was optimized only at 0K, while the atomic position were

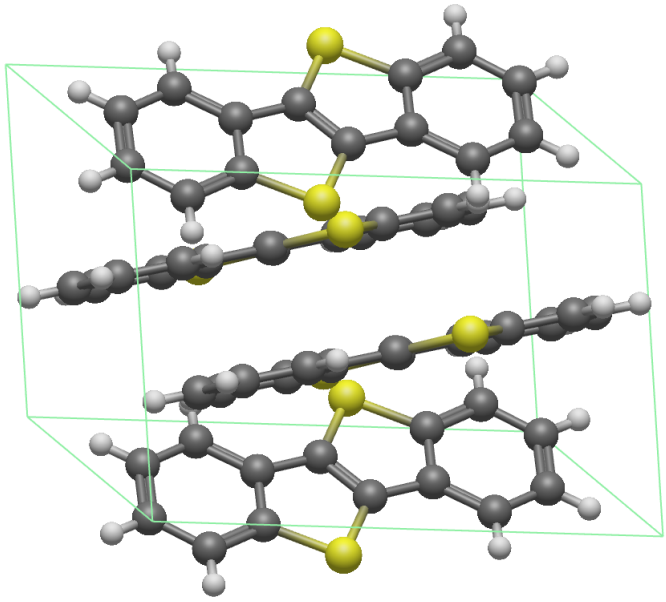

Figure 5.3: *Stick and balls representation of the BTBT unit cell.*

Table 5.1: *Lattice constants and cell angle of BTBT obtained via MD simulations at various temperature.*

Temp (K)	a (Å)	b (Å)	c (Å)	γ (°)
100	11.8892	5.8910	8.1111	106.50
150	11.8656	5.8851	8.0603	106.35
200	11.8427	5.8798	8.0099	106.21
250	11.8221	5.8757	7.9629	106.08
300	11.8040	5.8721	7.9215	105.97

optimized at every temperature. The obtained cell has the following parameters: $a = 6.1993$ Å, $b = 7.5442$ Å, $c = 16.1565$ Å.

5.3 Results and discussion

The first impact of anharmonicity in harmonic properties can be seen in the dispersion curves showed in Figure 5.5.

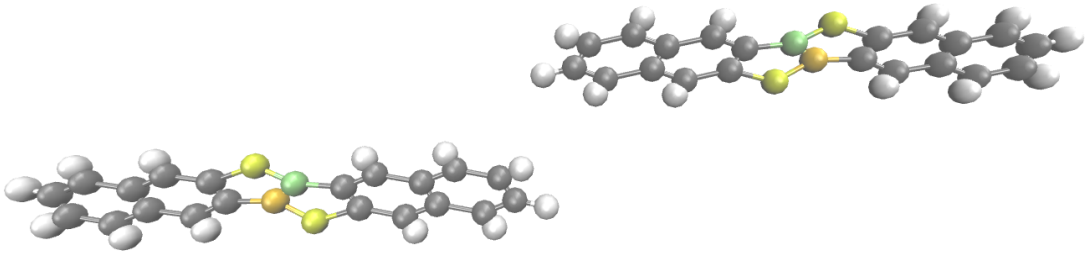

Figure 5.4: *Stick and balls representation of the DNTT unit cell.*

In Figure 5.5 a) are reported the dispersion curves of BTBT at 100 K and 300 K. Here we see how at different temperature the system show different behaviors, especially in the high-frequency regions. While the general shape is preserved, the system at 300 K shows slightly lower frequencies due to the thermal expansion. Moreover, it is possible to compare the harmonic phonon dispersion curves with the one obtained including the dependence on temperature. Such comparison is showed in Figure 5.5 b) for the systems at 100 K and 300 K. While the system at 100 K shows little variations, in the system at 300 K the differences are more pronounced. This suggest that the cause of this changes is indeed the anharmonicity of the system, since the anharmonicity becomes stronger with higher temperatures. For this reasons, it is possible to call the dispersion curves with temperature effects *quasi-harmonic phonon dispersion.*

Furthermore, an interesting fact emerges: the change in dispersion curves is not uniform for all frequencies. Thermal expansion alone only produces uniform red-shift in the frequencies, but this renormalization includes mode-depending frequency shifts. In detail, it is possible to see that the lower frequency curves are associated with intra-molecular modes and are only slightly affected by the renormalization, while higher frequencies branches are associated with inter-molecular modes and are more affected. Since BTBT molecules are bonded only via weak

π bonds, the resulting inter-molecular force constants are more affected by anharmonic effects.

Another proof of the strong anharmonicity of the system can be found by looking

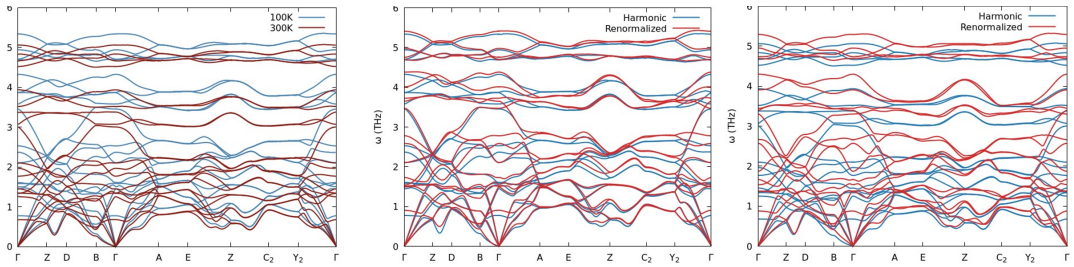

Figure 5.5: *a) Quasi-harmonic phonon dispersion of BTBT at 100 K and 300 K. b) Harmonic (blue) and renormalized (red) phonon dispersion curves at 100 K and 300 K.*

at their spectral energy density, reported in Figure 5.6.

As expected, at low temperature the band structure remains well defined, while as

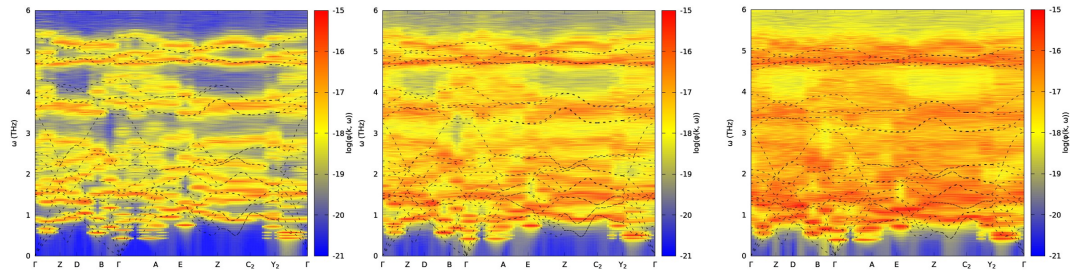

Figure 5.6: *Spectral energy density of BTBT at 100 K, 200 K and 300 K. The black dots represent the quasi-harmonic dispersion curves at the relative temperatures.*

the temperature increase the bands become hardly distinguishable. This is coherent with the results obtained in the dispersion curves: at non-zero temperatures the phonon mixing becomes important and affect the thermal properties of the material in conjunction with the thermal expansion.

Furthermore, we can analyze the cross correlation at Gamma point. In Figure 5.7 is reported the heat maps for BTBT correlations at various temperatures. The diagonal represents the auto-correlation, whereas the off-diagonal represents

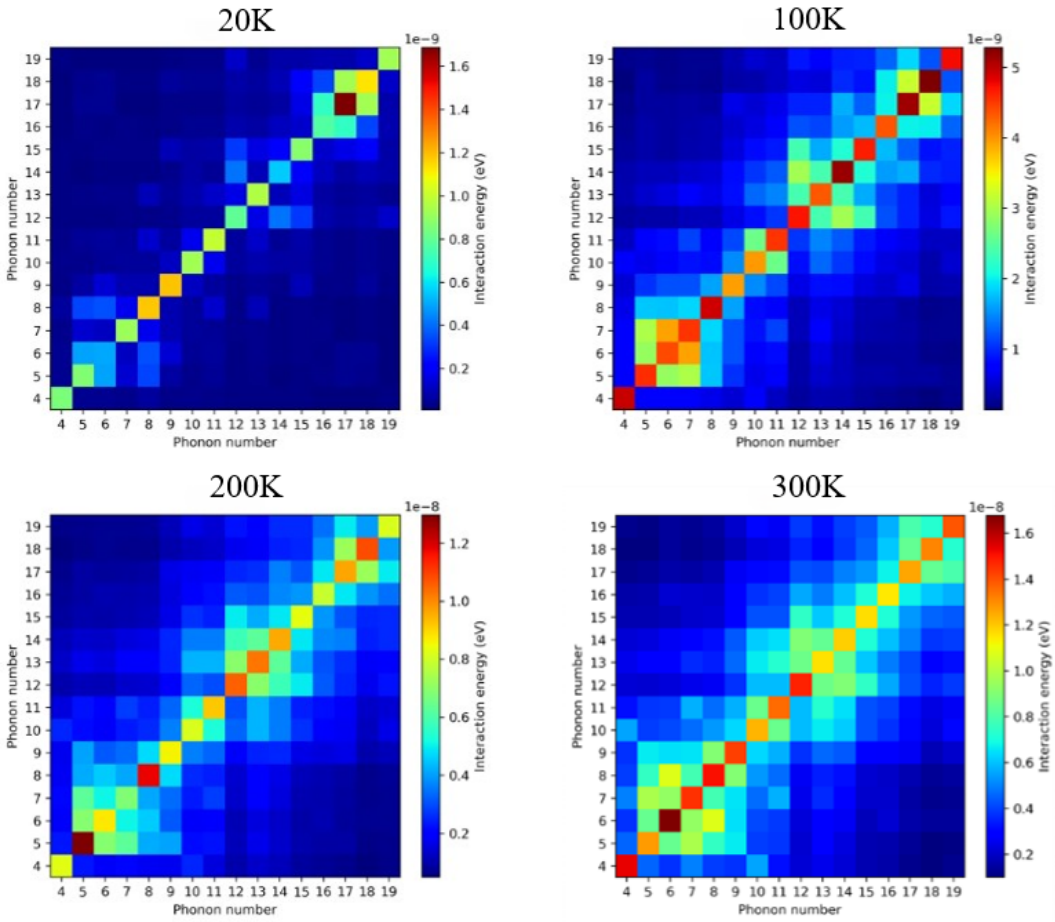

Figure 5.7: *Cross correlations of low-frequency modes of BTBT at 20, 100, 200 and 300 K.*

the cross-correlations. As expected, at low temperatures, i.e. 20 K, the cross-correlation is practically zero, describing a system without phonon mixing, as seen from the spectral energy density in Figure 5.6. As the temperature arises, the off-diagonal regions begin to have a non negligible value, describing the increased phonon mixing. This hints to an increasing importance of the wave-like term in phonon description with increasing temperature. Furthermore, this analysis showed the importance of anharmonicity in BTBT, thus the need to use a technique that is able to calculate inter-atomic force constants at high order of

anharmonicity. For this reason the four method discussed above are employed in calculating thermal conductivity.

In Figure 5.8 is reported the comparison between the thermal conductivity ob-

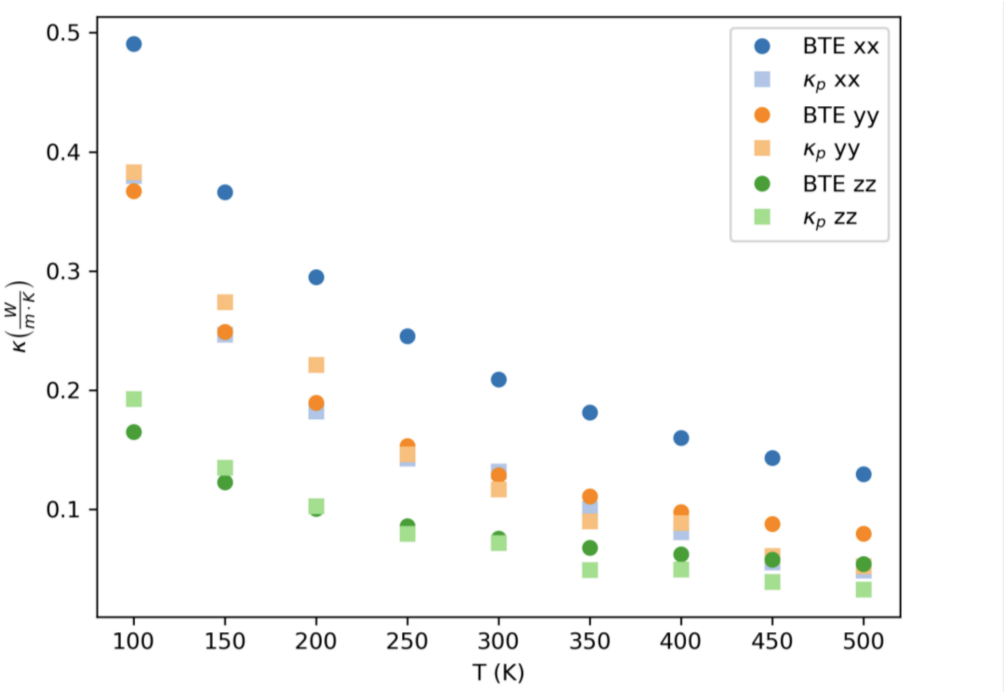

Figure 5.8: *Thermal conductivity in the inter-layer direction (xx) of BTBT. The green line is the BTE MD thermal conductivity, the blue line is the coherence term, the black line is the Wigner thermal conductivity and the red line is the AEMD thermal conductivity.*

tained with finite displacement BTE to the third order of anharmonicity and MD BTE that includes all order of anharmonicity for the three direction xx (inter-layer direction), yy and zz.

For the two intra-layer directions the results are compatible, showing how anharmonicity has a less impact in those directions, confirming the observations done while analyzing the dispersion curves.

In contrast, in the xx direction the values obtained with only the third order of anharmonicity are substantially different to the ones obtained through MD simulations with all orders of anharmonicity.

For this reason, combined with the fact that AEMD is a directional methodology that allows the estimation on thermal conductivity along only one direction at a time, only the results for the xx direction will be further discussed.

In Figure 5.9 are shown the thermal conductivities obtained using:

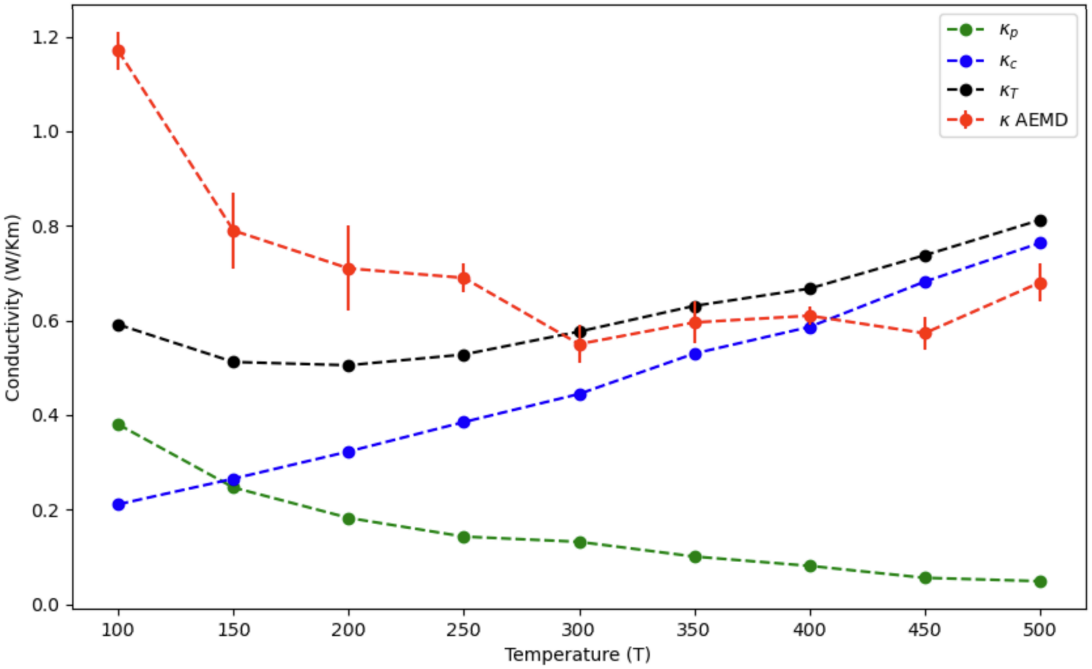

Figure 5.9: *Thermal conductivity in the interlayer direction (zz) of BTBT. The green line is the BTE MD thermal conductivity, the blue line is the coherence term, the black line is the Wigner thermal conductivity and the red line is the AEMD thermal conductivity.*

1. Wigner approach (black line);
2. SM-RTA-BTE approach obtained with MD simulations (green line);
3. coherence term (blue line);
4. AEMD approach (red line).

The only experimental measurement of BTBT inter-layer thermal conductivity is 0.63 ± 0.12 Wm^{-1}K^{-1} at 300 K is in perfect agreement with the calculated values

obtained with both the Wigner approach (0.60 $Wm^{-1}K^{-1}$) and the AEMD technique (0.56 $Wm^{-1}K^{-1}$).

Furthermore, the thermal conductivity obtained using Wigner approach shows an interesting fact: around 200 K the expected trend of $\kappa \sim 1/T$ is not observed. In fact, at high temperature the thermal conductivity is shown to have an higher value than the one at 100 K. The explanation of this can be found observing the trends of the two terms that compose the Wigner κ: the BTE and the coherence terms.

The BTE term strictly follows the $\kappa \sim 1/T$ term at every temperature, even when accounting all the anharmonicity orders. On the contrary, the coherence term increases almost linearly with the temperature. While at low temperatures the BTE term is predominant and therefore at low temperature the expected thermal conductivity trend is respected, rapidly the coherence term becomes predominant and leads the overall κ trend.

Moreover, the calculated BTE values largely underestimate the experimental thermal conductivity, showing how the anharmonicity alone, while it is important as shown before, can not fully explain the anomalous trend found in this systems.

Remarkably, the same anomalous trend is observed in the AEMD results. While the thermal conductivity values obtained at lower temperature are in net disagreement with the Wigner ones, after 300 K the two results become very similar. This discrepancy arises because AEMD employs the classical Dulong–Petit heat capacity, which is overestimated below room temperature (as Debye's temperature is approached) and therefore leads to an overestimation of the conductivity in this regime.

The similarity between the two trends at $T > 300$ K is interesting. The coherence therm that dictates the trend of Wigner thermal conductivity is composed by two types of effects: the first arises from quantum mechanic, such as tunnel effect, and

the second from the description of the phonon as both particle-like and wave-like. However, the first effect should not be present in the AEMD methodology, because it is a purely classical technique that theoretically should not be able to represent those effects. Perhaps, since the system studied is macroscopic, the quantum effects only have a minor impact in the overall thermal conductivity and can be considered negligible. On the contrary, since in the AEMD methodology at any point the assumption of phonon as the carrier of heat is made, the particle-like heat transport that is used in the BTE approach is never seen, thus never neglecting the wave-like terms. However, this point warrants further investigation.
The results obtained with the DNTT system confirms this unexpected similarity. In contrast to BTBT, DNTT does not show any difference in the shape of phonon dispersion curves at different temperatures, but shows the increase phonon mixing phenomenon with increasing temperature, as the BTBT does.

In Figure 5.10 the spectral energy density of DNTT is showed. Here we can see

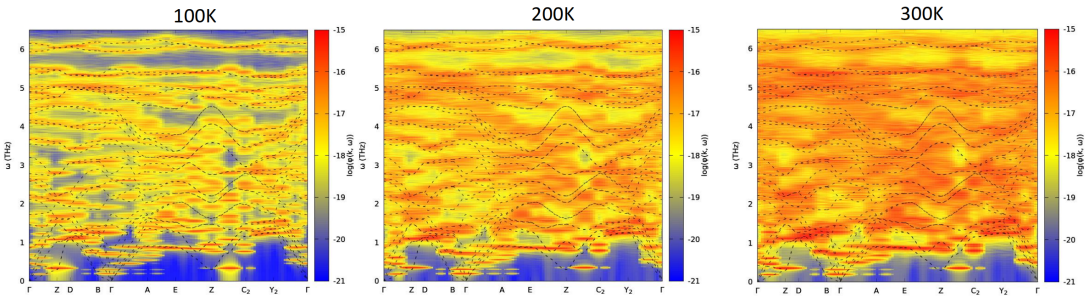

Figure 5.10: *Spectral energy density of DNTT at 100 K, 200 K and 300 K. The black dots represent the quasi-harmonic dispersion curves at the relative temperatures.*

how, similarly to BTBT, the systems at higher temperatures showed the blurring of bands characteristic of a system with high phonon mixing, while at low temperatures the dispersion curves are more defined.

In Figure 5.11 are shown the cross-correlation od the low-frequency modes of DNTT at Gamma point. In this system we can see how at 20 K, cross-correlation is practically absent, with the only non zero contribution being the auto-correlation

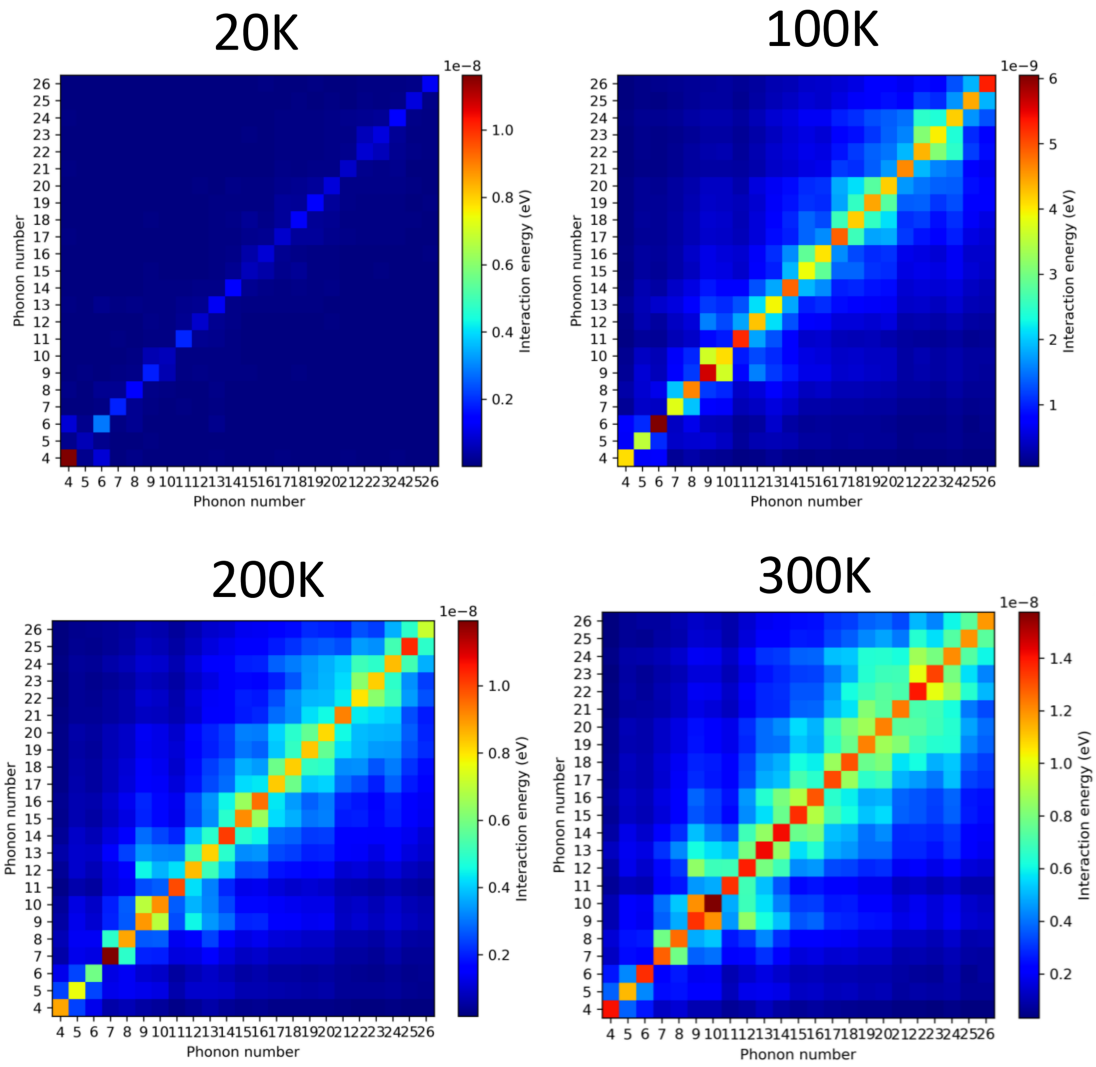

Figure 5.11: *Cross correlations of low-frequency modes of DNTT at 20, 100, 200 and 300 K.*

associated with low number phonons. As the temperature increases however, the cross correlation terms become more important, pointing towards the rise of phonon mixing, even if the process is slower than in the BTBT, with lower cross-correlation values at the same temperature. This hints that even in DNTT the wave-like phonon contribution is important, but it becomes predominant at higher temperatures than in the BTBT system.

In Figure 5.12 are shown the thermal conductivities obtained using:

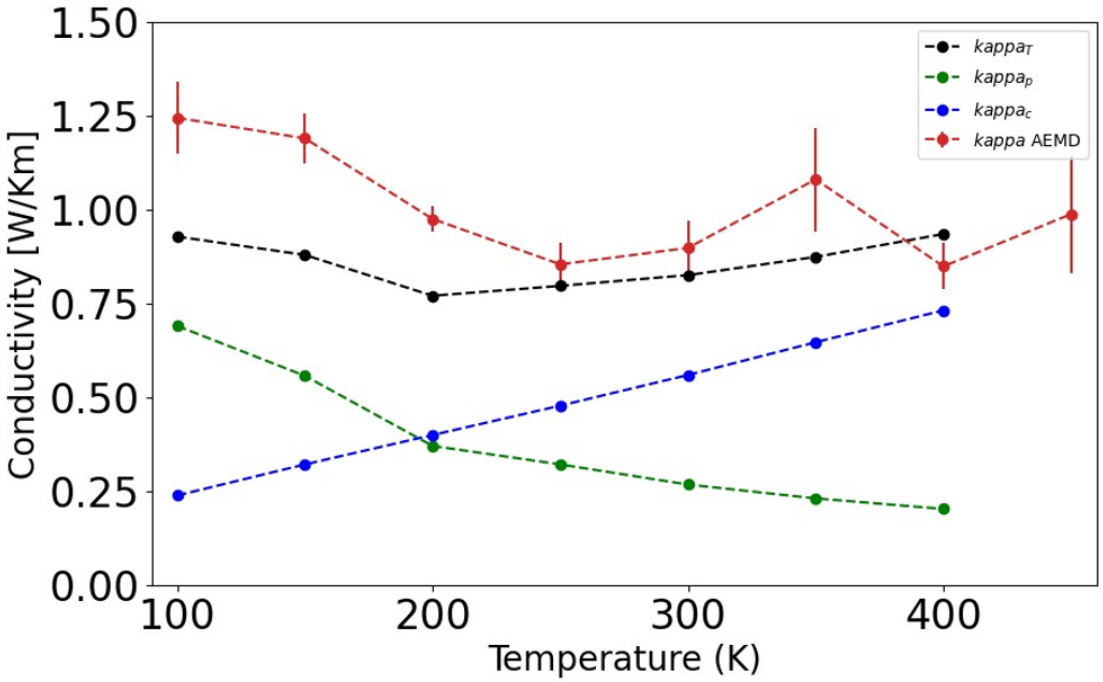

Figure 5.12: *Thermal conductivity in the inter-layer direction (zz) of DNTT. The green line is the BTE MD thermal conductivity, the blue line is the coherence term, the black line is the Wigner thermal conductivity and the red line is the AEMD thermal conductivity.*

1. Wigner approach (black line);
2. SM-RTA-BTE approach obtained with MD simulations (green line);
3. coherence term (blue line);
4. AEMD approach (red line).

In contrast to the BTBT system, here the third order BTE approach was not considered since we already proved for the BTBT system how the BTE with MD simulations gives results more in line with the experiment.
By analyzing the κ obtained with the Wigner approach, we can find the same inversion of the 1/T trend that is expected in the BTE approach. Although, in the

DNTT system the inversion is at ~ 200 K, an higher temperature than the BTBT system. In fact, by looking at the BTE and coherence contributions, it is possible to notice how the BTE remains predominant until ~ 200 K, temperature at which the coherence term give the same contribution as the BTE one, and at higher temperatures the coherence term becomes predominant. Once again, the AEMD approach gives results similar to the ones obtained with the Wigner methodology, if we account the overestimation of low temperature values resulting from the Dulong-Petit heat capacity. Aside from that, them AEMD thermal conductivity shows the same trend inversion as the Wigner approach.

In summary, this chapter showed how the BTE approach, both at the third order and at any order of anharmonicity, fails to describe system with packed phonon dispersion curves, because it fail to account the phonon mixing phenomenon. However, this systems are well described by both the Wigner and the AEMD approaches, that surprisingly give similar results.
The main difference between the BTE and the Wigner approach is that the BTE formalism relies heavily on the quasi-particle approximation. During the development of the Boltzmann Transport Equation, phonons are defined as a Bose-Einstein gas and all the thermal properties are derived using this assumption. In contrast, in the Wigner formalism this particle-like behavior coexist with the wave-like one, resulting in a more comprehensive description of phonon propagation. In most crystalline solids, the wave-like nature of the phonon is not the dominating factor in thermal transport, and the BTE approach with the correct order of anharmonicity is enough to give an accurate description of its thermal properties [143]. Although, in some crystals, like BTBT and DNTT, the particle-like contribution il small enough that the wave-like term becomes predominant, thus the anomalous thermal conductivity trend here analyzed.

In contrast, the AEMD method is based on the phenomenological Fourier Law, that only describes macroscopic quantities. Thus, the particle-like behavior of phonons present in the BTE approximation is never introduced in AEMD, making this methodology not limited by the BTE limits. So, while the AEMD do not give any information of the microscopical quantities such as phonon group velocity or dispersion curves, its prediction of thermal conductivity has a more general nature and is able to describe both crystalline and non-crystalline materials. However, AEMD is still limited by a number of factors, such a the heat capacity calculation, that can result into the numerical discrepancies found when comparing to the Wigner approach.

Chapter 6

Conclusions

In this thesis we have analyzed the thermal properties of various materials in order to extrapolate some strategies that can help the development of new thermoelectric materials.

Thermoelectricity is the physical phenomenon that enables the direct conversion of heat into electrical energy, allowing the generation of an electric current from a temperature gradient. This type of energy generations can be used both as primary electricity generation method and as a secondary generator. While the first is optimal in applications where the durability of the generator in a major concern, like in deep-space missions or as a battery for pacemaker, the second has a wider array of applications, allowing the recycling of the wasted heat produced by the primary generator.

Despite its many advantages, the thermoelectric generators are not widely adopted because of their generically low efficiency, that is much lower than other types of generators.

Typically, the dimensionless figure of merit (zT) is used as an indicator pf the performance of a material as a thermoelectric generator. The typical figure of merit of a pristine material has a value ~ 1, while other types of energy generators often

surpass $zT \sim 20$.

More precisely, the zT depends directly from the electrical properties of the material (i.e. electrical conductivity and squared Seebeck coefficient) and inversely from its thermal conductivity. Since often a material that shows high electrical conductivity posses a equally high thermal conductivity, modifications to the pristine materials are needed to further develop this subject.

Among all possible materials with thermoelectric applications, 2D and organic semiconductors have emerged as particularly promising candidates for thermoelectric applications.

2D materials are of particular interest because they undergo a peculiar change in all their properties when transitioning from bulk to single layer or when changing their stacking type. Moreover, they are easily functionalized by the addition of side-chains between their layer, permitting the creation of organic-inorganic hybrid structures that can further boost their performance as thermoelectric generators. Furthermore, they have shown great value in other type of applications after the incorporation of defects, a strategy that could be beneficial for thermoelectric applications as well.

Organic semiconductors, especially the one composed by small molecules that give form to the class of organic molecular crystals are equally interesting because of their high anharmonic conduction. This behavior, if treated accordingly, can offer valuable insights on thermal conduction and can lead to the creation of anharmonic materials that artificially decrease their thermal conductivity through anharmonic scattering.

In this thesis were analyzed four different materials, TaS_2 and Mos_2, two compounds belonging to the class of transition metal dichalcogenoids, a particularly interesting type of 2D material, BTBT and DNTT, two organic molecular crystals with peculiarly high anharmonicity.

To perform those investigation computational methods were employed.
Firstly, the finite displacements methodology, a method that uses the forces generated from small atomic displacements to extrapolate the interatomic force constants and calculate the dynamical matrix, from which it is possible to obtain all microscopical thermal transport properties in the Boltzmann Transport Equation approximation. These displacements can be simulated using ab-initio DFT calculations, molecular dynamics or mode decomposition techniques, where the fist excel in reliability, the second is faster and still sufficiently accurate and the third allows the calculation of high order of anharmonicity.
The second method is the approach to equilibrium molecular dynamics. This classical technique solves the macroscopic Fourier law, giving accurate results of the macroscopic thermal properties of a material but forgoing the microscopic description obtained with the first method. This methodology is particularly robust and allow the prediction of thermal properties of non-crystalline materials, such as defected crystals, a field where the BTE approximation tends to fail and where the computational cost of the finite displacement method would be overwhelmingly high. In this technique a heat gradient is applied to the simulation cell and then the system is brought to thermal equilibrium through NVT molecular dynamics simulations. From the trend of the temperature difference throughout the NVT run the thermal conductivity can be extrapolated.
The third method is the Wigner approach to thermal conduction. This methodology expands the BTE formulation adding some wave-like phenomena that the phonon theory forgo. These new terms allow the description of material with high cross correlation, like glasses or insulator for which the BTE alone is not sufficient to give a comprehensive explanation of thermal transport.
All three methods have their strength and their weakness: the BTE give precise microscopic results at any order of anharmonicity while the Wigner approach is

more computational expensive but manage to predict the behavior of certain materials better than the BTE, while the opposite is also true in some cases. Finally, AEMD give a macroscopic description of the materials, trading the microscopic information for speed of result acquisition and generality.

For both TaS_2 and MoS_2 the finite displacement methodology with ab-initio DFT calculations revealed the presence of low frequency optical phonon dispersion modes, called quasi-acoustic branches, that play a pivotal role in thermal conductivity. These modes are caused by the vibration between two adjacent layers, thus are not present in the mono-layer phase of a TMD.
However, their contribution in the bulk phase is not consistent. In fact, they give two opposing contribution:

- an increase of the possible phonon scattering channels that leads to an increase in anharmonicity and to a decrease in phonon lifetime, decreasing the resulting thermal conductivity;

- an increase of vibrational modes with non negligible group velocity and phonon lifetime, resulting in an increase of thermal conductivity.

Those two phenomena give different contribution in different systems, sometimes leading to an increase of thermal conductivity, sometimes to a decrease of it.
Unfortunately, while different stacking types leads to a change of the contribution of quasi-acoustic modes to thermal conductivity, the stacking type does not seem directly connected to the entity of this contribution, as per the analysis proposed in this thesis. In fact, while in the TaS_2 with 2H-AA' stacking the quasi-acoustic branches are responsible to almost an half of the total thermal conductivity, practically leading to a doubling of the thermal conductivity of the mono-layer system,

in the MoS_2 with 2H-AA' stacking the quasi-acoustic branches give a slight negative contribution, resulting in a thermal conductivity of the bulk material smaller than the one of the mono-layer phase at low temperature. Meanwhile in the 2H-AB phase of MoS_2 the contribution of quasi-acoustic branches is reminiscent of the one in TaS_2, resulting in a great increase in the thermal conductivity of the system.

While stacking type does not seem to be the discerning factor between a positive and a negative contribution of quasi-acoustic modes to thermal conductivity, a possible discerning factor could be the distancing between layers. In fact, the inter-layer distancing between two sulfur atoms in 2H-AA' TaS_2 (3.58 Å) is similar to the one in 2H-AB MoS_2 (3.37 Å) while the one in 2H-AA' MoS_2 is substantially higher (3.96 Å).

Since the interactions between the layers are dominated by van der Waals forces, the distance between two adjacent layers plays a primary role in determining the scope of such interactions, so it is possible that the difference discussed above is the main responsible to the different behavior of quasi-acoustic modes.

Moreover, the same two systems were investigated after the introduction of different modifications.

In the bulk TaS_2 some organic side-chains were introduced, namely tert-butyl isocianate, and the effects of such functionalization were discussed. Not only the side-chains act as a layer separator, increasing the layer separation and transitioning the TaS_2 in a condition of near mono-layer, but they provide additional phonon dispersion curves at low frequency, derived from molecular vibrations. These modes have almost zero group velocity and phonon lifetimes, thus they can be considered fully optical since the quasi-acoustic modes are characterized by an high group velocity with a value comparable to the acoustic one. These low frequency optical modes cross the acoustic modes and as a result of this crossing

decrease both the acoustic phonon lifetimes, by increasing the number of possible scattering channels, and the acoustic phonon group velocity. This combination of harmonic and anharmonic effects lead to a huge reduction in the in-plane thermal conductivity.

In summary, it is possible to say that the functionalization is an effective method to increase a 2D material figure of merit by decreasing its thermal conductivity without affecting its electrical properties and it is a viable technique to create novel thermoelectric generators with transition metal dichalgoneoids.

In the mono-layer MoS_2 was performed a further study using the AEMD method to analyze the effect of sulfur vacancies in the system. The sulfur atoms were only removed from the top sulfur layer of the material, in order to simulate an experimental etching process. Firstly, the vacancies were introduced following a random distribution, creating a number of point vacancies with a certain density. Then, using the same densities of the random systems, materials with ordered strips of vacancies were realized.

The systems with random point vacancies all showed a great decrease in thermal conductivity, while the effects of the ordered strips were more complex.

Firstly, it is possible to notice how the systems with random point vacancies have lower thermal conductivity in confront of the systems with ordered vacancies in almost all the defect density examined. Thus, for a thermoelectric prospective, etching a system with random point vacancies is a more effective way to obtain a good thermoelectric material.

However, the difference between the two distribution methods are more profound than just the reduction in thermal conductivity. Notably, while the decrease obtained through random point vacancies directly depends on the density of the vacancies, the reduction obtained in systems with ordered strips shows more dependence on the number of defect lines than in the density of vacancies. The most

notable effect is observed for two strips of vacancies, were the thermal conductivity of the systems, independently of the density of vacancies, becomes almost equal to the one of the pristine MoS_2 mono-layer.

This phenomenon seems dependent not only by the number of strips, but even on their separation. In fact, it is show how by taking a system with two strips and reducing their distance we obtain a reduction in thermal conductivity even before they merge into one strip. Similarly, it is possible to take a system with four strips and decrease their separation and it is shown that the thermal conductivity of the system slowly increase to the value of the two strips system, even before the four strips are merged into two.

This effect is demonstrated the result of an harmonic modification of the system. In systems with $n_S \neq 2$, some low frequency optical modes are found that, similarly to the molecular modes in functionalized TaS_2, cross with the acoustic branches and effectively reduce the group velocity of the system, resulting in a decrease of thermal conductivity. In contrast, in both the pristine mono-layer MoS_2 and the system with two strips of vacancies these optical modes are not present, resulting in the same thermal conductivity value.

Unfortunately, the super periodicity here discovered hinders the applications of defected MoS_2 in the thermoelectric field. Notably, the best way to use MoS_2 as a thermoelectric generator is the system with random point vacancies. However, other applications, such as MoS_2 transistors, require an efficient heat dissipation method, thus a high value of thermal conductivity, making the system with two strips of vacancies a prime candidate for these type of applications.

Furthermore, in both the TaS_2 and MoS_2 studies the two methodologies AEMD and finite displacements with the BTE approximation at the third order od anharmonicity were proven sufficient for the reproduction of experimental results and therefore the analysis of the TMD class of materials.

However, depending on the system, a deeper level of theory is needed, as demonstrated in the third analysis proposed.

The BTBT and the DNTT systems are organic molecular crystals with high anharmonicity that is a perfect testing ground for a prediction method. For this reason the system was analyzed with both BTE at third order anharmonicity, BTE at any order of anharmonicity, AEMD and Wigner approach to thermal conductivity. In these highly anharmonical organic crystals the shortcomings of the BTE method were shown. Notably, it was shown how the third order of anharmonicity, while it gives sufficiently accurate results in systems with less anharmonicity, such as the TMDs seen before, greatly fails in the description of more complex materials such as BTBT. Indeed, by calculating the thermal conductivity using the mode decomposition technique, thus calculating the BTE thermal conductivity an a infinite order of anharmonicity, a great difference in the κ value is found.

Unfortunately, in the BTBT and DNTT systems only accounting for the high anharmonicity is not enough to correctly describe the thermal transport process. As a matter of fact, the BTBT thermal conduction is dominated by some phonon process that are not predicted in the BTE methodology, such as the phonon mixing derived from the wave-like nature of phonons.

As discussed above, the particle-like description of phonon is not enough to fully describe the system, but indeed it gives a important contribution to the total thermal conductivity, especially at low temperatures. Thus, in this system, the Wigner approach is necessary to obtain a realistic value of thermal conductivity. This methodology combine the particle-like description provided in the BTE approach with a coherence term that accounts the wave-like properties of the phonon. The necessity of this description can be discerned from the spectral energy density of the system. It is possible to notice that as the system increase its temperature, the spectral energy density increase accordingly making the phonon dispersion

curves hardly distinguishable. This is a sign of high phonon cross-correlation in the system that leads to the phonon mixing phenomenon.

Surprisingly, the AEMD method gives results similar to the Wigner approach. Theoretically specking, the Wigner methodology add some purely quantum effects ate the BTE description of thermal transport. In contrast, the AEMD is a purely classical approach based on the classical Fourier law. Even when using the classical Dulong-Petit heat capacity, that effectively give some overestimate results at low temperature, the overall trend of thermal conductivity is remarkably similar to the one predicted by the the Wigner approach and the two value are within the statistical error of the AEMD results.

This coincidence in thermal conductivity value is truly surprising and has been never seen before, thus it is worth further investigations. Nonetheless, an intuitive explanation can be given.

Firstly, let's clarify that the Fourier Law have an empirical nature that addresses only macroscopic quantities, while the Wiger approach is a theoretical formulation based on microscopic quantities.

When the BTE formalism and the phonon theory was proposed, they relied upon some heavy approximations that were considered accurate for crystalline materials, such as the quasi-particle nature of phonons. While these approximations are indeed sound when examining most crystalline systems, as demonstrated by the calculations in both TMD materials, the analysis on both BTBT and DNTT proved that even among the crystalline materials there are some form which the BTE formalism is not enough to describe the system. As can be observed comparing the BTE and coherence contributions to the thermal conductivity with the dispersion curves at the same temperature, at low temperatures, when the phonon mixing phenomenon is not present, the coherence term dominates the thermal conductivity, while at higher temperatures, when the phonon mixing becomes relevant,

the coherence term becomes the dominant one. This indicates that the Wigner approach,and so the contributions due to the wave-like behavior of phonons, is relevant not only for amorphous and glassy materials, but even for crystalline materials with low separation between phonon dispersion curves. In these cases, to describe the microscopical behavior of the system is necessary to account for both particle-like and wave-like properties of the phonon. A further proof of this can be found in [143], were they show that in a peculiar crystalline perovskite the Wigner and the BTE formalism at the same level of anharmonicity give approximately the same results, explaining how in crystalline systems with no phonon mixing the BTE and the Wigner approach are almost equivalent.
However, AEMD describes the system only in a macroscopic term, without ever introducing the phonon formalism and neither the quasi-particle approximation for lattice vibration. Thus, it stand to reason that its prediction capabilities are not limited from the BTE limits and that it is capable to give correct thermal conductivity estimation even in materials where the BTE fails. Of course, the AEMD has more limitations, since it is only capable of describing macroscopic quantities like thermal conductivity and can not give any information of the microscopic details of thermal transport.

In summary, this thesis have provided some new perspectives in the study of materials for thermoelectric applications. The ab-initio simulations provided a deeper understanding on the microscopic mechanism governing thermal conductivity in both 2D materials and highly anharmonical crystals, while the AEMD simulations provided accurate predictions of thermal conductivity values in both crystalline and non-crystalline systems.

The functionalization of a 2D material with an organic side-chain was demonstrated as a beneficial approach to improve a compound thermoelectric performances and, while this phenomenon was analyze for a single system with a particular side-chain, future studies can be performed to generalize the results, in particular by changing the length of the side-chain and by functionalizing materials with different bulk properties.

While the ordered strips of vacancies were not beneficial for thermoelectric applications, the superperiodicity that is found in the systems with 2 strips is an important result for other types of applications. While the random distribution of point vacancies seems like the most beneficial approach to decrease thermal conductivity and so increase the material figure of merit, future analysis using different vacancies distributions are possible, allowing for further improvements on the figure of merit of defected materials.

Lastly, the accuracy of the AEMD was proved, even in materials were the standard BTE approach fails and more advanced techniques that rely on quantum mechanics are needed. Unfortunately, the reason behind this accuracy is still largely unknown and a satisfying explanation is still needed. However, this broadens the range of applications of the AEMD method and offer a novel, precise and with a limited computational cost approach for the evaluation of thermal conductivity in complex materials.

Bibliography

[1] D. Beretta, N. Neophytou, J. M. Hodges, M. G. Kanatzidis, D. Narducci, M. Martin-Gonzalez, M. Beekman, B. Balke, G. Cerretti, W. Tremel, et al. "Thermoelectrics: From history, a window to the future". In: *Materials Science and Engineering: R: Reports* 138 (2019), p. 100501.

[2] M. Piccolino. "Luigi Galvani and animal electricity: two centuries after the foundation of electrophysiology". In: *Trends in neurosciences* 20.10 (1997), pp. 443–448.

[3] A. Volta, A. nazionale dei Lincei, and M. R. Istituto lombardo di scienze e lettere. *Le opere di Alessandro Volta*. Le opere di Alessandro Volta v. 1. Hoepli, 1918. URL: https://books.google.it/books?id=Cbc5AQAAMAAJ.

[4] M. Piccolino. "Animal electricity and the birth of electrophysiology: the legacy of Luigi Galvani". In: *Brain research bulletin* 46.5 (1998), pp. 381–407.

[5] Oersted. "Notiz von neuen electrisch-magnetischen Versuchen des Herrn Seebeck in Berlin". In: *Annalen der Physik* 73.4 (1823), pp. 430–432.

[6] T. J. Seebeck. *Magnetische polarisation der metalle und erze durch temperatur-differenz*. Vol. 70. Engelmann, 1895.

[7] H. C. Oersted. "On electro-magnetism". In: *Annals of Philosophy* 2 (1821), pp. 321–337.

[8] P. M. Roget. *Electricity, Galvanism, Magnetism and Electro-Magnetism by PM Roget*. Robert Baldwin, 1831.

[9] J. Peltier. "Investigation of the heat developed by electric currents in homogeneous materials and at the junction of two different conductors". In: *Ann. Chim. Phys* 56.1834 (1834), p. 371.

[10] E. Lenz. "Einige versuche im gebiete des galvanismus". In: *Annalen der Physik* 120.6 (1838), pp. 342–349.

[11] D. M. Rowe. *Thermoelectrics handbook: macro to nano*. CRC press, 2005.

[12] L. Rayleigh. "XLIII. On the thermodynamic efficiency of the thermopile". In: *The London, Edinburgh, and Dublin Philosophical Magazine and Journal of Science* 20.125 (1885), pp. 361–363.

[13] R. Kennedy. *Electrical Installations of electric light, power, traction and industrial electrical machinery*. Vol. 4. Jack, 1903.

[14] E. Altenkirch. "Elektrothermische Kälteerzeugung und reversible elektrische Heizung". In: *Physikalische Zeitschrift* 12 (1911), pp. 920–924.

[15] A. F. Ioffe, L. Stil'Bans, E. Iordanishvili, T. Stavitskaya, A. Gelbtuch, and G. Vineyard. "Semiconductor thermoelements and thermoelectric cooling". In: *Physics Today* 12.5 (1959), pp. 42–42.

[16] A. Dadhich, M. Saminathan, K. Kumari, S. Perumal, M. S. Ramachandra Rao, and K. Sethupathi. "Physics and technology of thermoelectric materials and devices". In: *Journal of Physics D: Applied Physics* 56.33 (May 2023), p. 333001. DOI: 10.1088/1361-6463/acc9d0. URL: https://doi.org/10.1088/1361-6463/acc9d0.

[17] M. Telkes. "The Efficiency of Thermoelectric Generators. I." In: *Journal of Applied Physics* 18.12 (1947), pp. 1116–1127.

[18] M. Vedernikov and E. Iordanishvili. «AF Ioffe and origin of modern semiconductor thermoelectric energy conversion». In: *Seventeenth International Conference on Thermoelectrics. Proceedings ICT98 (Cat. No. 98TH8365)*. IEEE. 1998, pp. 37–42.

[19] H. Goldsmid and R. Douglas. "The use of semiconductors in thermoelectric refrigeration". In: *British Journal of Applied Physics* 5.11 (1954), p. 386.

[20] B. Blanke, J. Birden, K. Jordan, and E. Murphy. *Nuclear battery-thermocouple type summary report*. Tech. rep. Mound Plant (MOUND), Miamisburg, OH (United States), 1960.

[21] L. D. Hicks and M. S. Dresselhaus. "Thermoelectric figure of merit of a one-dimensional conductor". In: *Physical review B* 47.24 (1993), p. 16631.

[22] D. M. Rowe. *CRC handbook of thermoelectrics*. CRC press, 1995.

[23] C. B. Vining. "An inconvenient truth about thermoelectrics". In: *Nature materials* 8.2 (2009), pp. 83–85.

[24] A. Shakouri. "Recent developments in semiconductor thermoelectric physics and materials". In: *Annual review of materials research* 41.1 (2011), pp. 399–431.

[25] D. Meadows and J. Randers. *The limits to growth: the 30-year update*. Routledge, 2012.

[26] H. Bottner, J. Nurnus, A. Schubert, and F. Volkert. «New high density micro structured thermogenerators for stand alone sensor systems». In: *2007 26th International Conference on Thermoelectrics*. IEEE. 2007, pp. 306–309.

[27] D. Beretta, M. Massetti, G. Lanzani, and M. Caironi. "Thermoelectric characterization of flexible micro-thermoelectric generators". In: *Review of scientific Instruments* 88.1 (2017).

[28] J. P. Heremans, M. S. Dresselhaus, L. E. Bell, and D. T. Morelli. "When thermoelectrics reached the nanoscale". In: *Nature nanotechnology* 8.7 (2013), pp. 471–473.

[29] S. Manzeli, D. Ovchinnikov, D. Pasquier, O. V. Yazyev, and A. Kis. "2D transition metal dichalcogenides". In: *Nature Reviews Materials* 2.8 (2017), pp. 1–15.

[30] A. K. Kushwaha, H. Kalita, S. Suman, A. Bhardwaj, and R. Ghosh. «Two-dimensional (2D) thermoelectric materials». In: *Thermoelectricity and advanced thermoelectric materials*. Elsevier, 2021, pp. 233–260.

[31] A. Splendiani, L. Sun, Y. Zhang, T. Li, J. Kim, C.-Y. Chim, G. Galli, and F. Wang. "Emerging photoluminescence in monolayer MoS2". In: *Nano letters* 10.4 (2010), pp. 1271–1275.

[32] K. F. Mak, C. Lee, J. Hone, J. Shan, and T. F. Heinz. "Atomically thin MoS 2: a new direct-gap semiconductor". In: *Physical review letters* 105.13 (2010), p. 136805.

[33] B. Radisavljevic, A. Radenovic, J. Brivio, V. Giacometti, and A. Kis. "Single-layer MoS2 transistors". In: *Nature nanotechnology* 6.3 (2011), pp. 147–150.

[34] R. G. Dickinson and L. Pauling. "The crystal structure of molybdenite". In: *Journal of the American Chemical Society* 45.6 (1923), pp. 1466–1471.

[35] J. A. Wilson and A. Yoffe. "The transition metal dichalcogenides discussion and interpretation of the observed optical, electrical and structural properties". In: *Advances in Physics* 18.73 (1969), pp. 193–335.

[36] R. Frindt and A. Yoffe. "Physical properties of layer structures: optical properties and photoconductivity of thin crystals of molybdenum disulphide". In: *Proceedings of the Royal Society of London. Series A. Mathematical and Physical Sciences* 273.1352 (1963), pp. 69–83.

[37] P. Joensen, R. Frindt, and S. R. Morrison. "Single-layer mos2". In: *Materials research bulletin* 21.4 (1986), pp. 457–461.

[38] R. Tenne, L. Margulis, M. e. Genut, and G. Hodes. "Polyhedral and cylindrical structures of tungsten disulphide". In: *Nature* 360.6403 (1992), pp. 444–446.

[39] Y. Feldman, E. Wasserman, D. Srolovitz, and R. Tenne. "High-rate, gas-phase growth of MoS2 nested inorganic fullerenes and nanotubes". In: *Science* 267.5195 (1995), pp. 222–225.

[40] V. Shanmugam, R. A. Mensah, K. Babu, S. Gawusu, A. Chanda, Y. Tu, R. E. Neisiany, M. Försth, G. Sas, and O. Das. "A review of the synthesis, properties, and applications of 2D materials". In: *Particle & Particle Systems Characterization* 39.6 (2022), p. 2200031.

[41] E. Marseglia. "Transition metal dichalcogenides and their intercalates". In: *International reviews in physical chemistry* 3.2 (1983), pp. 177–216.

[42] X. Wen, Z. Gong, and D. Li. "Nonlinear optics of two-dimensional transition metal dichalcogenides". In: *InfoMat* 1.3 (2019), pp. 317–337.

[43] M. M. Perera, M.-W. Lin, H.-J. Chuang, B. P. Chamlagain, C. Wang, X. Tan, M. M.-C. Cheng, D. Tománek, and Z. Zhou. "Improved carrier mobility in few-layer MoS2 field-effect transistors with ionic-liquid gating". In: *ACS nano* 7.5 (2013), pp. 4449–4458.

[44] J. Kumar, M. A. Kuroda, M. Z. Bellus, S.-J. Han, and H.-Y. Chiu. "Full-range electrical characteristics of WS2 transistors". In: *Applied Physics Letters* 106.12 (2015).

[45] R. Lieth and J. Terhell. «Transition metal dichalcogenides». In: *Preparation and crystal growth of materials with layered structures*. Springer, 1977, pp. 141–223.

[46] T. Hu, R. Li, and J. Dong. "A new (2 × 1) dimerized structure of monolayer 1T-molybdenum disulfide, studied from first principles calculations". In: *The Journal of Chemical Physics* 139.17 (Nov. 2013), p. 174702. ISSN: 0021-9606. DOI: 10.1063/1.4827082. eprint: https://pubs.aip.org/aip/jcp/article-pdf/doi/10.1063/1.

4827082/15468638/174702_1_online.pdf. URL: https://doi.org/10.1063/1.4827082.

[47] C.-H. Lee, E. Silva, L. Calderín, T. Nguyen Minh, M. Hollander, B. Bersch, T. Mallouk, and J. Robinson. "Tungsten Ditelluride: A layered semimetal". In: *Scientific reports* 5 (June 2015), p. 10013. DOI: 10.1038/srep10013.

[48] P. Lazar, J. Martincová, and M. Otyepka. "Structure, dynamical stability, and electronic properties of phases in TaS 2 from a high-level quantum mechanical calculation". In: *Physical Review B* 92.22 (2015), p. 224104.

[49] A. Kuc, N. Zibouche, and T. Heine. "Influence of quantum confinement on the electronic structure of the transition metal sulfide TS 2". In: *Physical Review B—Condensed Matter and Materials Physics* 83.24 (2011), p. 245213.

[50] H. Schäfer. *Chemical transport reactions*. Elsevier, 2013.

[51] R. Frindt. "Single crystals of MoS2 several molecular layers thick". In: *Journal of Applied Physics* 37.4 (1966), pp. 1928–1929.

[52] N. Huo, Z. Wei, X. Meng, J. Kang, F. Wu, S.-S. Li, S.-H. Wei, and J. Li. "Interlayer coupling and optoelectronic properties of ultrathin two-dimensional heterostructures based on graphene, MoS 2 and WS 2". In: *Journal of Materials Chemistry C* 3.21 (2015), pp. 5467–5473.

[53] S. Bertolazzi, J. Brivio, and A. Kis. "Stretching and breaking of ultrathin MoS2". In: *ACS nano* 5.12 (2011), pp. 9703–9709.

[54] Q. Li, J. Newberg, E. Walter, J. Hemminger, and R. Penner. "Polycrystalline molybdenum disulfide (2H- MoS2) nano-and microribbons by electrochemical/chemical synthesis". In: *Nano Letters* 4.2 (2004), pp. 277–281.

[55] R. Ganatra and Q. Zhang. "Few-layer MoS2: a promising layered semiconductor". In: *ACS nano* 8.5 (2014), pp. 4074–4099.

[56] G. Eda, H. Yamaguchi, D. Voiry, T. Fujita, M. Chen, and M. Chhowalla. "Photoluminescence from chemically exfoliated MoS2". In: *Nano letters* 11.12 (2011), pp. 5111–5116.

[57] M. A. Lukowski, A. S. Daniel, F. Meng, A. Forticaux, L. Li, and S. Jin. "Enhanced hydrogen evolution catalysis from chemically exfoliated metallic MoS2 nanosheets". In: *Journal of the American Chemical Society* 135.28 (2013), pp. 10274–10277.

[58] J. N. Coleman, M. Lotya, A. O'Neill, S. D. Bergin, P. J. King, U. Khan, K. Young, A. Gaucher, S. De, R. J. Smith, et al. "Two-dimensional nanosheets produced by liquid exfoliation of layered materials". In: *Science* 331.6017 (2011), pp. 568–571.

[59] M. B. Dines. "Lithium intercalation via n-butyllithium of the layered transition metal dichalcogenides". In: *Materials Research Bulletin* 10.4 (1975), pp. 287–291.

[60] R. Kappera, D. Voiry, S. E. Yalcin, B. Branch, G. Gupta, A. D. Mohite, and M. Chhowalla. "Phase-engineered low-resistance contacts for ultrathin MoS2 transistors". In: *Nature materials* 13.12 (2014), pp. 1128–1134.

[61] X. Wang, H. Feng, Y. Wu, and L. Jiao. "Controlled synthesis of highly crystalline MoS2 flakes by chemical vapor deposition". In: *Journal of the American Chemical Society* 135.14 (2013), pp. 5304–5307.

[62] X. Ling, Y.-H. Lee, Y. Lin, W. Fang, L. Yu, M. S. Dresselhaus, and J. Kong. "Role of the seeding promoter in MoS2 growth by chemical vapor deposition". In: *Nano letters* 14.2 (2014), pp. 464–472.

[63] J.-S. Rhyee, J. Kwon, P. Dak, J. H. Kim, S. M. Kim, J. Park, Y. K. Hong, W. G. Song, I. Omkaram, M. A. Alam, et al. "High-mobility transistors based on large-area and highly crystalline CVD-grown MoSe2 films on insulating substrates". In: *Advanced Materials* 28.12 (2016), pp. 2316–2321.

[64] L. Zhou, A. Zubair, Z. Wang, X. Zhang, F. Ouyang, K. Xu, W. Fang, K. Ueno, J. Li, T. Palacios, et al. "Synthesis of high-quality large-area homogenous 1T′ MoTe2 from chemical vapor deposition". In: *Advanced materials* 28.43 (2016), pp. 9526–9531.

[65] H. Wang, C. Tsai, D. Kong, K. Chan, F. Abild-Pedersen, J. K. Nørskov, and Y. Cui. "Transition-metal doped edge sites in vertically aligned MoS2 catalysts for enhanced hydrogen evolution". In: *Nano Research* 8.2 (2015), pp. 566–575.

[66] A. Tarasov, S. Zhang, M.-Y. Tsai, P. M. Campbell, S. Graham, S. Barlow, S. R. Marder, and E. M. Vogel. "Controlled doping of large-area trilayer MoS2 with molecular reductants and oxidants." In: *Advanced Materials (Deerfield Beach, Fla.)* 27.7 (2015), pp. 1175–1181.

[67] B. V. Lotsch. "Vertical 2D heterostructures". In: *Annual Review of Materials Research* 45.1 (2015), pp. 85–109.

[68] M.-Y. Li, Y. Shi, C.-C. Cheng, L.-S. Lu, Y.-C. Lin, H.-L. Tang, M.-L. Tsai, C.-W. Chu, K.-H. Wei, J.-H. He, et al. "Epitaxial growth of a monolayer WSe2-MoS2 lateral pn junction with an atomically sharp interface". In: *Science* 349.6247 (2015), pp. 524–528.

[69] S. Vishwanath, X. Liu, S. Rouvimov, P. C. Mende, A. Azcatl, S. McDonnell, R. M. Wallace, R. M. Feenstra, J. K. Furdyna, D. Jena, et al. "Comprehensive structural and optical characterization of MBE grown MoSe2 on graphite, CaF2 and graphene". In: *2D Materials* 2.2 (2015), p. 024007.

[70] K. E. Aretouli, D. Tsoutsou, P. Tsipas, J. Marquez-Velasco, S. Aminalragia Giamini, N. Kelaidis, V. Psycharis, and A. Dimoulas. "Epitaxial 2D SnSe2/2D WSe2 van der waals heterostructures". In: *ACS applied materials & interfaces* 8.35 (2016), pp. 23222–23229.

[71] W. Choi, N. Choudhary, G. H. Han, J. Park, D. Akinwande, and Y. H. Lee. "Recent development of two-dimensional transition metal dichalcogenides and their applications". In: *Materials Today* 20.3 (2017), pp. 116–130.

[72] A. Chaves, J. G. Azadani, H. Alsalman, D. Da Costa, R. Frisenda, A. Chaves, S. H. Song, Y. D. Kim, D. He, J. Zhou, et al. "Bandgap engineering of two-dimensional semiconductor materials". In: *npj 2D Materials and Applications* 4.1 (2020), p. 29.

[73] M. Chhowalla, H. S. Shin, G. Eda, L.-J. Li, K. P. Loh, and H. Zhang. "The chemistry of two-dimensional layered transition metal dichalcogenide nanosheets". In: *Nature chemistry* 5.4 (2013), pp. 263–275.

[74] S. Feng, Z. Lin, X. Gan, R. Lv, and M. Terrones. "Doping two-dimensional materials: ultra-sensitive sensors, band gap tuning and ferromagnetic monolayers". In: *Nanoscale Horizons* 2.2 (2017), pp. 72–80.

[75] M. Ghorbani-Asl, S. Borini, A. Kuc, and T. Heine. "Strain-dependent modulation of conductivity in single-layer transition-metal dichalcogenides". In: *Physical Review B—Condensed Matter and Materials Physics* 87.23 (2013), p. 235434.

[76] K. Santosh, R. C. Longo, R. Addou, R. M. Wallace, and K. Cho. "Impact of intrinsic atomic defects on the electronic structure of MoS2 monolayers". In: *Nanotechnology* 25.37 (2014), p. 375703.

[77] T. Brumme, M. Calandra, and F. Mauri. "First-principles theory of field-effect doping in transition-metal dichalcogenides: Structural properties, electronic structure, Hall coefficient, and electrical conductivity". In: *Physical Review B* 91.15 (2015), p. 155436.

[78] Y. Ma, Y. Dai, M. Guo, C. Niu, J. Lu, and B. Huang. "Electronic and magnetic properties of perfect, vacancy-doped, and nonmetal adsorbed MoSe 2, MoTe 2 and WS 2 monolayers". In: *Physical Chemistry Chemical Physics* 13.34 (2011), pp. 15546–15553.

[79] W. Tang, S. S. Rassay, and N. M. Ravindra. "Electronic & optical properties of transition-metal dichalcogenides". In: *Madridge J. Nanotechnol. Nanosci* 2.1 (2017), pp. 58–64.

[80] C. Lee, H. Yan, L. E. Brus, T. F. Heinz, J. Hone, and S. Ryu. "Anomalous lattice vibrations of single-and few-layer MoS2". In: *ACS nano* 4.5 (2010), pp. 2695–2700.

[81] R. Lv, J. A. Robinson, R. E. Schaak, D. Sun, Y. Sun, T. E. Mallouk, and M. Terrones. "Transition metal dichalcogenides and beyond: synthesis, properties, and applications of single-and few-layer nanosheets". In: *Accounts of chemical research* 48.1 (2015), pp. 56–64.

[82] S. Joseph, J. Mohan, S. Lakshmy, S. Thomas, B. Chakraborty, S. Thomas, and N. Kalarikkal. "A review of the synthesis, properties, and applications of 2D transition metal dichalcogenides and their heterostructures". In: *Materials Chemistry and Physics* 297 (2023), p. 127332.

[83] K. F. Mak, K. He, C. Lee, G. H. Lee, J. Hone, T. F. Heinz, and J. Shan. "Tightly bound trions in monolayer MoS2". In: *Nature materials* 12.3 (2013), pp. 207–211.

[84] A. Ramasubramaniam. "Large excitonic effects in monolayers of molybdenum and tungsten dichalcogenides". In: *Physical Review B—Condensed Matter and Materials Physics* 86.11 (2012), p. 115409.

[85] R. Yan, J. R. Simpson, S. Bertolazzi, J. Brivio, M. Watson, X. Wu, A. Kis, T. Luo, A. R. Hight Walker, and H. G. Xing. "Thermal conductivity of monolayer molybdenum disulfide obtained from temperature-dependent Raman spectroscopy". In: *ACS nano* 8.1 (2014), pp. 986–993.

[86] Y. Hong, J. Zhang, and X. C. Zeng. "Thermal conductivity of monolayer MoSe2 and MoS2". In: *The Journal of Physical Chemistry C* 120.45 (2016), pp. 26067–26075.

[87] S. Wang, X. Yang, L. Hou, X. Cui, X. Zheng, and J. Zheng. "Organic covalent modification to improve thermoelectric properties of TaS2". In: *Nature Communications* 13.1 (2022), p. 4401.

[88] Z. Yan, C. Jiang, T. Pope, C. Tsang, J. Stickney, P. Goli, J. Renteria, T. Salguero, and A. Balandin. "Phonon and thermal properties of exfoliated TaSe2 thin films". In: *Journal of Applied Physics* 114.20 (2013).

[89] B. Peng, H. Zhang, H. Shao, Y. Xu, X. Zhang, and H. Zhu. "Thermal conductivity of monolayer MoS 2, MoSe 2, and WS 2: interplay of mass effect, interatomic bonding and anharmonicity". In: *RSC advances* 6.7 (2016), pp. 5767–5773.

[90] C.-C. Chen, Z. Li, L. Shi, and S. B. Cronin. "Thermal interface conductance across a graphene/hexagonal boron nitride heterojunction". In: *Applied Physics Letters* 104.8 (2014).

[91] Y. Cai, J. Lan, G. Zhang, and Y.-W. Zhang. "Lattice vibrational modes and phonon thermal conductivity of monolayer MoS 2". In: *Physical Review B* 89.3 (2014), p. 035438.

[92] G. Schweicher, G. d'Avino, M. T. Ruggiero, D. J. Harkin, K. Broch, D. Venkateshvaran, G. Liu, A. Richard, C. Ruzié, J. Armstrong, et al. "Chasing the "killer" phonon mode for the rational design of low-disorder, high-mobility molecular semiconductors". In: *Advanced Materials* 31.43 (2019), p. 1902407.

[93] T. Nematiaram and A. Troisi. "Modeling charge transport in high-mobility molecular semiconductors: Balancing electronic structure and quantum dynamics methods with the help of experiments". In: *The Journal of chemical physics* 152.19 (2020).

[94] M. Hutereau, P. A. Banks, B. Slater, J. A. Zeitler, A. D. Bond, and M. T. Ruggiero. "Resolving anharmonic lattice dynamics in molecular crystals with X-ray diffraction and terahertz spectroscopy". In: *Physical Review Letters* 125.10 (2020), p. 103001.

[95] A. van Der Lee and D. G. Dumitrescu. "Thermal expansion properties of organic crystals: a CSD study". In: *Chemical science* 12.24 (2021), pp. 8537–8547.

[96] M. N. Gueye, A. Vercouter, R. Jouclas, D. Guérin, V. Lemaur, G. Schweicher, S. Lenfant, A. Antidormi, Y. Geerts, C. Melis, et al. "Thermal conductivity of benzothieno-benzothiophene derivatives at the nanoscale". In: *Nanoscale* 13.6 (2021), pp. 3800–3807.

[97] M. Asher, R. Jouclas, M. Bardini, Y. Diskin-Posner, N. Kahn, R. Korobko, A. R. Kennedy, L. Silva de Moraes, G. Schweicher, J. Liu, et al. "Chemical modifications suppress anharmonic effects in the lattice dynamics of organic semiconductors". In: *ACS Materials Au* 2.6 (2022), pp. 699–708.

[98] P. Yu, Y. Zhen, H. Dong, and W. Hu. "Crystal engineering of organic optoelectronic materials". In: *Chem* 5.11 (2019), pp. 2814–2853.

[99] C. Park, J. E. Park, and H. C. Choi. "Crystallization-induced properties from morphology-controlled organic crystals". In: *Accounts of chemical research* 47.8 (2014), pp. 2353–2364.

[100] Z. Zhang, L. Jiang, C. Cheng, Y. Zhen, G. Zhao, H. Geng, Y. Yi, L. Li, H. Dong, Z. Shuai, et al. "The impact of interlayer electronic coupling on charge transport in organic semiconductors: a case study on titanylphthalocyanine single crystals". In: *Angewandte Chemie* 128.17 (2016), pp. 5292–5295.

[101] J. E. Park, M. Son, M. Hong, G. Lee, and H. C. Choi. "Crystal-Plane-Dependent Photoluminescence of Pentacene 1D Wire and 2D Disk Crystals". In: *Angewandte Chemie* 124.26 (2012), pp. 6489–6494.

[102] H. Dong, X. Fu, J. Liu, Z. Wang, and W. Hu. "25th anniversary article: key points for high-mobility organic field-effect transistors". In: *Advanced materials* 25.43 (2013), pp. 6158–6183.

[103] W. Shao, H. Dong, L. Jiang, and W. Hu. "Morphology control for high performance organic thin film transistors". In: *Chemical Science* 2.4 (2011), pp. 590–600.

[104] D. H. Kim, Y. D. Park, Y. Jang, S. Kim, and K. Cho. "Solvent vapor-induced nanowire formation in poly (3-hexylthiophene) thin films". In: *Macromolecular rapid communications* 26.10 (2005), pp. 834–839.

[105] J. A. Lim, F. Liu, S. Ferdous, M. Muthukumar, and A. L. Briseno. "Polymer semiconductor crystals". In: *Materials Today* 13.5 (2010), pp. 14–24.

[106] C. Wang, H. Dong, L. Jiang, and W. Hu. "Organic semiconductor crystals". In: *Chemical Society Reviews* 47.2 (2018), pp. 422–500.

[107] J. Jang, S. Nam, K. Im, J. Hur, S. N. Cha, J. Kim, H. B. Son, H. Suh, M. A. Loth, J. E. Anthony, et al. "Highly crystalline soluble acene crystal arrays for organic transistors: mechanism of crystal growth during dip-coating". In: *Advanced Functional Materials* 22.5 (2012), pp. 1005–1014.

[108] L. Li, P. Gao, W. Wang, K. Müllen, H. Fuchs, and L. Chi. "Growth of ultrathin organic semiconductor microstripes with thickness control in the monolayer precision." In: *Angewandte Chemie* 125.48 (2013).

[109] J.-M. Lehn. *Supramolecular chemistry: concepts and perspectives*. John Wiley & Sons, 1995.

[110] G. R. Desiraju and A. Gavezzotti. "From molecular to crystal structure; polynuclear aromatic hydrocarbons". In: *Journal of the Chemical Society, Chemical Communications* 10 (1989), pp. 621–623.

[111] C. A. Hunter and J. K. Sanders. "The nature of. pi.-. pi. interactions". In: *Journal of the American Chemical Society* 112.14 (1990), pp. 5525–5534.

[112] M. Nishio. "CH/π hydrogen bonds in crystals". In: *CrystEngComm* 6.27 (2004), pp. 130–158.

[113] L. C. Gilday, S. W. Robinson, T. A. Barendt, M. J. Langton, B. R. Mullaney, and P. D. Beer. "Halogen bonding in supramolecular chemistry". In: *Chemical reviews* 115.15 (2015), pp. 7118–7195.

[114] C. Wang, H. Dong, W. Hu, Y. Liu, and D. Zhu. "Semiconducting π-conjugated systems in field-effect transistors: a material odyssey of organic electronics". In: *Chemical reviews* 112.4 (2012), pp. 2208–2267.

[115] C. Reese, M. Roberts, M.-m. Ling, and Z. Bao. "Organic thin film transistors". In: *Materials Today* 7.9 (2004), pp. 20–27. ISSN: 1369-7021. DOI: https://doi.org/10.1016/S1369-7021(04)00398-0. URL: https://www.sciencedirect.com/science/article/pii/S1369702104003980.

[116] I. E. Jacobs and A. J. Moulé. "Controlling molecular doping in organic semiconductors". In: *Advanced Materials* 29.42 (2017), p. 1703063.

[117] O. Bubnova, Z. U. Khan, A. Malti, S. Braun, M. Fahlman, M. Berggren, and X. Crispin. "Optimization of the thermoelectric figure of merit in the conducting polymer poly (3, 4-ethylenedioxythiophene)". In: *Nature materials* 10.6 (2011), pp. 429–433.

[118] O. Ostroverkhova. "Organic optoelectronic materials: mechanisms and applications". In: *Chemical reviews* 116.22 (2016), pp. 13279–13412.

[119] A. Köhler and H. Bässler. *Electronic processes in organic semiconductors: An introduction*. John Wiley & Sons, 2015.

[120] J. Nyman and G. M. Day. "Static and lattice vibrational energy differences between polymorphs". In: *CrystEngComm* 17.28 (2015), pp. 5154–5165.

[121] J. Nyman and G. M. Day. "Modelling temperature-dependent properties of polymorphic organic molecular crystals". In: *Physical Chemistry Chemical Physics* 18.45 (2016), pp. 31132–31143.

[122] M. N. Gueye, A. Vercouter, R. Jouclas, D. Guérin, V. Lemaur, G. Schweicher, S. Lenfant, A. Antidormi, Y. Geerts, C. Melis, J. Cornil, and D. Vuillaume. "Thermal conductivity of benzothieno-benzothiophene derivatives at the nanoscale". In: *Nanoscale* 13 (6 2021), pp. 3800–3807. DOI: 10.1039/D0NR08619C. URL: http://dx.doi.org/10.1039/D0NR08619C.

[123] W. Shi, J. Chen, J. Xi, D. Wang, and Z. Shuai. "Search for Organic Thermoelectric Materials with High Mobility: The Case of 2,7-Dialkyl[1]benzothieno[3,2-b][1]benzothiophene Derivatives". In: *Chemistry of Materials* 26.8 (2014), pp. 2669–2677. DOI: 10.1021/cm500429w. URL: https://doi.org/10.1021/cm500429w.

[124] E. Selezneva, A. Vercouter, G. Schweicher, V. Lemaur, K. Broch, A. Antidormi, K. Takimiya, V. Coropceanu, J.-L. Brédas, C. Melis, et al. "Strong Suppression of Thermal Conductivity in the Presence of Long Terminal Alkyl Chains in Low-Disorder Molecular Semiconductors". In: *Advanced materials* 33.37 (2021), p. 2008708.

[125] A. Cappai, A. Antidormi, A. Bosin, D. Narducci, L. Colombo, and C. Melis. "Impact of synthetic conditions on the anisotropic thermal conductivity of poly (3, 4-ethylenedioxythiophene)(PEDOT): A molecular dynamics investigation". In: *Physical Review Materials* 4.3 (2020), p. 035401.

[126] A. Pinna, M. F. Casula, L. Pilia, A. Cappai, C. Melis, P. C. Ricci, and C. M. Carbonaro. "Driving the polymerization of PEDOT:PSS by means of a nanoporous template: Effects on the structure". In: *Polymer* 185 (2019), p. 121941. ISSN: 0032-3861. DOI: https://doi.org/10.1016/j.polymer.2019.121941. URL: https://www.sciencedirect.com/science/article/pii/S0032386119309474.

[127] Z. Fan, D. Du, H. Yao, and J. Ouyang. "Higher PEDOT molecular weight giving rise to higher thermoelectric property of PEDOT: PSS: a comparative study of clevios P and clevios PH1000". In: *ACS applied materials & interfaces* 9.13 (2017), pp. 11732–11738.

[128] C. Genovese, A. Antidormi, R. Dettori, C. Caddeo, A. Mattoni, L. Colombo, and C. Melis. "Linking morphology to thermal conductivity in PEDOT: an atomistic investigation". In: *Journal of Physics D: Applied Physics* 50.49 (2017), p. 494002.

[129] A. Cappai, A. Antidormi, A. Bosin, D. Galliani, D. Narducci, and C. Melis. "Interplay between synthetic conditions and micromorphology in poly(3,4-ethylenedioxythiophene):tosylate (PEDOT:Tos): an atomistic investigation". In: *Phys. Chem. Chem. Phys.* 21 (16 2019), pp. 8580–8586. DOI: 10.1039/C9CP00970A. URL: http://dx.doi.org/10.1039/C9CP00970A.

[130] A. Crnjar, C. Melis, and L. Colombo. "Assessing the anomalous superdiffusive heat transport in a single one-dimensional PEDOT chain". In: *Physical Review Materials* 2.1 (2018), p. 015603.

[131] L. Colombo. *Solid state physics: a primer*. IoP Publishing, 2021.

[132] R. E. Peierls. *Zur kinetischen theorie der wärmeleitung in kristallen*. JA Barth, 1929.

[133] A. Inyushkin, A. Taldenkov, A. Gibin, A. Gusev, and H.-J. Pohl. "On the isotope effect in thermal conductivity of silicon". In: *Physica status solidi (C)* 1.11 (2004), pp. 2995–2998.

[134] W. Kohn. "Nobel Lecture: Electronic structure of matter - wave functions and density functionals". In: *Rev. Mod. Phys.* 71 (5 1999), pp. 1253–1266. DOI: 10.1103/RevModPhys.71.1253.

[135] P. Hohenberg and W. Kohn. "Inhomogeneous Electron Gas". In: *Phys. Rev.* 136 (3B Nov. 1964), B864–B871. DOI: 10.1103/PhysRev.136.B864. URL: https://link.aps.org/doi/10.1103/PhysRev.136.B864.

[136] W. Kohn and L. J. Sham. "Self-Consistent Equations Including Exchange and Correlation Effects". In: *Phys. Rev.* 140 (4A Nov. 1965), A1133–A1138. DOI: 10.1103/PhysRev.140.A1133. URL: https://link.aps.org/doi/10.1103/PhysRev.140.A1133.

[137] E. Wigner. "On the Interaction of Electrons in Metals". In: *Phys. Rev.* 46 (11 1934), pp. 1002–1011. DOI: 10.1103/PhysRev.46.1002.

[138] J. P. Perdew, J. A. Chevary, S. H. Vosko, K. A. Jackson, M. R. Pederson, D. J. Singh, and C. Fiolhais. "Atoms, molecules, solids, and surfaces: Applications of the generalized gradient approximation for exchange and correlation". In: *Phys. Rev. B* 46 (11 Sept. 1992), pp. 6671–6687. DOI: 10.1103/PhysRevB.46.6671. URL: https://link.aps.org/doi/10.1103/PhysRevB.46.6671.

[139] J. P. Perdew, A. Ruzsinszky, G. I. Csonka, O. A. Vydrov, G. E. Scuseria, L. A. Constantin, X. Zhou, and K. Burke. "Restoring the density-gradient expansion for exchange in solids and surfaces". In: *Physical review letters* 100.13 (2008), p. 136406.

[140] A. P. Thompson, H. M. Aktulga, R. Berger, D. S. Bolintineanu, W. M. Brown, P. S. Crozier, P. J. in 't Veld, A. Kohlmeyer, S. G. Moore, T. D. Nguyen, R. Shan, M. J. Stevens, J. Tranchida, C. Trott, and S. J. Plimpton. "LAMMPS - a flexible simulation tool for particle-based materials modeling at the atomic, meso, and continuum scales". In: *Comp. Phys. Comm.* 271 (2022), p. 108171. DOI: 10.1016/j.cpc.2021.108171.

[141] W. C. Swope, H. C. Andersen, P. H. Berens, and K. R. Wilson. "A computer simulation method for the calculation of equilibrium constants for the formation of physical clusters of molecules: Application to small water clusters". In: *The Journal of chemical physics* 76.1 (1982), pp. 637–649.

[142] S.-i. Tamura. "Isotope scattering of dispersive phonons in Ge". In: *Physical Review B* 27.2 (1983), p. 858.

[143] A. Cappai, C. Melis, D. Marongiu, F. Quochi, M. Saba, F. Congiu, Y. He, T. J. Slade, M. G. Kanatzidis, and L. Colombo. "Strong anharmonicity at the origin of anomalous thermal conductivity in double perovskite Cs2NaYbCl6". In: *Advanced Science* 11.9 (2024), p. 2305861.

[144] T. Tadano, Y. Gohda, and S. Tsuneyuki. "Anharmonic force constants extracted from first-principles molecular dynamics: applications to heat transfer simulations". In: *Journal of Physics: Condensed Matter* 26.22 (2014), p. 225402.

[145] C. Melis, R. Dettori, S. Vandermeulen, and L. Colombo. "Calculating thermal conductivity in a transient conduction regime: theory and implementation". In: *The European Physical Journal B* 87.4 (2014), p. 96.

[146] D. P. Sellan, E. S. Landry, J. Turney, A. J. McGaughey, and C. H. Amon. "Size effects in molecular dynamics thermal conductivity predictions". In: *Physical Review B—Condensed Matter and Materials Physics* 81.21 (2010), p. 214305.

[147] P. B. Allen and J. L. Feldman. "Thermal conductivity of glasses: Theory and application to amorphous Si". In: *Physical review letters* 62.6 (1989), p. 645.

[148] M. Simoncelli, N. Marzari, and F. Mauri. "Wigner formulation of thermal transport in solids". In: *Physical Review X* 12.4 (2022), p. 041011.

[149] G. Caldarelli, M. Simoncelli, N. Marzari, F. Mauri, and L. Benfatto. "Many-body Green's function approach to lattice thermal transport". In: *Physical Review B* 106.2 (2022), p. 024312.

[150] V. D. Camiola, V. Romano, and G. Vitanza. "Wigner equations for phonons transport and quantum heat flux". In: *Journal of Nonlinear Science* 34.1 (2024), p. 10.

[151] E. Di Lucente, M. Simoncelli, and N. Marzari. "Crossover from Boltzmann to Wigner thermal transport in thermoelectric skutterudites". In: *Physical Review Research* 5.3 (2023), p. 033125.

[152] T. Sun, D.-B. Zhang, and R. M. Wentzcovitch. "Dynamic stabilization of cubic $CaSiO_3$ perovskite at high temperatures and pressures from ab initio molecular dynamics". In: *Phys. Rev. B* 89 (9 Mar. 2014), p. 094109. DOI: 10.1103/PhysRevB.89.094109. URL: https://link.aps.org/doi/10.1103/PhysRevB.89.094109.

[153] A. Togo, L. Chaput, T. Tadano, and I. Tanaka. "Implementation strategies in phonopy and phono3py". In: *J. Phys. Condens. Matter* 35.35 (2023), p. 353001. DOI: 10.1088/1361-648X/acd831.

[154] A. Togo. "First-principles Phonon Calculations with Phonopy and Phono3py". In: *J. Phys. Soc. Jpn.* 92.1 (2023), p. 012001. DOI: 10.7566/JPSJ.92.012001.

[155] A. Carreras, A. Togo, and I. Tanaka. "DynaPhoPy: A code for extracting phonon quasiparticles from molecular dynamics simulations". In: *Computer Physics Communications* 221 (2017), pp. 221–234. ISSN: 0010-4655. DOI: https://doi.org/10.1016/j.cpc.2017.08.017. URL: https://www.sciencedirect.com/science/article/pii/S0010465517302631.

[156] W. Fu, Y. Chen, J. Lin, X. Wang, Q. Zeng, J. Zhou, L. Zheng, H. Wang, Y. He, H. He, et al. "Controlled synthesis of atomically thin 1T-TaS2 for tunable charge density wave phase transitions". In: *Chemistry of Materials* 28.21 (2016), pp. 7613–7618.

[157] F. Siddi, A. Cappai, L. Colombo, and C. Melis. "An Ab Initio Investigation of Ultra-Low Thermal Conductivity in Organically Functionalized TaS 2 \rmTaS_2". In: *Advanced Theory and Simulations* 7.6 (2024), p. 2400056.

[158] P. Giannozzi, S. Baroni, N. Bonini, M. Calandra, R. Car, C. Cavazzoni, D. Ceresoli, G. L. Chiarotti, M. Cococcioni, I. Dabo, et al. "QUANTUM ESPRESSO: a modular and open-source software project for quantumsimulations of materials". In: *Journal of physics: Condensed matter* 21.39 (2009), p. 395502.

[159] M. Ernzerhof and G. E. Scuseria. "Assessment of the Perdew–Burke–Ernzerhof exchange-correlation functional". In: *The Journal of chemical physics* 110.11 (1999), pp. 5029–5036.

[160] G. Kresse and D. Joubert. "From ultrasoft pseudopotentials to the projector augmented-wave method". In: *Physical review b* 59.3 (1999), p. 1758.

[161] G. Liu, Z. Zhang, H. Wang, G.-L. Li, J.-S. Wang, and Z. Gao. "Large contribution of quasi-acoustic shear phonon modes to thermal conductivity in novel monolayer Ga2O3". In: *Journal of Applied Physics* 130.10 (2021).

[162] A. A. Balandin, S. Ghosh, W. Bao, I. Calizo, D. Teweldebrhan, F. Miao, and C. N. Lau. "Superior thermal conductivity of single-layer graphene". In: *Nano letters* 8.3 (2008), pp. 902–907.

[163] P. Klemens and D. Pedraza. "Thermal conductivity of graphite in the basal plane". In: *Carbon* 32.4 (1994), pp. 735–741.

[164] V. Guerra, C. Wan, and T. McNally. "Thermal conductivity of 2D nano-structured boron nitride (BN) and its composites with polymers". In: *Progress in Materials Science* 100 (2019), pp. 170–186.

[165] M. Christensen, A. B. Abrahamsen, N. B. Christensen, F. Juranyi, N. H. Andersen, K. Lefmann, J. Andreasson, C. R. Bahl, and B. B. Iversen. "Avoided crossing of rattler modes in thermoelectric materials". In: *Nature materials* 7.10 (2008), pp. 811–815.

[166] W. Li, J. Carrete, G. K. Madsen, and N. Mingo. "Influence of the optical-acoustic phonon hybridization on phonon scattering and thermal conductivity". In: *Physical Review B* 93.20 (2016), p. 205203.

[167] Y. Li, S. Yamamoto, K. Ahmad, Z. Almutairi, K. Koumoto, and C. Wan. "Localized vibration and avoided crossing in SrTi 11 O 20 for oxide thermoelectrics with intrinsically low thermal conductivity". In: *Journal of Materials Chemistry A* 9.19 (2021), pp. 11674–11682.

[168] K. R. Hahn, C. Melis, F. Bernardini, L. Paulatto, and L. Colombo. "Thermal transport in H-terminated ultrathin [110] Si nanowires: a first principles study". In: *The European Physical Journal Plus* 138.11 (2023), p. 1028.

[169] R. Franz and G. Wiedemann. "Ueber die wärme-leitungsfähigkeit der metalle". In: *Annalen der Physik* 165.8 (1853), pp. 497–531.

[170] G. Catelani. "Interaction corrections: Temperature and parallel field dependencies of the Lorentz number in two-dimensional disordered metals". In: *Physical Review B—Condensed Matter and Materials Physics* 75.2 (2007), p. 024208.

[171] B. Radisavljevic, A. Radenovic, and J. Brivio. "i. V. Giacometti and A. Kis". In: *Nat. Nanotechnol* 6.3 (2011), pp. 147–150.

[172] Y. Zhang, J. Ye, Y. Matsuhashi, and Y. Iwasa. "Ambipolar MoS2 thin flake transistors". In: *Nano letters* 12.3 (2012), pp. 1136–1140.

[173] K. Mak, C. Lee, and J. Hone. "j. Shan and TF Heinz". In: *Phys. Rev. Lett* 105 (2010), p. 036805.

[174] O. Samy, S. Zeng, M. D. Birowosuto, and A. El Moutaouakil. "A review on MoS2 properties, synthesis, sensing applications and challenges". In: *Crystals* 11.4 (2021), p. 355.

[175] A. N. Gandi and U. Schwingenschlögl. "Thermal conductivity of bulk and monolayer MoS2". In: *Europhysics Letters* 113.3 (2016), p. 36002.

[176] J. J. Bae, H. Y. Jeong, G. H. Han, J. Kim, H. Kim, M. S. Kim, B. H. Moon, S. C. Lim, and Y. H. Lee. "Thickness-dependent in-plane thermal conductivity of suspended MoS 2 grown by chemical vapor deposition". In: *Nanoscale* 9.7 (2017), pp. 2541–2547.

[177] V. Varshney, J. Lee, B. L. Farmer, A. A. Voevodin, and A. K. Roy. "Modeling of cross-plane interface thermal conductance between graphene nano-ribbons". In: *2D Materials* 1.2 (2014), p. 025005.

[178] X. Liu, G. Zhang, Q.-X. Pei, and Y.-W. Zhang. "Phonon thermal conductivity of monolayer MoS2 sheet and nanoribbons". In: *Applied Physics Letters* 103.13 (2013).

[179] L. Zheng, R. Sahul, S. Zhang, W. Jiang, S. Li, and W. Cao. "Orientation dependence of piezoelectric properties and mechanical quality factors of 0.27 Pb (In1/2Nb1/2) O3-0.46 Pb (Mg1/3Nb2/3) O3-0.27 PbTiO3: Mn single crystals". In: *Journal of Applied Physics* 114.10 (2013).

[180] W. Li, J. Carrete, and N. Mingo. "Thermal conductivity and phonon linewidths of monolayer MoS2 from first principles". In: *Applied Physics Letters* 103.25 (2013).

[181] W. Huang, H. Da, and G. Liang. "Thermoelectric performance of mx2 (m= mo, w; x= s, se) monolayers". In: *Journal of Applied Physics* 113.10 (2013).

[182] A. J. Gabourie, Ç. Köroğlu, and E. Pop. "Substrate-dependence of monolayer MoS2 thermal conductivity and thermal boundary conductance". In: *Journal of Applied Physics* 131.19 (2022).

[183] R. Dettori, C. Melis, R. Rurali, and L. Colombo. "Thermal rectification in silicon by a graded distribution of defects". In: *Journal of applied physics* 119.21 (2016).

[184] R. Dettori, C. Melis, and L. Colombo. "SixGe1-x alloy as efficient phonon barrier in Ge/Si superlattices for thermoelectric applications". In: *The European Physical Journal B* 88.1 (2015), p. 27.

[185] B. Lorenzi, R. Dettori, M. T. Dunham, C. Melis, R. Tonini, L. Colombo, A. Sood, K. E. Goodson, and D. Narducci. "Phonon scattering in Silicon by multiple morphological defects: A multiscale analysis". In: *Journal of Electronic Materials* 47.9 (2018), pp. 5148–5157.

[186] S. Mahendran, J. Carrete, A. Isacsson, G. K. Madsen, and P. Erhart. "Quantitative predictions of the thermal conductivity in transition metal dichalcogenides: Impact of point defects in MoS2 and WS2 monolayers". In: *The Journal of Physical Chemistry C* 128.4 (2024), pp. 1709–1716.

[187] W. Zhou, X. Zou, S. Najmaei, Z. Liu, Y. Shi, J. Kong, J. Lou, P. M. Ajayan, B. I. Yakobson, and J.-C. Idrobo. "Intrinsic structural defects in monolayer molybdenum disulfide". In: *Nano letters* 13.6 (2013), pp. 2615–2622.

[188] M. Sledzinska, R. Quey, B. Mortazavi, B. Graczykowski, M. Placidi, D. Saleta Reig, D. Navarro-Urrios, F. Alzina, L. Colombo, S. Roche, et al. "Record low thermal conductivity of polycrystalline MoS2 films: tuning the thermal conductivity by grain orientation". In: *ACS applied materials & interfaces* 9.43 (2017), pp. 37905–37911.

[189] C. Muratore, V. Varshney, J. J. Gengler, J. Hu, J. E. Bultman, A. K. Roy, B. L. Farmer, and A. A. Voevodin. "Thermal anisotropy in nano-crystalline MoS 2 thin films". In: *Physical Chemistry Chemical Physics* 16.3 (2014), pp. 1008–1014.

[190] R. Dettori, F. Siddi, L. Colombo, and C. Melis. "Superlattice Thermal Modulation in MoS_2 by Defect Engineering". In: *Advanced Theory and Simulations* 8.3 (2025), p. 2401199. DOI: https://doi.org/10.1002/adts.202401199. eprint: https://advanced.onlinelibrary.wiley.com/doi/pdf/10.1002/adts.202401199. URL: https://advanced.onlinelibrary.wiley.com/doi/abs/10.1002/adts.202401199.

[191] J.-W. Jiang. "Parametrization of Stillinger–Weber potential based on valence force field model: application to single-layer MoS2 and black phosphorus". In: *Nanotechnology* 26.31 (2015), p. 315706.

[192] J.-W. Jiang. "Misfit strain-induced buckling for transition-metal dichalcogenide lateral heterostructures: A molecular dynamics study". In: *Acta Mechanica Solida Sinica* 32.1 (2019), pp. 17–28.

[193] N. Cortés, L. Rosales, P. Orellana, A. Ayuela, and J. González. "Stacking change in MoS_2 bilayers induced by interstitial Mo impurities". In: *Scientific Reports* 8 (Feb. 2018). DOI: 10.1038/s41598-018-20289-1.

[194] J. Wang, R. M. Wolf, J. W. Caldwell, P. A. Kollman, and D. A. Case. "Development and testing of a general amber force field". In: *Journal of computational chemistry* 25.9 (2004), pp. 1157–1174.

[195] T. Yamamoto and K. Takimiya. "Facile Synthesis of Highly π-Extended Heteroarenes, Dinaphtho[2,3-b:2',3'-f]chalcogenopheno[3,2-b]chalcogenophenes, and Their Application to Field-Effect Transistors". In: *Journal of the American Chemical Society* 129.8 (2007). PMID: 17279756, pp. 2224–2225. DOI: 10.1021/ja068429z. eprint: https://doi.org/10.1021/ja068429z. URL: https://doi.org/10.1021/ja068429z.

[196] Q. Guo, X. Ye, L. Qinglian, Q. Han, C. Ge, X. Zheng, L. Zhang, S. Cui, Y. Wu, C. Li, Y. Liu, and X. Tao. "Micro-spacing In-Air Sublimation Growth of Ultrathin Organic Single Crystals". In: *Chemistry of Materials* XXXX (Aug. 2020). DOI: 10.1021/acs.chemmater.9b05215.

[197] W. Xie, K. Willa, Y. Wu, R. Häusermann, K. Takimiya, B. Batlogg, and C. D. Frisbie. "Temperature-Independent Transport in High-Mobility Dinaphtho-Thieno-Thiophene (DNTT) Single Crystal Transistors". In: *Advanced Materials* 25.25 (2013), pp. 3478–3484. DOI: https://doi.org/10.1002/adma.201300886. eprint: https://advanced.onlinelibrary.

wiley.com/doi/pdf/10.1002/adma.201300886. URL: https://advanced.onlinelibrary.wiley.com/doi/abs/10.1002/adma.201300886.

Acknowledgments

This thesis was produced while attending the PhD programme in Physics at the University of Cagliari, Cycle XXXVIII, with the support of a scholarship financed by the Ministerial Decree no. 351 of 9th April 2022, based on the NRRP - funded by the European Union - NextGenerationEU - Mission 4 "Education and Research", Component 1 "Enhancement of the offer of educational services: from nurseries to universities" - Investment 4.1 "Extension of the number of research doctorates and innovative doctorates for public administration and cultural heritage".